New methods for exploring gastrointestinal disorders and diseases based on electrical bioimpedance and optical fibre sensing

Albert Ruiz-Vargas
BEng (Electronics), MEng (Mechanical), MSc (Biomedical)

A thesis submitted to the College of Science and Engineering
in total fulfilment of the requirements of the degree of
Doctor of Philosophy

The Medical Device Research Institute
Flinders University - Adelaide, Australia

February 20, 2019

Contents

List of Figures

List of Tables

Abbreviations and symbols

AC	Alternating current
ADC	Analogue to digital converter
Ag	Silver
AgCl	Silver chloride
BIS	Bioimpedance spectroscopy
BMS	Bioimpedance measurement system
$CaCl_2$	Calcium chloride
CCD	Charge-coupled device
CMRR	Common mode rejection ratio
CO_2	Carbon dioxide
DAC	Digital to analogue converter
DC	Direct current
D-Glucose	Glucose
DMaps	Diameter Maps
DPMaps	Diameter and pressure composite maps
ECG	Electrocardiography
EEG	Electroencelography
EGG	Electrogastography
EIS	Electrical impedance spectroscopy
EIT	Electrical impedance tomography

FBG	Fibre Bragg Grating
FD	Functional disorders
FEM	Finite Element Method
FGIDs	Functional gastrointestinal disorders
GERD	Gastroesophageal reflux disease
GI	Gastrointestinal
GIDs	Gastrointestinal disorders
HR	High resolution
HRIM	High-Resolution-Impedance-Manometry
IBS	Irritable bowel syndrome
IMaps	Impedance Maps
IPMaps	Impedance and pressure composite maps
IQR	Interquartile range
KCl	Potassium chloride
LOS	Lower oesophageal sphincter
MD	Motility disorders
$MgCl_2$	Magnesium chloride
MII	Multichannel intraluminal impedance
MRI	Magnetic resonance imaging
NaCl	Sodium chloride
NaH_2PO_4	Monosodium phosphate
$NaHCO_3$	Sodium bicarbonate
O_2	Oxygen
OFS	Optical fibre sensor
PCC	Pearson's correlation coefficient
PEEK	Polyether Ether Ketone

Pmaps	Pressure Maps
PTFE	PolyTetraFlouroEthelene
RLC	Resistor, inductor and capacitor
SD	Structural disorders
SDM	Spatial division multiplexing
TDM	Time division multiplexing
UOS	Upper oesophageal sphincter
US	Ultrasonography
WDM	Wavelength division multiplexing
$^{\mathbf{99m}}\mathbf{Tc}$	Technetium 99m
$^{\mathbf{113}}\mathbf{In}$	Indiun 113
$^{\mathbf{13}}\mathbf{C}$	Carbon 13
$^{\mathbf{13}}\mathbf{CO_2}$	Carbon 13 dioxide
B	Susceptance, S
C	Capacitance, F
D	Diameter, mm
F	Force magnitude, N
G	Conductance, S
I	Current, A
$\vec{J}$	Current density, Am^{-2}
K	Cell constant, m^{-1}
M	Mass, g
P	Pressure, mmHg or kPa
R	Resistance, Ω
S	Impedance sensitivity, m^{-4}
T	Temperature, ℃

V	Voltage, V
X	Reactance, Ω
Y	Admittance, S
Z	Impedance = R + jX, $\Omega + j\Omega$
$\|Z\|$	Impedance magnitude, Ω
$\angle Z$	Phase angle, $^\circ$
ε	Permittivity, Fm^{-1}
ε_0	Vacuum permittivity, $8.85 \times 10^{-12}\,\mathrm{Fm}^{-1}$
ε_r	Relative permittivity, adimensional
λ	Wavelength, nm
ρ	Resistivity, Ωm
σ	Conductivity, Sm^{-1}

Glossary

Agar-Agar: a gelatinous substance obtained from certain red seaweeds and used in biological culture media.

bolus: small rounded mixture of food and saliva formed in the mouth during the chewing process.

chyme: substance consisting of gastric juices and partly digested food.

excitation or measuring frequency: frequency at which impedance is measured. It corresponds to the frequency of the excitation signal it is applied to measure the impedance of the sample.

***ex-vivo*:** experimentation or measurements performed in or on tissue from an organism in an external environment with minimal alteration of natural conditions.

haustral sacs: are the small pouches caused by sacculation (sac formation), which give the colon its segmented appearance.

***in-silico*:** experimentation or measurements performed on a computer or via computer simulation.

***in-vitro*:** experimentation or measurements performed or taking place in a test tube, culture dish, or elsewhere outside a living organism.

***in-vivo*:** experimentation or measurements performed or taking place in a living organism or cells, usually animals, including humans, and plants, as opposed to a tissue extract or dead organism.

lumina: plural noun of lumen.

plexus: a network of nerves or vessels in the body.

plicae: a fold or ridge of tissue.

ripples: a small wave or series of waves.

rugae: is a term used in anatomy that refers to a series of ridges produced by folding of the wall of an organ.

spatiotemporal: term indicating a characteristic or parameter belonging to both space and time or to space–time.

steady state: an unvarying condition in a physical process.

Abstract

Gastrointestinal disorders and diseases are classified as either, functional, structural or motile. Around one third of the population in Australia report symptoms related with functional gastrointestinal disorders at some point during their lives. Approximately, 50 to 60 million US citizens were affected by gastrointestinal symptoms in 2010.

Electrical bioimpedance is used as a clinical tool in oesophageal studies, but it is still a research tool on other parts of the gastrointestinal tract, especially in the lower gastrointestinal tract. That is why, I have focused on the use of electrical bioimpedance in the lower gastrointestinal tract.

In this thesis, I have developed a bioimpedance measurement system, three impedance measuring probes and multiple custom-made software packages to acquire, save and display data in real-time. The three devices, are as follows: 1) a four-electrode catheter, 2) a novel High-Resolution-Impedance-Manometry (HRIM) catheter with fibre optic pressure sensors and closely spaced impedance electrodes, and 3) a novel four-electrode-contact electrical impedance probe with fibre optic contact pressure and temperature sensors built in it. Furthermore, a 3D model of the gastrointestinal tract was implemented that has provided greater understanding of the experimental results obtained during this thesis.

Different *in-vitro* and *in-silico* experiments were performed to investigate: 1) the use of different measuring frequencies and parameters (such as impedance magnitude and phase angle) for bolus transit studies, 2) the differentiation between different luminal contents, and 3) the effect of closer electrode separation on HRIM catheters. In addition, an *in-vitro* animal and *ex-vivo* human experiments were performed to investigate the use of monitoring the contact pressure on, and standardisation of bioimpedance measurements.

Results showed that the phase angle had much better correlation with changes in luminal diameter than impedance magnitude. The best frequency to use for differentiating between content (liquid and mixed gas) depended on which impedance parameter was selected, with larger differences observed at 177.81 kHz for phase angle, and 5.62 kHz

for impedance magnitude. The custom HRIM catheter had twice the spatial resolution of impedance electrodes compared to commercially available HRIM catheters. As a result, subtle muscular contractions in the colon were identified for the first time in *in-vitro* animal models.

The results with the pencil probe corroborated the previously reported contact pressure dependency on bioimpedance measurements; which demonstrates the importance of controlling and monitoring the contact pressure. A new method to standardize bioimpedance measurement is suggested. This method provides the resistivity normalised to a contact pressure of 0 kPa and also the ratio of resistivity over contact pressure. Two distinct regions of this ratio were observed during the trials, which might be indicative of damage.

The findings and improvements presented in this thesis will help clinical researchers to gain insight on how the gastrointestinal tract works and to standardize bioimpedance measurements for tissue characterization in the gastrointestinal tract in the following ways. Firstly, it was found that the phase angle parameter can add extra information to lower gastrointestinal bolus transit studies by providing information on bolus type. Secondly, the increased spatial resolution achieved in the HRIM catheter allows initiating accurate bolus transit studies in *in-vivo* animals, in which the use of an external camera will no longer be possible. Finally, monitoring the contact pressure on bioimpedance measurements will improve the consistency of measurements and allow more quantifiable results.

Declaration

I certify that this thesis does not incorporate without acknowledgement any material previously submitted for a degree or diploma in any university; and that to the best of my knowledge and belief it does not contain any material previously published or written by another person except where due reference is made in the text.

Albert Ruiz-Vargas

February 20, 2019

Acknowledgements

Firstly, I wish to express my sincere gratitude to my principal PhD supervisor Professor John Arkwright for giving me the opportunity to take this challenge, for his continuous support throughout my candidature, for his patience, and motivation especially when things did not work as expected. I am truly thankful for convincing me to present at scientific conferences. Although I found my first conference to be a challenge, I am currently eager to attend more conferences. Thank you for giving me the opportunity to attend a very exciting conference this year in Hawaii. You always gave me freedom but you knew when to push to achieve more and increase my potential, e.g., your insistence on my first publication, this helped me infinitely to gain the confidence necessary to draft further publications. I will forever be grateful.

Besides my principal supervisor, I would like to extend my gratitude to my second PhD supervisor Associate Professor Antoni Ivorra for his support to take this challenge, for his invaluable guidance on the bioimpedance topic and related research during my candidature. Thank you for always being there on Skype to help me when I needed, and for hosting me in your research group (BERG) in Barcelona at Universitat Pompeu Fabra. Thank you. I would like to thank to Quim Castellví, from the BERG group, for his help during my stay in the group.

Thanks also to Karen Reynolds. Although we only had annual meetings, you always made sure everything was on track.

I also extend my thanks to my team colleagues – Anthony Papageorgiou, Luke Parkinson, Peter Cook, Alex Wall, and Andrew Karas – for their support and for sharing such a good time during my candidature. Thanks also to the staff at Flinders Medical Centre for their help with tissue preparation and protocol experimentation during my candidature.

Thanks also to my industry mentor Tom Melville for his mentoring and support during the last year of my candidature. You always showed interest in my research and helped me develop my network and industry skills but also my personal skills.

A thanks to all the friends I made at the MDRI – Bryant Roberts, Dermot O'Rourke, Dhara Amin, Laura Gell, Sophie Rapagna, Mark Gardner, Rowan Pivetta, Maged Awadalla, Mark Williams, Ashwin Jeyakar – who became part of my personal life and made my time in Adelaide and Flinders University more enjoyable during my candidature – without doubt, best moments were during the Fringe Festival and our trips.

Finally, to my family – Mum, Dad and brother –, to whom I dedicate this thesis, without them my achievements and goals to date would not have been possible. Your support, love and motivation helped me through the most difficult moments, especially, being so far from you. Words cannot express my deep gratitude.

Finalmente, a mi familia – a mis padres y hermano –, a quienes dedico esta tesis, sin ellos, mis logros y objetivos hasta la fecha no hubieran sido posibles. Vuestro apoyo, amor y motivación me ayudaron en los momentos más difíciles, especialmente al estar tan lejos de vosotros. Las palabras no pueden expresar mi profunda gratitud.

Statement of Ethical Conduct

Ethical approval for research undertaken in this thesis was obtained from the Animal Welfare Committee of Flinders University (Animal Ethics Number: 845/12), and the Southern Adelaide Clinical Human Research Ethics Committee (Ethics Approval Number: 50.07). All patients provided written informed consent prior to their involvement.

Publications

A number of publications, conference papers and presentations arose from the work conducted in this thesis. These are listed collectively below, and publications noted individually at the beginning of each relevant chapter.

Journal papers

Ruiz-Vargas, A, Ivorra, A, Arkwright JW. Design, construction and validation of an electrical impedance probe with contact force and temperature sensors suitable for *in-vivo* measurements. *Scientific Reports*. 2018;8(1):14818. doi:10.1038/s41598-018-33221-4.

Ruiz-Vargas, A, Mohd Rosli, R, Wiklendt, L, Arkwright, JW. Effect of electrode separation on High-Resolution Impedance Manometry catheters for *ex-vivo* animal experiments. *Neurogastroenterology & Motility*. 2018;e13488. doi:10.1111/nmo.13488.

Parkinson LA, Cool, PR, **Ruiz-Vargas, A**, Arkwright, JW. Correction of peak tracking Ripple in solid state spectrometers. *Journal of Lightwave Technology*. 2018;36(18): 3912-3918. doi:10.1109/JLT.2018.2854281.

Ruiz-Vargas, A, Mohd Rosli, R, Ivorra, A, Arkwright, JW. Impedance spectroscopy measurements as a tool for distinguishing different luminal content during bolus transit studies. *Neurogastroenterology & Motility*. 2018;e13274. doi:10.1111/nmo.13274.

Conference Proceedings

Ruiz-Vargas A, Ivorra, A, Arkwright, JW. Monitoring the effect of contact pressure on bioimpedance measurements. In: *2018 40th Annual International Conference of the IEEE Engineering in Medicine and Biology Society (EMBC)*. IEEE; 2018:4949-4952. doi:10.1109/IECBES.2016.7843433. Podium presentation

Ruiz-Vargas, A, Arkwright, JW, Ivorra, A. A portable bioimpedance measurement system based on Red Pitaya for monitoring and detecting abnormalities in the gastrointestinal tract. In: *2016 IEEE EMBS Conference on Biomedical Engineering and Sciences (IECBES)*. IEEE; 2016:150-154. doi:10.1109/IECBES.2016.7843433. Podium presentation

Ruiz-Vargas, A, Costa, M, Wiklendt, L, Dinning, PG, Arkwright, JW. The use of fibre optic sensing technology with intraluminal impedance catheter for functional gastrointestinal motility disorders. In: *Australian and New Zealand Conference on Optics and Photonics 2015 (ANZCOP 2015)*. Engineers Australia, 2015: 51-54. Podium presentation

Chapter 1

Introduction

1.1 Motivation

Gastrointestinal disorders (GIDs) can be structural, functional and/or motility (Drossman, 2016). Functional disorders (FD) are those in which the gastrointestinal (GI) tract does not function properly but there is no apparent cause of the malfunction that can be seen with x-ray, endoscopy or blood test; and usually they are diagnosed based on symptoms. Motility disorders (MD) are associated with the abnormal visceral muscle activity. Structural disorders (SD) are those in which the GI tract does not work properly and looks abnormal. Therefore, GI disorders can affect functional, motile, and structural parts of the digestive system causing characteristic symptoms such as heartburn, constipation, irritable bowel, abdominal pain, bloating, diarrhoea or unspecified functional bowel disorders (Drossman, 2006).

To date, the most recent study on the burden gastrointestinal diseases in United states, estimated that between 50 to 60 million US citizens were affected by GI symptoms in 2010 (Peery et al., 2015). The most common GI diagnosis in patients with GI symptoms was abdominal pain accounting for approximately 17 million visits to health care providers, followed by reflux oesophagitis with more than 7 million visits (Peery et al., 2015). Other prevalent disorders and symptoms include haemorrhoids, constipation, nausea and vomiting, abdominal wall hernia, malignant neoplasm of the colon/rectum, Diverticular disease, diarrhoea, dyspepsia, Irritable Bowel Syndrome (IBS) and Chron's disease (Peery et al., 2015).

Furthermore, digestive diseases were the seventh leading cause of death worldwide in 2012 with 2.26 million deaths (American Cancer Society, 2015). According to the American

Cancer Society, based on data from GLOBOCAN12 (Torre et al., 2015), stomach, colon & rectum and oesophagus cancer were the third, the fourth and the sixth leading cancer sites of death in men, and the fifth, the third and the ninth leading cancer sites of death for women in 2012 worldwide (American Cancer Society, 2015). In 2012, an estimated 1.4 million, 951,600 and 455,800 new cases of colon/rectum, stomach and oesophagus cancer occurred worldwide (American Cancer Society, 2015). According to the National Cancer Institute in USA, mortality due to gastrointestinal cancers in 2017 was estimated at 157,700 deaths and there were 310,440 estimated new cases, with 95,520 estimated new cases of colon/rectum. Cancer of the colon/rectum was expected to be the fourth most common type cancer in the US in 2017 (American Cancer Society, 2017). Similarly, in 2017 the second most common cancer in Australia was colon/rectal cancer with 16,682 estimated new cases, and was also the third leading cause of death from cancer (4,114 estimated deaths) (Australian Institute of Health and Welfare, 2017).

In 2004, GI disorders and diseases were responsible for approximately US$ 142 billion in direct and indirect costs (Everhart, 2008). This cost could be significantly reduced if the misdiagnosis rate was reduced. A review of 150 consecutive colorectal cancers at a district hospital in the United Kingdom between August 2010 and July 2011 showed that 8% (12 patients) of the total number had a false negative diagnosis in the first instance (Than et al., 2015). The diagnoses of these 12 false negative cases were delayed in time from 21 to 456 days, and as a result were already in an advanced state at the time of successful diagnosis (5 in stage II, 2 in stage III and 5 in stage IV). Colonoscopy is the gold standard method and also has the lowest miss rate (Frenette and Strum, 2007; Than et al., 2015), however, a study showed the reasons why cancer were missed, one of which was misinterpretation of what was seen (Leaper et al., 2004).

For diagnosing functional disorders, The Rome Foundation classification of GIDs is used (Drossman, 2016). This classification system is based on symptoms rather than physiological changes. However, the overlap of GI symptoms and the limited knowledge of the mechanism of functional GI can incur misdiagnosis, especially in the lower GI tract where it has been shown that most of the GI symptoms are shared by different GIDs (Locke et al., 2005; Talley et al., 2003). A misdiagnosed implies two things: a) the treatment and therapy given to the patient is not cost effective and is often incorrect, and b) patient's correct diagnosis is delayed, thus the cost of the correct treatment might be more expensive.

There is a need for improved or new methods for helping clinicians to diagnose GI disorders and diseases accurately (Fox et al., 2018). A set of available established methods exist in the clinical environment (e.g. colonoscopy, barium enema, antroduodenal manom-

etry, radiopaque markers, scintigraphy, ingestible capsules and so on. More methods are shown in Chapter 2, Section 2.3.1). Other emerging methods are available for research, but not yet available for clinical use (Chapter 2, Section 2.3.2). In the thesis, I present bioimpedance spectroscopy techniques, and in some cases in combination with fibre optic sensing technology, to develop and improved new tools for *in-vivo* diagnostics.

1.2 Aims

The primary aims of this thesis were to contribute to understanding the mechanism of electrical bioimpedance, and develop medical tools/devices for bolus transit studies and tissue characterization in the lower GI tract. The aims, more specifically, were:

Aim 1 To develop a theoretical model of the electrical properties of the GI tract with different tissue layers, shapes and sizes of boluses. This model will allow us to: (1) study the effect of different luminal content during GI studies, (2) study the effect of the electrode separation, and (3) understand how impedance measurements change due to the bolus volume between electrodes.

Aim 2 To develop a custom-made bioimpedance spectroscopy system to distinguish different luminal content by means of complex impedance spectroscopy. This is the first time that complex impedance is used for bolus transit studies and will provide information on the nature of luminal content.

Aim 3 To design and build an impedance manometry catheter using fibre optic sensing technology that has improved spatial resolution compared to existing commercial devices, and compare the results with the numerical results and with the commercial High-Resolution-Impedance-Manometry (HRIM) catheter.

Aim 4 To monitor and control the force applied during bioimpedance measurements using a fibre optic force sensor suitable for *in-vivo* via the port of an endoscope. This is essential for viable *in-vivo* bioimpedance measurements as the effect of contact pressure can significantly affect bioimpedance values.

Aim 5 To standardize bioimpedance measurements based on contact-pressure.

1.3 Thesis outline

The thesis is composed of eight chapters:

Chapter 1 is an introduction to the motivation, outlines the aims, and the structure of this thesis.

Chapter 2 describes the background and provides knowledge on the GI tract and its disorders, a review of pertinent current and emerging methods on GI diagnosis with a focus on bioimpedance methods.

Chapter 3 describes the design and implementation of a method to distinguish between content (**Aims 1 and 2**). To do so, a GI model was implemented to study the passage of a bolus with different content (**Aim 1**); then, the numerical results were compared with experimental results by a custom-made catheter (**Aim 2**) with a four-electrode configuration.

Chapter 4 reports the development of a custom made HRIM catheter based on fibre optic sensing technology (**Aim 3**).

Chapter 5 studies the effect of the electrode separation on HRIM catheters (**Aims 1 and 3**). The same numerical model used in chapter 3 is used to study the effect of the electrode separation (**Aim 1**). Furthermore, four *ex-vivo* studies were performed on excised tissue from rabbits using the custom made HRIM catheter described in Chapter 4 (**Aim 3**) and a commercial HRIM catheter to compare the results with the numerical studies.

Chapter 6 describes the development and validation of a pencil probe for bioimpedance measurements with a fibre optic contact-force sensor (**Aim 4**).

Chapter 7 evaluates the variability of bioimpedance data as a function of contact pressure using the pencil probe developed in Chapter 6 in resected human colonic tissue. A technique is proposed for standardizing bioimpedance measurements based on continuous variations of contact pressure (**Aim 5**).

Chapter 8 concludes this thesis. It presents principal contributions of this work to GI research, limitations and recommendations for future work.

Appendix A introduces the reader to the basics of electrical bioimpedance and fibre optic sensing technology to understand the two main techniques used in this thesis.

Appendix B explains the design, development and validation of the bioimpedance measurement system used in this thesis.

Appendix C contains additional information relevant to Chapter 3 including graphs and statistical results.

Chapter 2

Background and literature review

2.1 Introduction

This chapter introduces to the reader to the anatomy of gastrointestinal tract, and the main structure of the digestive tube at different parts. This is followed by a brief resume of gastrointestinal disorders, and how its classification has become more rigorous thanks to advancements in technology. A brief review of established and emerging techniques is presented, with a more extensive review of electrical bioimpedance technique in gastrointestinal field. As mention in Chapter 1, this thesis has a strong focus on electrical bioimpedance phenomena and fibre optic sensing. The reader will notice that this chapter does not explain the basis of these two concepts; however, a brief explanation on electrical bioimpedance and fibre optic sensing can be found in Appendix A.

2.2 Gastrointestinal tract

The Gastrointestinal (GI) tract is a hollow tube approximately 8-9 meters long. It is responsible for the digestion process. Its main function is to take in food, transport it along the digestive system, process it, absorb nutrients, water and electrolytes and finally eject the waste. The GI tract is formed by different organs; mouth, pharynx, oesophagus, stomach, intestines (small and large), rectum, and anus (Stanfield, 2010). Other organs involved in the digestive system that do not belong to the tract are: pancreas, liver and gallbladder.

2.2.1 Upper GI tract

The **mouth** is the start of the digestive system. Food is broken into pieces, and at the same time, saliva mixes with pieces to lubricate food and to start the digestion process. The food is then passed to the **pharynx**, which connects the mouth with the oesophagus allowing the passage of the food and protecting the airways from aspiration. The oesophagus is connected to the pharynx and the stomach by means of two sphincters: the upper oesophageal sphincter (UOS), which prevents air entering the **oesophagus**, and the lower oesophageal sphincter (LOS) that prevents reflux of gastric contents. It is approximately 25 cm in length, and its main function is to deliver food and fluids to the stomach from the mouth by means of coordinated motor patterns (peristalsis).

The **stomach** is a distensible bag of 2 – 3 litres capacity that receives food and fluids from the oesophagus. The stomach mixes the food with secreted digestive juices with powerful enzymes to break down the food and, finally, to form chyme. The contents are stored in the stomach until these are sufficiently processed; then, the pyloric sphincter, which controls the flow of gastric contents, release the contents to the small intestine (duodenum).

2.2.2 Lower GI tract

The **small intestine** are responsible for ending the digestive and starting the absorptive processes. The small intestine are approximately 6 -7 meters in length, the longest part of the GI tract, and is divided in three parts: the duodenum, jejunum and ileum. In the duodenum, the muscular contractions mix the chyme with bile and pancreatic juices that are released from the bile and pancreatic ducts, segment the content, and push it forwards along the small intestine to the jejunum and ileum where nutrients are absorbed into the bloodstream. The left-over food residue pass to the large intestine predominantly as liquid through the ileocecal valve, which also prevents the return of faeces into the small intestine. During digestion along the small intestine, mucus and gastrointestinal hormones are secreted. The mucus lubricates the mucosal surface and avoids any damage from the bolus during its passage through the intestine, and the gastrointestinal hormones help to control the digestion process.

The **large intestine** runs from the ileocecal junction to the end of the digestive system, and is about 1 m in length. It is divided in seven sections: the caecum and appendix, the ascending colon, the transverse colon, the descending colon, the sigmoid colon, the rectum and the anus. The absorption of water and electrolytes of the chyme occurs along the colon, typically in compartments called haustra, by means of muscular contractions

(segmentation movements and propulsive mass movements). Once the water and electrolytes have been absorbed, the chyme becomes a semi-solid content called faeces. Faecal matter is stored in the sigmoid colon waiting for mass movements to propel the faeces to the rectum and is finally ejected during defecation. Distension of the rectum due to the build-up of faeces triggers an urge to empty the faecal content, but the external anal sphincter prevents this happening until the external anal sphincter is voluntarily relaxed and the rectal muscles contract to evacuate the content.

2.2.3 Gastrointestinal structure

The GI wall has between three and four layers along the GI tract but with differences in the structure to adapt each of them to their specific function. Four layers from the lumen (the internal volume of the GI tract) towards the outer surface form the GI wall structure: mucosa, submucosa, muscularis (circular and longitudinal) and serosa (oesophagus lacks the serosal layer). Figure 2.1 shows how sub-layers also form the different layers of the GI tract.

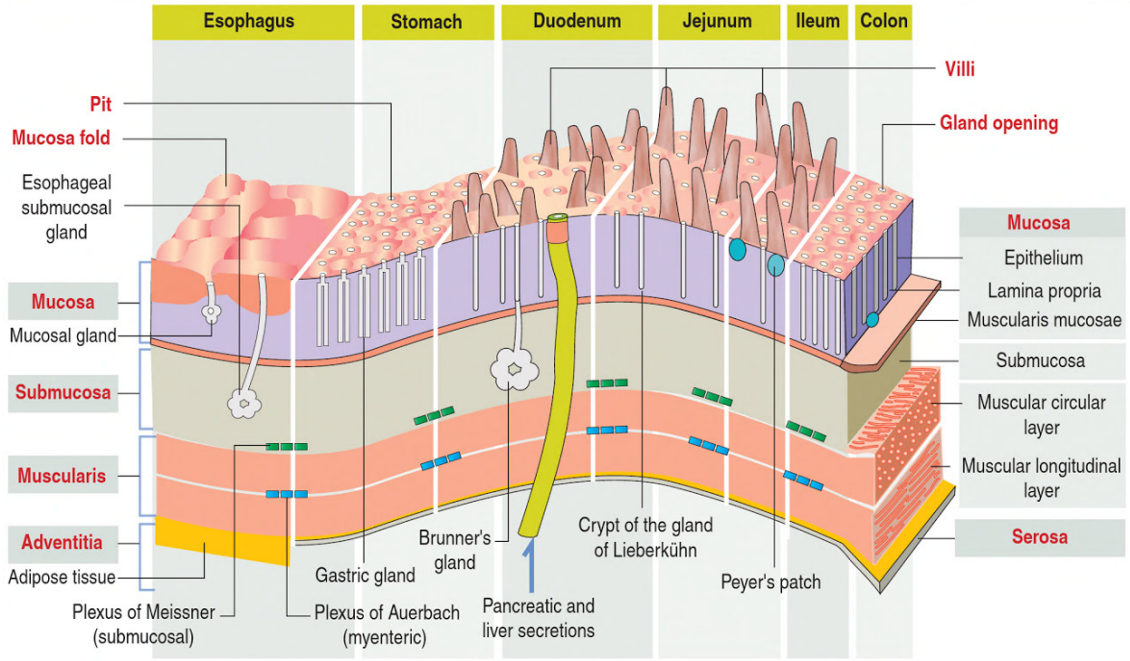

Figure 2.1: Different layers of different digestive parts. Reproduced with permission from Elsevier Health Sciences, from Kierszenbaum and Tres (2015).

The **mucosa** is composed of three different layers: epithelium, lamina propria and muscularis mucosae. The epithelium is the layer in contact with the luminal content, and variations exist between different parts of the GI tract. E.g. oesophagus has a squamous, stratified but not keratinized epithelium, while stomach, small and large intestine have a

simple columnar epithelium with variances (Kierszenbaum and Tres, 2015). The stomach also has thick longitudinal folds, rugae and tiny surface invaginations. The small intestine is characteristic for having microscopic villous and macroscopic plicae with absorptive cells. Large intestine has transverse mucosal fold, plicae semilunares with haustral sacs between the folds.

The middle-layer or **lamina propria**, contains lymphatics (except in the large intestine), and blood vessels, lymphocytes and plasma cell. The muscularis mucosae, which is the outer layer of the mucosa, is composed of inner circular and outer longitudinal layer of smooth muscle, except for the oesophagus which only has longitudinal muscle.

The **submucosa** layer is mainly composed of loose connective tissue, vessels and Meissner's nerve plexus for all the parts of the GI tract except the stomach that has connective tissue with elastic fibres with prominent blood vessels. Oesophagus also has a lymphovascular network with developed venous plexi and glands.

The **muscularis** layer is composed of two layers of muscle: circular muscle (inner) and longitudinal muscle (outer); the Auerbach's nerve plexus is found between these two layers. This layer tends to be thicker in the intestines in order to propel the bolus forward (peristalsis). Unlike the rest of the GI tract, the oesophagus presents striated muscle in the upper, smooth in the lower and mixed in the middle. The stomach has three indistinct layers: an inner oblique, middle circular and outer longitudinal layers.

The **serosa** layer is the outer most layer of the GI wall and is composed of connective tissue. The oesophagus also has thick nerves, blood vessels and lymphatics.

2.2.4 Gastrointestinal disorders and diseases

In Chapter 1, functional, motility and structural gastrointestinal disorders, GIDs, were briefly introduced. Table 2.1 shows a quick summary of primary domain, criterion and measurement of the different GIDs. Obviously, functional, motility and/or structural GIDs can sometimes coexist together. For example, a structural alteration such as ulcerative colitis can be associated with symptoms of pain and diarrhoea and also disturb motility (Drossman, 2016).

Furthermore, there is little known about the underlying causes of some functional gastrointestinal disorders (FGIDs), which makes them difficult to diagnose as it is based on symptoms provided by the patient. The Rome classification (latest version (Drossman, 2016)) attempts to rigorously document FGIDs based on our current understanding, in

Table 2.1: Summary of major clinical domains and its criterion and measurement in gastroenterology. Reproduced with permission from Elsevier, Rome IV Drossman (2016)

	Gastrointestinal disorder		
	Functional	**Motility**	**Structural**
Primary domain	Illness experience	Organ function	Organ morphology
Criterion/Condition	Symptoms	Altered motility	Pathology (disease)
Measurement/Diagnostic method	Motility Visceral sensitivity Symptom criteria (Rome)	Motility Visceral sensitivity	Histology Pathology Endoscopy Radiology

which all the FGIDs are well documented. More information about the current FGIDs, symptoms, treatment and so on, from the Rome criteria can be found in (Aziz et al., 2016; Galmiche et al., 2006; Lacy et al., 2016; Longstreth et al., 2006; Rao et al., 2016; Stanghellini et al., 2016; Tack et al., 2006; Van Oudenhove et al., 2016). The Rome criteria has been updated since its first version in 1994 (Rome I) approximately every 6 years (Camilleri, 1995; Mostafa, 2008; Spiller, 2000), except the last edition published in 2016 that took 10 years to update (Drossman, 2016). Every new version has been updated or modified with sub-types disorders, changes in classification categories, criteria changes and corrections of terminology.

These changes are in part due to the better understanding attributed to the increase in study numbers in GIDs, the use of current techniques in other fields, and advancements in technology. A clear example is the use of brain-imaging techniques for GIDs that has helped to understand the psychosocial factors and its inclusion in the Rome criteria. Most importantly, its use brought insight on how these factors affect the GI function in healthy subjects, and in patients with FGIDs (Van Oudenhove et al., 2016).

Another example, reflux hypersensitivity diagnosis was included in the most recent Rome criteria (Rome IV). In the previous version (Rome III), reflux hypersensitivity was diagnosed as a functional heartburn disorder when there was normal acid exposure with positive symptom of reflux association (Aziz et al., 2016), but with the consensus of the clinical community, and the combination of pH and impedance catheters, it is now possible to identify/categorise refluxes with normal acid exposure (reflux hypersensitivity).

Furthermore, studies of normal GI function (colonic motility) to gain a greater insight into the physiology were performed, and even though these attempts to understand the physiology of the lower GI tract, this is still poorly understood as reported in a review by Dinning (2018).

It is obvious, that accurate diagnosis and sub-characterisation are often difficult and that a better understanding of normal GI function is needed. Therefore, more studies and improved diagnostic devices are needed to better characterize and understand the GIDs and their subtypes in order to treat disorders appropriately.

2.3 Methods of diagnosis for GIDs

In this sub-section, the different methods for diagnosing and evaluating GIDs are briefly presented. Firstly, the established methods in clinical environment are described, and secondly the emerging methods (still in research, not yet used as a clinical tool) are presented.

2.3.1 Established methods

Manometry

Manometry studies allow the measurement and evaluation of peristalsis and other muscular contractions along the gastrointestinal tract via the use of a small diameter catheter containing one or more pressure sensing elements along its length (Szarka and Camilleri, 2009).

High-Resolution Manometry

In the past 3 decades, high resolution (HR) manometry catheters with closer pressure sensor separation (spaced = 10 mm) have emerged for similar studies. These studies have been shown to be a powerful method to classify different functional gastrointestinal motility disorders (Pandolfino and Kahrilas, 2009).

Combined impedance-pH catheters

Multichannel intraluminal impedance (MII) and pH monitoring catheters were initially used as two separate instruments (Kahrilas and Sifrim, 2008). MII catheters were used for monitoring and studying the passage of bolus (Nguyen et al., 1999; Silny, 1991; Silny et al., 1993), whereas pH monitoring catheters were used for detecting changes in acid content in the oesophageal tract (Bredenoord and Smout, 2013). Combined multichannel intraluminal impedance (MII) and pH (MII-pH) catheters allow practitioners to diagnose and classify functional disorders (heartburn and reflux hypersensitivity) and motility disorders (gastroesophageal reflux disease) (Tutuian, Vela, Shay and Castell, 2003). Basically, intra-

luminal impedance detects the presence of reflux and its content, and the pH characterises the reflux as acid versus non-acid.

Combined impedance and HR manometry catheters

Similarly to the impedance - pH devices, impedance and high resolution manometry are also combined to provide greater diagnostic capability. This is known as High-Resolution-Impedance-Manometry (HRIM) catheter and is conventionally used for oesophageal studies (Kahrilas and Sifrim, 2008). The HRIM catheters provide a better understanding of the intraluminal pressures changes, LOS relaxation and bolus transit in the oesophageal lumen (Tutuian, Vela, Balaji, Wise, Murray, Peters, Shay and Castell, 2003).

Radiopaque markers

Radioopaque or radioisotope markers are ingested in order to follow their progression along the colon by means of a set of radiographs or other imaging technology of the abdomen. This method is useful to measure colonic transit and to differentiate slow colonic transit and functional faecal retention, however, it is not viable for assessment of small bowel function since it can be difficult to anatomically locate the markers (Szarka and Camilleri, 2012). In addition, the necessity of multiple radiographs and nuclear medicine make this technique less acceptable when repeated evaluations are necessary (Cook et al., 2005).

Barostat

The barostat studies monitor changes in tone, compliance and sensation within the gastrointestinal tract by inflating a balloon to a known constant pressure. The volume of air and/or change in volume can be used to assess the function of the gastric fundus, gastrointestinal lumen, or rectum. It is an invasive technique that involves the introduction of an intraluminal bag into the section of the GI tract being studied and then inflating the bag to a predetermined pressure. This pressure is held constant by means of injecting or aspirating air when the surrounding organ contracts or relaxes(Sarnelli et al., 2001). The limitations of this method are that the presence of an intraluminal bag interferes with gastrointestinal physiology and the contraction patterns are irregular (Zwart et al., 2003).

EndoFLIP

EndoFLIP is a similar concept as the barostat bag, but instead of pumping air into the bag a saline solution is injected, and simultaneously an array of electrodes along inside the balloon measures the cross-section area along it (impedance planimetry) (Mary et al., 1979; McMahon et al., 2005). Its main application is for assessment of oesophageal luminal cross-section during volumetric distension. Similarly to the barostat method, a limitation

is the assessment of the intraluminal bag (10 cm in length) that is reported by a single pressure value when the pressure profile along the balloon will be irregular (Carlson et al., 2015), but the EndoFLIP allows the cross-sectional shape of the bag to be monitored so it is an improvement on the barostat.

Ingestible capsules

Ingestible capsules are devices that mimic the shape of a standard pill and contain sensors capable of recording information such as pH, pressure, temperature and video images. For example, the SmartPill GI monitoring System transmits wireless data on intraluminal pressure, pH and temperature as it moves throughout the gastrointestinal tract (Cassilly et al., 2008). It can evaluate the transit time throughout the gastrointestinal system (upper and lower gastrointestinal). Another example of ingestible capsule is the Pillcam, which records video images in order to determine gastric emptying, and transit times through oesophagus, small bowel and colon (Li et al., 2014). A smaller Magnetic Pill, which is tracked with a magnet tracking system, is also available. Its dimensions are generally smaller than the other ingestible capsules. The Magnet Pill can obtain the transit times and 3D configuration which makes it really valuable tool (Stathopoulos et al., 2005).

Ingestible capsules are unable to detect coordinated pressures at multiple locations within the gut. Moreover, ingestible capsules are not suitable for those patients with obstructive gastrointestinal symptoms (Tran et al., 2012).

Scintigraphy

This is the gold standard technique for gastric emptying. The scintigraphic measurement can also evaluate whole and regional transit times (Madsen, 2014). The technique consist of an oral ingestion of a radiolabelled (gamma-emitting, e.g. ^{99m}Tc and ^{113}In) solid, liquid or mixed meals, then multiple images are taken of the region of interest with a gamma camera.

Breath testing

Two main breath tests are used in clinical studies; ^{13}C breath test and hydrogen breath test. The ^{13}carbon-labelled octatonic acid is used for gastric emptying studies whereas the hydrogen breath test is used for orocaecal transit studies (Madsen, 2014). In the first instance, the test consists of ingesting ^{13}C mixed with a meal. Once the substance has passed to the small intestine, the meal is digested and absorbed, and ^{13}C is excreted in the breath as $^{13}CO_2$ (Madsen, 2014). The hydrogen breath test consists of ingesting non-digestible carbohydrates (e.g. lactulose with rice), when the carbohydrates reach the colon colonic bacteria produce hydrogen gases through fermentation. The hydrogen is

then diffused across the mucosa to be transported to the lungs and excreted in the breath (Madsen, 2014).

Ultrasonography

Ultrasonography (US) consists of acquiring real-time imaging of soft tissue. It is used to assess injuries in muscles, malfunction of heart or any other organs. Its use in gastroenterology is not well established but some countries use it for assessing gastric emptying (Odegaard et al., 2015), and monitoring anal sphincter damage (Albuquerque, 2015). It is a non-invasive technique and can be repeated several times.

On the other hand, the combination of US and endoscopy has become useful for classifying stages of oesophageal, gastric, rectal cancer, sub-epithelial lesions in the GI tract, and anal sphincter function (Abdool et al., 2012; Shami and Waxman, 2005). In fact, in some areas such as anal sphincter, US became as the gold standard for evaluating anal sphincter pathology. However, in other areas, it has not become yet used as a gold standard due to limitations such as concomitant treatment with drugs which can inhibit gastrointestinal motility, inadequate visualization of the antrum or other soft tissue landmark points, and possible errors due to the presence of air bubbles and antral contractions (Portincasa et al., 2000).

Endoscopy

Endoscopy usually refers to a flexible tube with a single or multiple ports that is introduced through either the upper or lower GI tract to introduce white light with a camera and biopsy forceps to visualize, inspect and collect samples in order to be later analysed in the laboratory. This procedure requires a highly-qualified user as it relies on the user's experience to select, inspect the area and make the decision to collect the sample. Furthermore, it cannot evaluate the whole part of the small bowel, only the first and last part of the GI tract.

2.3.2 Emerging methods

Electrogastrography

Electrogastrography (EGG) is a technique that records bio-potentials associated with the stomach and is similar to other techniques well established in the clinical area, such as electrocardiography (ECG) or electroencephalography (EEG). EGG measures the gastric slow waves from the abdominal surface with cutaneous electrodes (Ogawa et al., 2004), but does not measure contractions or emptying (Verhagen, 2005). This method, however,

is not well established as a diagnostic tool because of its poor correlation between EGG findings and symptoms and overlaps between healthy volunteers and patients (Abid and Lindberg, 2007).

Combined impedance and HR manometry catheters

As seen in the established methods subsection, these tools are already in use for the diagnosis and sub-classification of oesophageal disorders; however, their use for assessment of small bowel, colonic motility and bolus transit – bowel disorders – are not yet established. Nonetheless, its use in research is becoming more common for gaining insight on the motor complex patterns in the small and large bowel (Costa et al., 2013; Dinning et al., 2011; Dinning, Costa, Brookes and Spencer, 2012; Dinning, Hunt, Arkwright, Patton, Szczesniak, Wiklendt, Davidson, Lubowski and Cook, 2012; Dinning et al., 2013, 2014; Kuizenga et al., 2014). Most of the outcomes of these studies are presented by Dinning (2018).

Electrical bioimpedance

Electrical bioimpedance, and/or impedance consists of measuring electrical properties of biological tissue at a given frequency. When different frequencies are being used, then, the terminology is referred as impedance spectroscopy (more information can be found in Appendix A). Impedance spectroscopy has been used in research environments in the gastrointestinal tract for the last 20 years, although it has not got as much attention as other forms of diagnosis. Impedance spectroscopy has been used to distinguish/classify tissue malignancies in the oesophageal tract and stomach (González-Correa et al., 1999), to discriminate gastroesophageal reflux disease (GERD) from Non-GERD conditions (Ates et al., 2015), and to monitor ischemic injury on the intestinal mucosa (Kassanos et al., 2015; Othman et al., 2003). Although impedance spectroscopy is mainly used for tissue characterization, attempts to assess the gastric emptying of food by means of electrical impedance tomography (EIT) have also been tested. EIT is a variant of impedance spectroscopy but with multiple measurement sites used to build up an image based on the different electrical properties of the volume of interest (Podczeck et al., 2008; Smallwood et al., 1994).

Magnetic resonance imaging

Magnetic resonance imaging (MRI) consists of acquiring a sequence of images of an area of interest which are then put together in order to obtain a video. MRI has been extensively used as a clinical tool in some areas (e.g. neuroscience, cardiovascular, musculoskeletal, angiography, and so on); however, in gastroenterology its use is predominantly as a research tool. MRI is currently being evaluated for gastrointestinal motility (de Jonge et al.,

2018), assessment of gastric emptying (Menys et al., 2017), small bowel movements (Menys et al., 2013; Wakamiya et al., 2011) and colonic motility (Hoad et al., 2016). The lack of standardization and the difficulty of data interpretation have prevented MRI being used as a clinical tool as yet (de Jonge et al., 2018).

2.3.3 Summary

A summary of the different methods with their purpose and regions of use are shown in Tables 2.2 and 2.3. Interestingly, the established methods are mainly focused on the diagnosis of the upper GI tract, especially in the oesophagus. Only a few established methods are focused on the lower GI tract; however, these devices are mainly focused on transit times and not in motility, which may bring insight on some of the GIDs.

Table 2.2: Established methods.

Established method	**Purpose**	**GI part**
Antroduodenal manometry	Motility	Oesophagus
Impdance - pH	Transit, refluxes	Oesophagus
Ultrasonography	Transit	Whole GI
Scintigraphy	Transit	Stomach and small intestine
High-Resolution manometry	Motility	Oesophagus
Impedance & HR manometry	Motility, transit	Oesophagus
Barostat & EndoFLIP	Motility	Upper GI
Hydrogen breath testing	Transit	Small intestine
Wireless motility capsule	Motility, transit	Whole GI
Radiopaque markers	Transit	Whole GI
Endoscopy	Visualization, biopsy	Whole GI

Table 2.3: Emerging methods.

Emerging method	**Purpose**	**GI part**
MRI	Motility, transit	Whole GI
High-Resolution manometry	Motility	Colorectal
Impedance & HR manometry	Motility, transit	Colorectal
Electrical impedance	Tissue characterization, biopsy	Whole GI
Electrogastrography	Gastric slow waves	Lower GI

This subsection has not attempted to undertake a thorough review of emerging diagnostic

techniques, but to address those related to diagnose motility problems. Further details of emerging techniques can be found in the following references (Chao et al., 2013; Kassanos et al., 2015; Podczeck et al., 2008; Smallwood et al., 1994).

For the purpose of this thesis, I am going to focus on the electrical bioimpedance and impedance spectroscopy methods for the lower GI tract. Thus, an extensive review on the most common methods for the GI tract is presented in the next section.

2.4 Studies using electrical impedance and bioimpedance spectroscopy for GI disorders

The first impedance catheter for GI tract was reported by Silny (1991). He built an impedance catheter of nine thin metal ring electrodes mounted on the lower part of a 2-m-long plastic catheter with a diameter of 3 mm, an electrode length of 4 mm with 2 cm spacing between electrodes. He used this catheter for the study of bolus transit along the GI tract. He used an impedance-voltage transducer to measure the magnitude of the impedance, at a measurement frequency of 1 kHz and measurement current < 6 µA (Silny, 1991).

After Silny's first reported use of impedance, numerous studies have been conducted with impedance alone, and in combination with pressure and pH sensors. Since this pioneering work, commercial systems from (Sandhill EFT catheter; Sandhill Scientific Inc. – Diversatek Healthcare, Highlands Ranch, CO, USA) and (Solar GI HRIM, Medical Measurement System - Laborie, Mississauga, ON, Canada) have been used in many studies for recording impedance, pressure and pH measurements (Nguyen et al., 1999; Srinivasan et al., 2001; Tutuian, Vela, Balaji, Wise, Murray, Peters, Shay and Castell, 2003; Tutuian, Vela, Shay and Castell, 2003). These studies only reported a single impedance parameter, as reported by Silny, which was the absolute value of the impedance. Silny reported the frequency that he used for the impedance measurements, however, in these subsequent studies the frequency used for the impedance measurement is unknown owing to the use of commercial systems.

Commercial intraluminal impedance catheters – sometimes in combination with pressure and/or pH sensors – have been used in order to monitor, assess and diagnose different functional gastrointestinal motility disorders in the upper GI tract. Studies have also been conducted using simultaneous video-fluoroscopy (Kahrilas and Sifrim, 2008). In 2013, impedance and manometry studies in conjunction with video recording of changes in diameter in *ex-vivo* animal models were done by Costa et al. (2013), that revealed in-

teresting insight in the motor activity of the colon by means of a combination of pressure, impedance, and diameter data. These studies have also shown that admittance (the inverse of impedance) and the diameter of the specimen are in good agreement. Recently, Omari et al. (2014) demonstrated that using impedance in pharyngeal-oesophageal studies in conjunction with video-fluoroscopy in human beings also provides a means for quantitatively determining changes in internal diameter of the lumen to predict risk of aspiration. However, impedance is not only dependent on geometry; it also depends on the electrical properties of medium. In this instance, the experiments were done with a bolus of constant conductivity – a parameter that can be easily controlled in the oesophagus, however, in regions below the stomach the conductivity of the medium cannot be well controlled making this form of measurement more challenging.

Further to the oesophageal studies, Al-Zaben and Chandrasekar (2004, 2005) conducted simulations of an oesophageal model to study the configuration parameters – such as electrode separation, electrode length and electrode diameter – on impedance catheters. He demonstrated that space between electrodes was crucial for identifying the minimum bolus length.

The first use of electrical impedance spectroscopy on GI tract, specifically in resected oesophagus and stomach tissue from humans and rats, was reported by González-Correa et al. (1999). He used a 3.2-mm-diameter and four-electrode probe. By looking at the electrical properties, at a frequency range of 9.6 kHz to 614.4 kHz, of squamous and columnar epithelium, he could differentiate between these two epithelial structures.

Gonzalez-Correa went on and performed a most thorough *ex-vivo* study on human tissue to compare the resistivity values of squamous and columnar epithelium (Gonzalez-Correa et al., 2003). Their bioimpedance techniques found statistically significant differences ($p < 0.05$) between non-inflamed columnar tissue (4.9 Ωm) from inflamed (4.2 Ωm) and dysplastic (3.4 Ωm) columnar tissue (Gonzalez-Correa et al., 2003). However, no significant differences were found between non-inflamed and inflamed squamous tissue and inflamed and dysplastic columnar tissue.

In 2001 a research group from "*Universidad Autonoma Metropolitana*" based in Mexico (Iztapalapa) patented a new impedance catheter for ischemic mucosal damage monitoring in hollow viscous organs (Rock, 2012). The probe designed and employed by this group is composed of 4 Ag/AgCl ring electrodes of 5.4mm in diameter, 0.5mm in length, and 1.5mm spaced from each other. Complex impedance and impedance spectroscopy data was used (four-electrode configuration) over a range of frequencies (100 Hz - 1 MHz) to measure, identify and classify different levels of ischemic injury in gastric mucosa in human

and animal models in order to detect multiple organ failure due to hypoperfusion or shock (Beltran et al., 2013, 2006; González et al., 2007; Gonzalez et al., 2003; Othman et al., 2003). This study used the so-called 'Cole parameters' (see Appendix A, Section A.2.4) to evaluate the complex impedance data at different frequencies in order to assess the health of the gastric mucosa (Beltran et al., 2006). In these studies, the reactance of the complex impedance (in Ω) was found out to be a very good predictor and diagnostic tool of ischemic damage in gastric tissue, as it is insensitive due to changes in gastric contents and the electrode to mucosa interface impedance (Beltran et al., 2013; Beltran and Sacristan, 2015).

In 2005, an *ex-vivo* study on resected gastric tissue of rats and humans again conducted by the Gonzalez-Correa group determined that the bioimpedance measurements had a pressure dependency – e.g. gastric human (columnar epithelium) tissue had an increment of 80% for an exerted pressure range of 1 kPa to 5 kPa (González-Correa et al., 2005). The increase in resistivity is much higher than the small difference between non-inflamed columnar tissue and inflamed or dysplastic columnar tissue showed in (Gonzalez-Correa et al., 2003). Gonzalez-Correa concluded there is a need for controlling the contact force of probe with sample during bioimpedance measurements, especially *in-vivo* situations.

These studies cannot precisely represent *in-vivo* situations, where the tissue is not supported by a hard surface and contact pressure is not constant over time. In addition, an *in-vivo* study in dogs done by Lundin et al. (2011) showed a large variability in resistivity values using a similar probe as described above – even though only one investigator was used to standardize the measurements –, possibly due to uncontrolled variations in contact pressure between the probe and the mucosa.

In 2011 a research group from "*Tabriz University of Medical Science*" based in Iran (Tabriz) presented its first and only study related to electrical bioimpedance of normal and abnormal gastric tissue (Keshtkar, Salehnia, Somi and Eftekharsadat, 2012). Additionally, this research group has a very strong background in impedance spectroscopy measurements on bladder and cervical tissue (Keshtkar et al., 2006; Keshtkar, Salehnia, Keshtkar and Shokouhi, 2012; Smallwood et al., 2002), where he concluded that probe size had an effect on the bioimpedance variability – the larger the probe, the less variability since avoids the expulsion of fluid below the tip (Keshtkar and Keshtkar, 2008). Nonetheless, due to the size limitations of an endoscope port, a probe of 2 mm diameter – similar configuration as Gonzalez-Correa used in his studies – with four gold wire electrodes of 0.5 mm diameter located in the tip was designed for the gastric tissue studies.

Different types (normal, benign, dysplastic and adenocarcinoma) of gastric tissue in hu-

man beings were measured *in-vivo* with the probe over a range frequency from 470 kHz to 1 MHz. Similarly, the contact pressure was not controlled in this study, and the results exhibited a large variability with overlapping resistivity values among the groups. Significant differences ($p < 0.05$) between resistivity values of normal group and malignant group were also observed. Nonetheless, overlapping resistivity values among the groups were observed, which precludes any rigorous classification of individual measurements (Keshtkar, Salehnia, Somi and Eftekharsadat, 2012).

Although research into bioimpedance for GI applications is growing, there are still multiple issues to address before it can be included as a viable diagnostic test. These issues include:

- How can the varying conductivity of different luminal content be addressed? Especially below the stomach where the nature of the content is not fully known.
- Lack of HRIM catheters with closer electrode separation. Could an HRIM catheter with closer electrode separation be beneficial for GI motility studies?
- How can the uncontrolled contact pressure exerted during bioimpedance measurements be addressed in order to get more reliable and consistent measurements?

Chapter 3

Distinguishing different luminal content

The study presented in this chapter is the subject of the following paper:

Ruiz-Vargas, A, Mohd Rosli, R, Ivorra, A, Arkwright, JW. Impedance spectroscopy measurements as a tool for distinguishing different luminal content during bolus transit studies. *Neurogastroenterology & Motility*. 2018;e13274. doi:10.1111/nmo.13274.

3.1 Introduction

The electrical impedance method has been widely used for electrochemistry (Fischer et al., 2011; Khafaji et al., 2011), food inspection (Abdul Rahman et al., 2014; González-Sosa et al., 2014) and biomedical applications (Nowakowski et al., 2005). The use of impedance measurement in gastrointestinal studies is gaining popularity among clinicians for studying bolus transit, motor patterns, and disorders along the gastrointestinal tract (Dinning et al., 2010; Pandolfino and Kahrilas, 2009). Intraluminal impedance has been used in the human oesophagus to record the transit of a controlled bolus, to measure the internal diameter, to differentiate between acid and non-acid reflux, and to predict risk of aspiration (Nguyen et al., 2013; Rommel et al., 2014; Zifan et al., 2015). In addition, it has been shown that impedance measurements can be used to quantify the internal diameter in a rabbit colon in a controlled *in-vitro* environment (Costa et al., 2013). However, using impedance recordings to measure transit in the human colon is not straightforward, as the content cannot be controlled and may include liquid, gas, solid or a mixture of these at any one time.

Electrical impedance can be obtained at a single frequency but it can also be taken across a range of frequencies. When this is done, it is referred to as electrical impedance spectroscopy. In living tissues, the impedance measurements will not be constant across the range of frequencies. The variation in response is due to the electrolytic and dielectric nature of biological tissue. Biological tissue can be thought of as cells with dielectric membranes and junctions containing conductive fluid floating in a sea of similar conductive extracellular fluid. At low frequencies, the electric current predominantly flows through the conductive extracellular liquid whereas at high frequencies the cellular membranes act as the dielectric in a capacitor allowing current flow through both the extracellular fluid and the cells themselves.

Commercially available equipment (e.g. Solar GI HRM, Laborie/MMS, Mississauga, ON, Canada and InSight GI, Diversatek Healthcare/Sandhill Scientific, Germatown, Wisconsin USA) being used in clinical environments only measure impedance magnitude and do not provide information on the real and imaginary components of impedance; hence important information of the nature of the gastrointestinal wall and surrounding tissue may be lost. Furthermore, the frequency used for impedance measurement is typically not provided by equipment manufacturers. The first report of gastrointestinal intraluminal impedance measurement by Silny, who quoted a measuring frequency of 1 kHz (Silny, 1991). Since this initial publication, information on the measuring frequency used – from impedance acquisition system (InSight GI) – to derive impedance measurements is rarely provided,

the only exception to this that I am aware of is the work by Ates et al. (2015) who reported a frequency of 2 kHz for mucosal impedance discrimination without giving any reason for using such frequency.

The aim of the present study is to determine whether impedance spectroscopy (**Aim 2**) can be used to differentiate two different forms of luminal content (liquid and gas) in an excised section of guinea pig colon. I report an investigation into the spectral characteristics of intraluminal impedance measurements conducted in an *in-vitro* organ bath that provides insight into the effect of varying the frequency and an associated numerical model. I provide recommendations for the best frequencies to use in different situations.

3.2 Materials and methods

3.2.1 Catheter design

A custom designed four-electrode catheter was built for this experiment (Figure 3.1). Four silver ring electrodes were assembled along a 3.5 mm diameter cylindrical piece of PEEK (Polyether Ether Ketone). The electrodes were 1 mm in length and were separated by 1 mm intervals. The cylinder containing the electrodes was then attached to a length of PTFE (PolyTetraFlouroEthelene) tube of 3 mm outer diameter (Figure 3.1). The surface electrodes were roughed with sandpaper to minimize the tissue/electrolyte interface impedance and to fix the half-cell potential that appear between metallic conductors and biological tissue and that commonly cause impedance measurement errors (Grimnes and Martinsen, 2008).

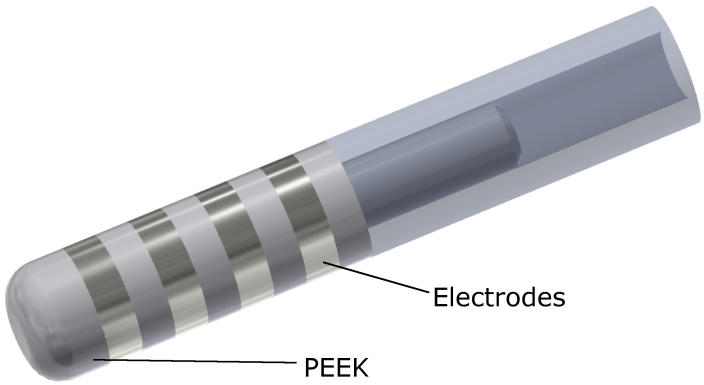

Figure 3.1: 3D model of impedance catheter used for the experiment and numerical study.

3.2.2 Equipment

Two sets of data were recorded during the experiments: impedance spectroscopy and the external diameter of segments determined from synchronous digital video imaging. This allowed us to directly measure the bolus transit at different measuring frequencies, compare them and correlate the impedance measurements with the external luminal diameter.

A digital video camera (iPhone 6, Apple, Cupertino, California, USA), positioned above the preparation was used to record video images to create spatiotemporal maps of changes in diameter, referred to as 'Dmaps'(Hennig et al., 1999).

The four-electrode catheter was connected to a custom-made bioimpedance measurement system (BMS), based on a Red Pitaya board (Redpitaya v1.1, Redpitaya, Slovenia), which is capable of measuring impedance from 10 Hz to 1 MHz (more information about the system can be found in the Appendix B). The unit used a tetrapolar configuration for measuring the complex impedance; an alternating current with a maximum amplitude of 10 µA was applied between the two outer electrodes at each predetermined measuring frequencies, and simultaneously the voltage drop between the inner electrodes was measured. The complex impedance at five different frequencies (from 1 kHz to 1MHz separated logarithmically) was calculated using the onboard processor of the Red Pitaya unit. Impedance data was sent in real time to a custom software application built in LabVIEW (National Instruments, Austin, Texas, USA) to be saved and displayed. The impedance spectrograms were acquired at 10 samples per second which is an adequate sampling rate for oesophageal transit testing, in which bolus transit passes considerably faster than in the human colon, estimated by Bredenoord et al. (2004).

3.2.3 *Ex-vivo* study

A section of a proximal colon from a guinea pig was used. The section was removed from the laboratory animals by methods approved by the Animal Welfare Committee of Flinders University (Animal Ethics Number: 845/12). The removed section of colon was placed into a beaker containing oxygenated Krebs solution (in mM: $NaCl$, 118; KCl, 4.7; NaH_2PO_4, 1.0; $NaHCO_3$, 25; $MgCl_2$, 1.2; *D- Glucose*, 11; $CaCl_2$, 2.5) and bubbled with 95% O_2/ 5% CO_2. The faecal pellets were gently flushed out of the colonic segment with Krebs solution.

The excised section of gut was then placed into an organ bath containing the same Krebs solution warmed to 37°C. Spontaneous gut contractile activities could be present for hours

while within the organ bath.

In the organ bath, the anal and oral ends of the proximal colon were attached to T-shaped plastic connectors (Figure 3.2). The catheter was passed through the T-shaped connector at the oral end and the vertical arm of the T-piece was connected to an infusion pump. In the first part of the experiment, warm Krebs (36 - 37°C) solution was infused at 2 ml/min through the oral end of the specimen to stimulate contractile activity. In the second part of the experiment, ambient air was infused using the same infusion pump at the same infusion rate. In both instances, the experiment lasted for 60 minutes, and after initial recording of free flow through the gut, the anal end of the segment was blocked causing the gut to swell to large diameters around the four-electrode catheter.

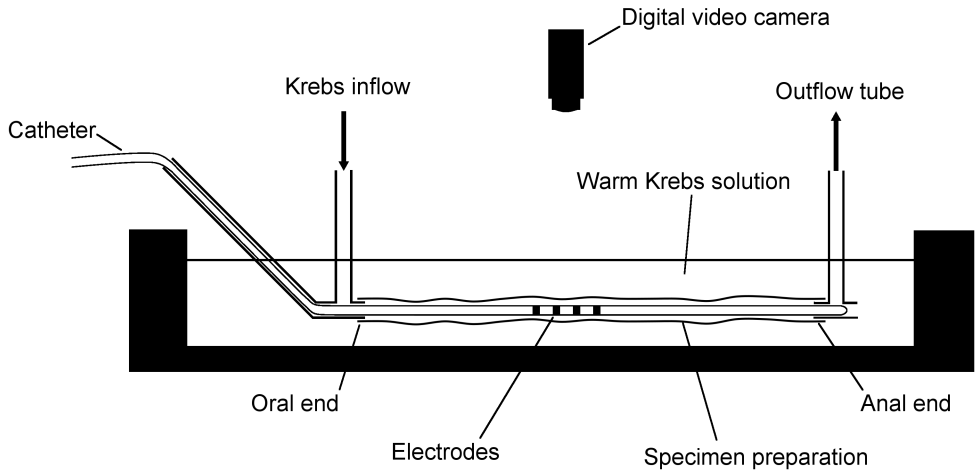

Figure 3.2: Experimental set-up.

3.2.4 Numerical study

A model of the gut section was developed in Autodesk Inventor 2017 (Autodesk, San Rafael, California, USA) and used for simulating transit of different conductivity content along the segment. The segment model consists of a hollow tube (length = 150 mm) composed of eight regions: luminal content, mucus layer (thickness = 50 µm), mucosa layer (thickness = 900 µm), submucosa layer (thickness = 800 µm), circular muscularis layer (thickness = 450 µm), longitudinal muscularis layer (thickness = 450 µm), serosa layer (thickness = 50 µm) and surrounding tissue (thickness = 7 mm) (Kassanos et al., 2015). A catheter (length = 150 mm; outer diameter = 3.5 mm) with four ring electrodes (length = 1 mm; outer diameter = 3.5 mm) was positioned on the axis of the tube. Then, a specific shape bolus (Figure 3.3) with an outer diameter of 10 mm was created. Twenty-six different static models were created changing the bolus position by 2.5 mm each time to

simulate bolus propulsion and the impedance was simulated for each bolus location using the DC electrical conduction component of the ANSYS Finite Element Method (FEM) software platform (ANSYS Electronics desktop, ANSYS Inc, Canonsburg, Pennsylvania, USA). Each simulation was carried out on 12 CPUs Intel ® Xeon ® CPU E5 – 2630 v2 running at 2.60 GHz with 128 GB of RAM, with OS Windows 8.1 Enterprise. The models were solved using 3D models method. The meshes used in the FEM simulations varied from model to model but were composed from 465569 to 6329027 tetrahedral elements, depending on the complexity.

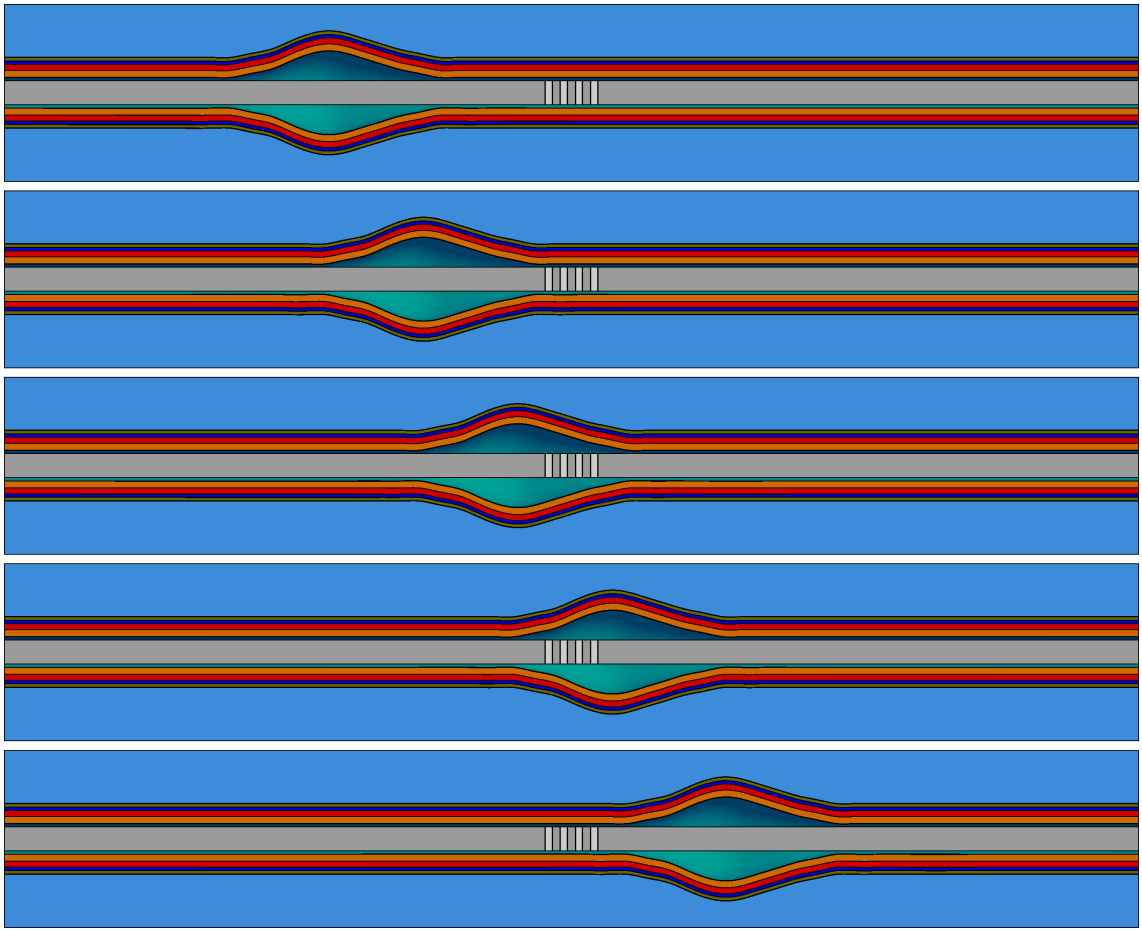

Figure 3.3: Lateral cross-section views of the 3D gastrointestinal model with electrodes. Bolus travels from left to right mimicking the passage of a bolus along the specimen with all its layers from inside to outside (mucosa, submucosa, circularis muscularis, longitudinal muscularis, serosa and surroundings).

The numerical values for electrical properties of different layers of the tissue at 1 kHz were selected from (Kassanos et al., 2015), and electrical properties for the catheter tube and electrodes were selected from the Material Library provided in ANSYS Electronics. The electrical properties of the layers are presented in Table 3.1. Four different conductivity

Table 3.1: Electrical properties of different GI tract layers used in the FEM model.

	Electrical properties	
	Conductivity, σ (S/m)	**Relative Permittivity, ε_r**
Mucus	1.1	72
Mucosa	0.532	2.64×10^5
Submucosa	0.383	3.03×10^5
Circular muscularis	0.321	4.35×10^5
Longitudinal muscularis	0.5	1×10^6
Serosa	0.383	3.03×10^5
Surrounding tissue	0.148	1.97×10^5

luminal contents from 0.1 S/m to 1.44 S/m for conductivity (0.1 S/m for humid gas, 0.5 S/m for watery content, 1 S/m for loose stool and 1.44 S/m for semi-solid stool) and 1 to 80 for relative permittivity (1, 80, 80 and 80), respectively were used, to simulate content ranging from mixed of humid gas with mucus to liquid.

An excitation current of 10 µA was modelled between the outer electrodes, representing the maximum current that the bioimpedance measurement system can provide, and, for the calculations below, the voltage difference between the inner electrodes was measured.

Impedance sensitivity

The sensitivity distribution of the tetrapolar electrode system was also simulated within the lumen to define the region of measurement when lumen is empty and when a bolus is passing through. Sensitivity is defined as the contribution of a small volume to the total measured impedance. Hence the sensitivity and the total measured impedance is given as (Grimnes and Martinsen, 2007):

$$S = \frac{\vec{J}_1 \cdot \vec{J}_2}{I^2} \quad \text{and} \quad Z = \int_V \rho \cdot S \, dv \tag{3.1}$$

Where $\vec{J}_1$ is the current density vector when current I is injected between the outer electrodes, $\vec{J}_2$ is the current density vector when current I is injected between the inner electrodes, and ρ is the resistivity of the medium. Sensitivity can be positive, zero or negative depending on the dot product of the two vectors ($\vec{J}_1$ and $\vec{J}_2$). If the two vectors have an angle between them lower than 90 degrees, then S is positive, if the angle is bigger than 90 degrees it is negative, and if it is equal to 90 degrees then S is zero. A

positive S means that an increase in resistivity of the small volume will have an increment of the total measured impedance, whereas, a negative S means that an increment of the resistivity will decrease the total measured impedance. A zero S has no influence on the total measured impedance. The higher the absolute value of S, the greater the influence on the total measured impedance.

3.2.5 Statistical analysis

A set of 1500 samples of free flow through the gut – corresponding to approximately 5 minutes of recording data – were used for each content for the statistical analysis. Examination of the normality of data was tested by Shapiro-Wilks test. A non-parametric Wilcoxon test was used to compare mean difference between contents for impedance magnitude data phase angle at five different measuring frequencies (1 kHz, 5.6 kHz, 31.6 kHz, 177.18 kHz and 1 MHz). Correlation between the complete data sets of impedance magnitude and phase angle were compared against luminal diameter using Pearson's correlation coefficient (PCC). In all instances, p-values were less than *0.05* indicating statistical significance. Statistical analyses were carried out using SPSS Statistics, version 23 (IBM Corp., Armonk, NY, USA).

3.3 Results

3.3.1 Impedance sensitivity

Figure 3.4 shows the normalized sensitivity distribution of the catheter within the simulated lumen when it was empty and when bolus was passing through. In both distributions, negative sensitivities were found between the outer and inner electrodes, and positive sensitivity were found between inner electrodes. This accords with the simulated tetrapolar system model from Grimnes and Martinsen (2007). When the lumen is empty, positive sensitivity reaches to the mucosa and submucosa whereas when the bolus is passing through, the positive sensitivity region reaches about 2 mm (not getting to the mucosa in this case).

A larger volume of positive sensitivity can be seen in Figures 3.4(a) and 3.4(b), and this can be seen in both the experimental and simulated data since an increase in resistivity of luminal content corresponds to an increase in the total measured impedance baseline. When different conductivity boluses pass through there is an increment in total impedance for gas but a decrease for liquid (liquid equals to lower resistivity and gas equals to higher

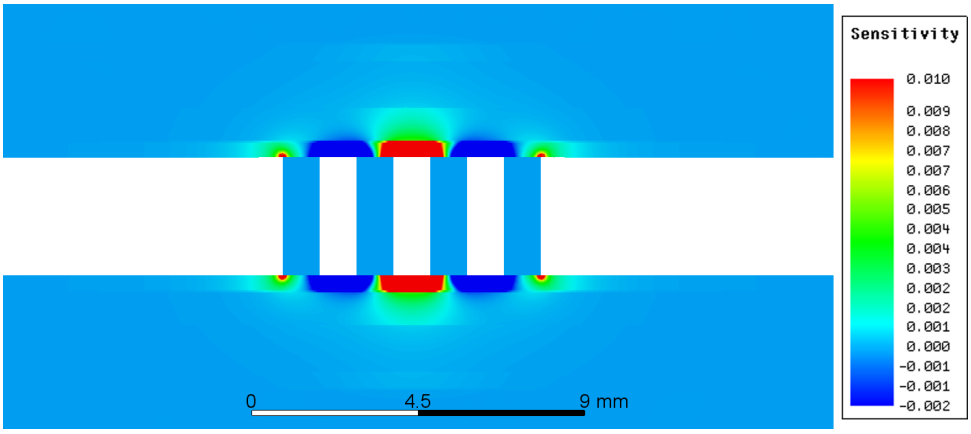

(a)

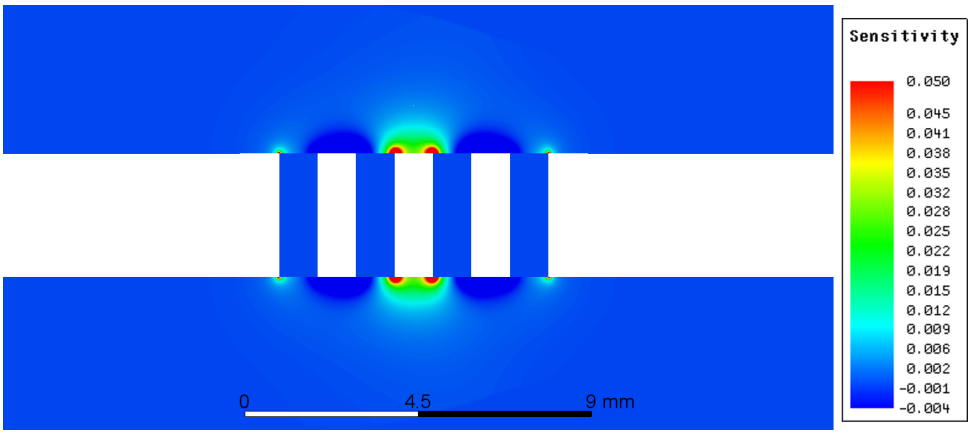

(b)

Figure 3.4: Normalised sensitivity distributions of the catheter in the simulated lumen when: (a) no bolus is present and (b) when a bolus is present.

resistivity). This can be explained due to the resistivity being higher when the lumen is in normal condition, due to the overall resistivity of content, mucus, mucosa and submucosa, and lower when the bolus passes through since the overall resistivity is due predominantly to the content.

3.3.2 Numerical and *ex-vivo* study

When the numerical model is in steady state, with a small but continuous flow of Krebs going through the lumen, small changes in luminal diameter do not cause much variation in baseline of the impedance magnitude measurement. Figure 3.5(a) shows the baseline of impedance magnitude of the continuous flow and then the passage of the bolus for different content conductivities in the simulation. The passage of the bolus travels from left to right as shown in Figure 3.3. The impedance magnitude baseline range (when there

is a continuous flow of Krebs) goes from 48.80 Ω for higher conductive content (liquid) to 63.80 Ω for lower conductive content (moist air or gas), respectively. Similarly, the experimental data of both bolus types (liquid and gas) are shown in the Figure 3.5(b). The baseline impedance magnitude, for continuous flow of Krebs and gas, is 34.95 Ω and 45.00 Ω respectively.

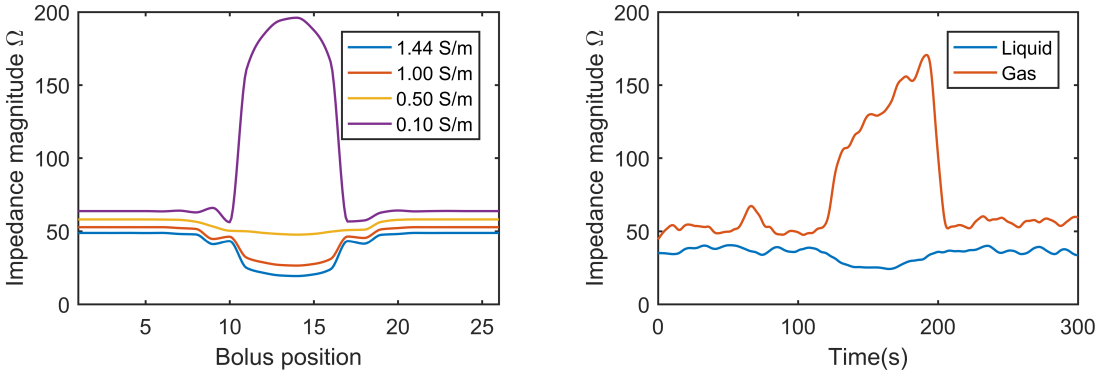

(a) (b)

Figure 3.5: Variation in impedance magnitude measured at 1 kHz for (a) a numerical simulation of four different luminal contents ranging from gas (0.1 S/m) to liquid (1.44 S/m); and (b) measured data of the passage of liquid and gas bolus in the excised section of guinea pig colon.

3.3.3 Impedance spectroscopy

Table 3.2 shows the specific (median, interquartile range (IQR), mean and standard deviation) and the summary statistics for the difference between impedance magnitude and phase angle between content at each measuring frequency. There were significant differences between content for mean impedance magnitude and phase angle the only exception to this being for impedance magnitude at 1 MHz.

The mean impedance magnitude for liquid content (34.9, 30.5, 28.8, 25.5 and 18.1 Ω at different frequencies from 1 kHz to 1 MHz) were lower than for gas content (48.4, 40.9, 37.2, 30.3 and 18.3 Ω). The Wilcoxon matched-pairs test showed that the difference between the means over the frequency range 1 kHz to 177.81 kHz for impedance magnitude (13.5, 10.4, 8.4 and 4.8 Ω respectively) were significant beyond *0.001* level: asymptotic $p < 0.001$ (two-tailed). The matched-pairs rank biseral correlation are 0.98, 0.98, 0.98 and 0.9, respectively (representing 'large' effects). No significant difference of means in impedance magnitude at 1 MHz between contents was evident (asymptotic $p = 0.485$).

Table 3.2: Mean, median, IQR and standard deviation of impedance magnitude and phase angle for liquid and gas bolus.

		Liquid				Gas						
	Frequency	**Median**	**IQR**	**Mean**	**Std**	**Median**	**IQR**	**Mean**	**Std**	**Mean difference**	**p-value**	**Effect size (r)**
Impedance Magnitude	**1 kHz**	34.3	5.0	34.9	3.6	44.9	12.5	48.4	10.1	-13.6	<0.001	0.98
	5.6 kHz	30.2	3.9	30.5	2.8	38.3	8.8	40.9	7.3	-10.3	<0.001	0.98
	31.6 kHz	28.6	3.4	28.8	2.4	35.0	7.3	37.2	6.1	-8.4	<0.001	0.98
	177.8 kHz	25.3	2.6	25.5	1.9	28.7	5.4	30.3	4.6	-4.8	<0.001	0.90
	1 MHz	17.7	1.5	18.1	1.8	17.2	3.7	18.3	3.1	-0.3	0.485	0.02
Phase angle	**1 kHz**	-11.4	1.6	-11.5	1.1	-11.9	2.0	-12.1	1.6	0.6	<0.001	0.26
	5.6 kHz	-4.9	0.7	-5.0	0.5	-6.6	1.5	-6.8	1.0	1.8	<0.001	0.98
	31.6 kHz	-5.4	1.2	-5.4	0.8	-8.3	1.3	-8.3	0.9	2.9	<0.001	1.00
	177.8 kHz	-11.0	2.0	-11.2	1.4	-16.8	1.2	-16.8	0.9	5.6	<0.001	1.00
	1 MHz	-19.5	3.3	-19.8	3.3	-24.5	2.3	-24.5	2.7	4.7	<0.001	0.89

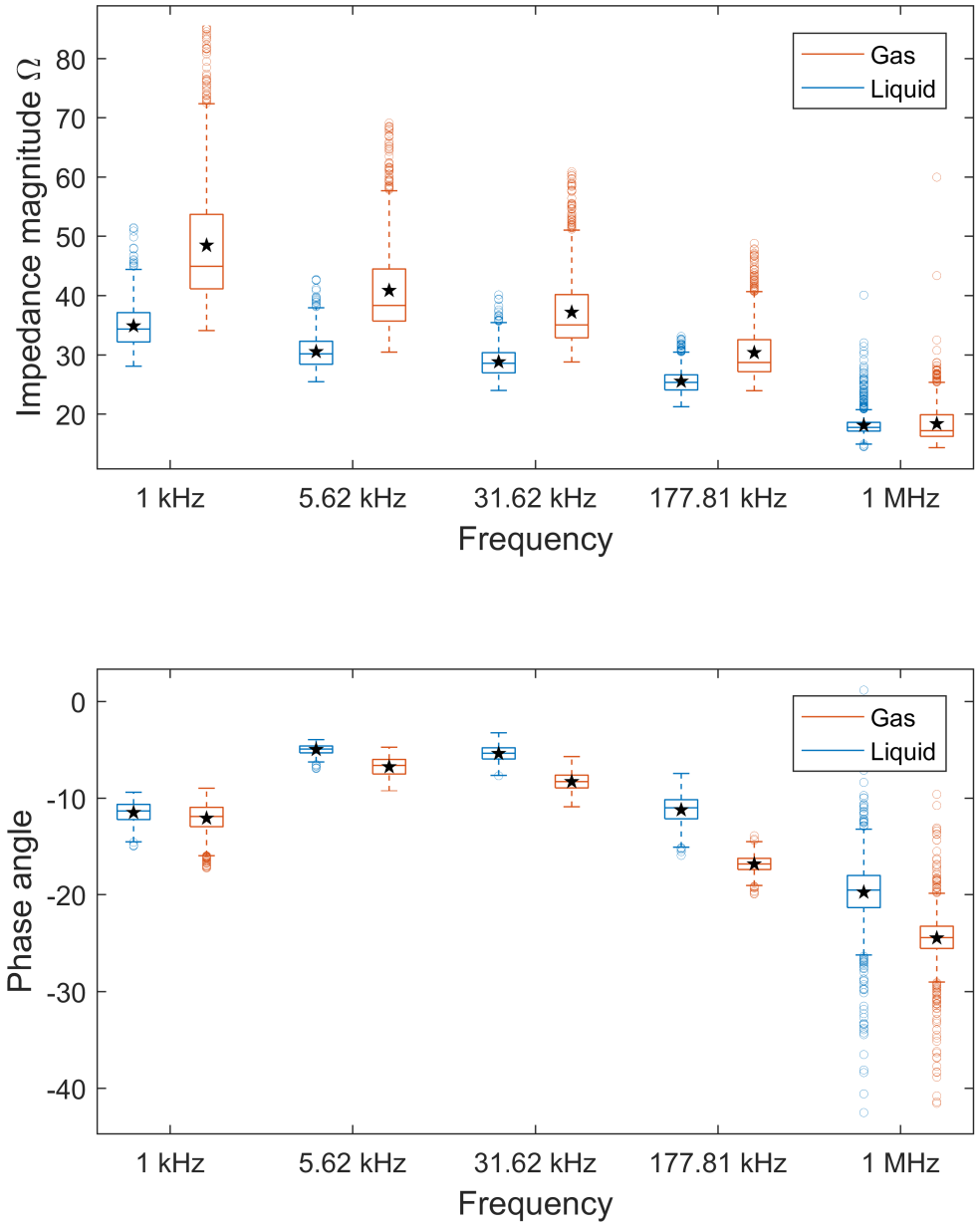

Figure 3.6: Box plots of impedance magnitude (top) and phase angle (bottom) for different content at different measuring frequencies. Star points represent the mean of the data set.

Similarly, the mean phase angles for liquid content (-11.5, -5, -5.4, -11.2 and -19.8° degree at different frequencies from 1 kHz to 1 MHz) were lower than for gas content (-12.1, -6.8, -8.3, -16.8 and -24.5° degree). The Wilcoxon matched-pairs test showed that the difference between means of contents at frequency range 1 kHz to 1 MHz for phase angles (0.6, 1.8, 2.9, 5.6 and 4.7 ° degree respectively) were significant beyond *0.001* level: asymptotic

$p < 0.001$ (two-tailed). The matched-pairs rank biseral correlation are 0.26, 0.98, 1.00, 1.00 and 0.89, with r values between 0.1 and 0.3 indicating a 'small' effect, and above 0.5 indicating a 'large' effect.

The difference between median and mean is small for liquid whereas for gas that difference is bigger at lower frequencies and lower at bigger frequencies, Table 3.2. Furthermore, for impedance magnitude measurements, no overlap in IQR was observed between contents over the frequency range (1 kHz – 177.81 kHz), however, some overlap was seen at 1 MHz, Figure 3.6. Standard deviation and IQR for impedance magnitude are smaller for liquid than for gas content.

For phase angle, no difference between median and mean was observed for liquid and gas content, Table 3.2. Conversely, the phase angle measurements did not overlap in the IQR between contents at higher frequencies (5.62 kHz – 1 MHz, Figure 3.6), but did at the lowest frequency. Further, no difference between IQR and standard deviation for liquid and gas content were observed. In both instances, for impedance magnitude and phase angle measurements, outliers are present. The causes of these outliers are explained in the discussion section.

3.3.4 Impedance spectroscopy and DMaps

Table 3.3 shows the correlations and 95% confidence intervals between the impedance magnitude and phase angle against the measured diameter with for the two extreme types of content. All Pearson correlations were significant beyond *0.001* level ($p\text{-value} < 0.001$). The impedance magnitude is negatively correlated for liquid (coefficient range: -0.78 – -0.12 being the highest at 5.62 kHz), whereas for gas the correlation is positive (coefficient range: 0.47 – 0.39). Conversely, the phase angle correlation for liquid is positive (coefficient range: 0.87 – 0.58 being the highest at 177.81 kHz) and for gas is negative (coefficient range: -0.48 – -0.04), see Figures C.1 and C.2. Liquid content gives better correlation coefficients than gas content. The correlation coefficients were stronger for phase angle than impedance magnitude.

3.4 Discussion

This present study has demonstrated, for the first time, that complex impedance spectroscopy may be useful to differentiate between liquid and gas media inside the colon. Differences between mean values between intra-luminal content were found significant (Table

Table 3.3: Pearson correlation and 95% confidence intervals for magnitude and phase angle of liquid and gas against diameter of the specimen. All p values for each correlation were found significant, *p-value* < 0.001.

		1 kHz		**5.6 kHz**		**31.6 kHz**		**177.8 kHz**		**1 MHz**	
Liquid	Magnitude	-0.77	-0.78 -0.76	-0.78	-0.79 -0.77	-0.75	-0.76 -0.74	-0.66	-0.67 -0.65	-0.12	-0.13 -0.11
	Phase	0.83	0.83 0.82	0.82	0.82 0.81	0.74	0.75 0.73	0.87	0.87 0.87	0.55	0.56 0.54
Gas	Magnitude	0.47	0.48 0.46	0.46	0.47 0.47	0.45	0.46 0.44	0.44	0.45 0.43	0.38	0.39 0.37
	Phase	-0.41	-0.42 -0.40	-0.48	-0.49 -0.47	-0.33	-0.34 -0.32	-0.17	-0.18 -0.16	-0.04	-0.05 -0.03

3.2). For example, the difference between the impedance magnitude of contents is larger at low frequency (1 kHz) and decreases at higher frequencies (up to 177.81 kHz). Contrarily, the difference between phase angles of contents is larger at the highest frequency (1 MHz) and decreases at lower frequencies (to 5.6 kHz).

In addition, the IQR and standard deviation for impedance magnitude of liquid are at least two times smaller than for gas content. This makes sense as the conductivity of the mixed gas varies more than the conductivity of liquid that is constantly flowing through the specimen. Three reasons could explain this: a) when gas is passing through the specimen, this is mixed with moisture and mucus but these are not homogeneously distributed and b) the catheter may touch the walls due to gravity, affecting the measurement as well, c) similarly, a few small bubbles were seen in the liquid bolus, which could alter the impedance readings, however, this effect was less than was seen with gas content. This could also be the reason for the outliers in the graphs.

The difference in impedance magnitude at different measuring frequencies shows that dielectric materials are involved in the measurements during bolus transit studies. As the content medium (Krebs) is purely electrolytic, this behaviour can only come from the luminal wall. This decrease in impedance, when the frequency increases, is also seen in a study in pigs for monitoring ischemic injury in the gastric mucosa performed by Gonzalez et al. (2003).

The correlation between impedance magnitude and diameter partially agrees with previous values calculated by Costa et al. (2013), however we cannot directly compare these data

due to the unknown measuring frequency used by their system, the differences in the geometry of electrodes, and the two element configuration used, compared to the 4 element configuration used in this work. A strong correlation between changes in phase angle and external diameter was shown in our studies.

The numerical model allowed us to further understand the bolus passage with different conductivity content. The numerical data were compared with the two big boluses created by clamping the end (liquid and gas bolus diameter were approximately 6 mm and 7.5 mm respectively). Bolus media with high conductivity (1 S/m and 1.44 S/m) had the same trend (a decrease in impedance magnitude) as the liquid bolus from experimental data. Similarly, bolus mediums with low conductivity (0.1 S/m) had the same trend (an increase in impedance magnitude) as the gas bolus from the experimental data, these trends are the same as those shown by Tutuian and Castell (2005). The total change in both instances are lower in the experimental data but as mentioned before the diameter of the bolus did not reach the 10 mm used in the simulation. Furthermore, the shape of the bolus in the simulation stays constant unlike in the experimental data in which the bolus shapes could vary with the spontaneous propagating contractions.

The impedance magnitude baseline from the numerical data (1.44 S/m had 48 Ω and 0.1 S/m had 61 Ω) were slightly higher than the mean from the experimental data at 1 kHz (mean impedance magnitude for liquid and gas were 34 Ω and 51 Ω, respectively). That could be explained by the temperature effect on conductivity which was not included in the simulations. Temperature increases conductivity of materials. For example, the conductivity of 0.9% NaCl at 25℃ is 1.44 S/m but at 37℃, temperature at which the experiments were carried out, is 2 S/m (Grimnes and Martinsen, 2008).

When a high conductivity bolus passes the impedance sensor, the impedance magnitude drops, while for low conductive bolus, the impedance magnitude goes up. The closer the conductivity of the medium gets to the conductivities of the luminal wall the less change occurs. The sensitivity of the overall impedance sensor is therefore related to the conductivity of the content, the higher the conductivity of the content, the higher the sensitivity of the sensor. Hence, where possible it is advisable to use a bolus with the greatest contrast to that of the luminal wall. This is of direct interest to studies where a controlled bolus can be used, except that any bolus used in the oesophagus must also be palatable to the subject.

With regard to this study, some limitations need to be considered. Firstly, only one specimen was used for this preliminary study; however, the strong agreement with our FEM simulation gives us confidence in our results. Secondly, the lack of information on

electrical and mechanical properties of faecal content made it impossible to generate a suitable analogue material for semi-solid faeces, hence only two contents (liquid and gas) were used in this preliminary study. And lastly, the minimum measuring frequency was limited to 1 kHz as using measuring frequencies below this would affect the overall sample frequency.

To conclude, we observed that the impedance measurements recorded during the passage of a liquid or gas bolus are frequency dependent due to the electrical properties of the luminal wall. Given the differences observed in complex impedance spectroscopy between liquid and gas, a good frequency range is 5.62 kHz to 177.81 kHz, depending on what parameter (impedance magnitude or phase angle) is used for the analysis. Frequencies closer to 5.62 kHz are recommended for impedance magnitude, closer to 177.81 kHz are recommended for phase angle and/or a median frequency around 100 kHz if both parameters are to be taken into account. Lastly, increasing the conductivity of the bolus content with respect to the conductivity of the mucosa will increase the sensitivity of the impedance sensor.

Chapter 4

Development of a High Resolution Impedance Manometry catheter

The study presented in this chapter is the subject of the following refereed conference paper:

Ruiz-Vargas, A, Costa, M, Wiklendt, L, Dinning, PG, Arkwright, JW. The use of fibre optic sensing technology with intraluminal impedance catheter for functional gastrointestinal motility disorders. In: *Australian and New Zealand Conference on Optics and Photonics 2015 (ANZCOP 2015)*. Engineers Australia, 2015: 51-54. Podium presentation

4.1 Introduction

As seen in **Chapter 2**, High-Resolution-Impedance-Manometry (HRIM) catheters are one of the primarily tools in the diagnosis of swallowing disorders (Kahrilas and Sifrim, 2008; Tutuian, Vela, Balaji, Wise, Murray, Peters, Shay and Castell, 2003). This tool combines two components; 1) the manometry component consisting of an array of sensors that records the intraluminal pressure and contact force associated with gut contractions, and 2) the impedance component that records resistance to alternating currents measured between multiple electrode pairs. Impedance within the gut can be used to record the transit of content (the electrical resistance changes as content moves over the electrode pairs), and can also provide a measure of the cross-sectional area of the lumen (Zifan et al., 2015).

In the human oesophagus, specific metrics, based upon pressure (manometry) and bolus flow (impedance) have been developed to help assess the aspiration risk in patients with swallowing disorders (Omari et al., 2011). Nevertheless, the use of HRIM catheters for assessment of small bowel, colonic motility and bolus transit is not yet established. Although, a set of studies have been performed with HRIM catheters on isolated segments of colon from rabbits (Costa et al., 2013; Mohd Rosli et al., 2018), and examining the relationships that exist between the changes in diameter (measured as internal cross-sectional area by impedance and with video recording of the external diameter) and change in pressure (Costa et al., 2013).

A typical commercially available HRIM catheter has 32 pressure sensors (spaced 10 mm apart) and 16 impedance sensors (spaced 20 mm apart). The large number of wires required – 128 and 17 wires for pressure and impedance sensors, respectively – to monitor both impedance and pressure increases the catheter diameter and limits the impedance sensor spacing to 20 mm intervals. Therefore, an impedance value can only be attributed to every second pressure sensor, which *in-vitro* studies of animal models can be an inconvenient, as sections of animal models are smaller than their human counterparts. There is a need to have closer spaced electrodes (**Aim 3**) to understand how the gut works in smaller models in order to know more about the human gut.

Previously our group have developed a fibre-optic manometry catheter based upon Fibre Bragg Gratings (FBG) (Arkwright, Underhill, Maunder, Blenman, Szczesniak, Wiklendt, Cook, Lubowski and Dinning, 2009). These manometry catheters have shown to be a viable clinical tool for recording gut contractions over long sections of the GI tract (Arkwright, Blenman, Underhill, Maunder, Szczesniak, Dinning and Cook, 2009; Dinning et al., 2014). Each fibre within these catheters can contain up to 36 sensors spaced at 10 mm

intervals and as each catheter can have 4 separate fibres a total of 144 sensors can be included while still maintaining a high degree of flexibility and an external diameter of just 3 mm (Arkwright, Underhill, Maunder, Blenman, Szczesniak, Wiklendt, Cook, Lubowski and Dinning, 2009).

In this chapter, the evolution of this catheter is introduced. The additional space inside the catheter provided by the fibre optic manometry sensors allowed us to space the impedance sensors at 10 mm intervals in a catheter that is still less than 3 mm in diameter for use in *in-vitro* animal models. Finally, the catheter was tested in an excised section of guinea pig colon.

4.2 Methods

4.2.1 Catheter design

The fibre optic pressure sensors were formed from a pair of helically wound Draw Tower Grating (Lindner et al., 2011) arrays each with fibre Bragg grating (FBG) elements space 10 mm apart and with Bragg wavelengths spaced at 2 nm intervals over the range 1510 nm to 1590 nm. The winding was controlled so that the FBGs in each fibre at each sensing location were oriented one above the other and either side of the FBG was bonded to a rigid substrate using thermally cured epoxy (EPO-TEK 353 ND-T, Epoxy Technology, Billerica, MA, USA), so that the applied pressure increased the strain in the lower FBG and decreased it the upper FBG, as shown in Figure 4.1. This removes the characteristic temperature sensitivity commonly seen with FBG sensors because the applied force results in a differential change in wavelength whereas a change in temperature causes a common mode change (Wang et al., 2012). The rigid substrates were 3D printed in stainless steel using the design shown in Figure 4.1.

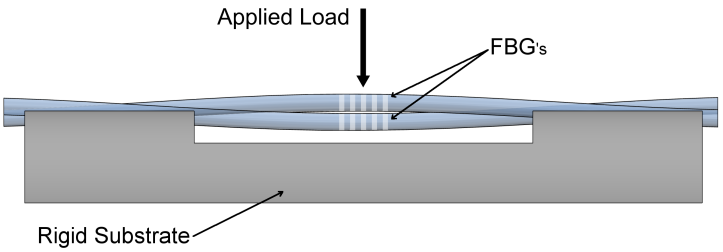

Figure 4.1: Pressure sensor formed by a pair of fibres containing FBGs arrays bonded into the stainless-steel substrate. The FBGs are allocated in the middle of the window and one above the other.

The catheter was assembled in a dual lumen silicone extrusion of 2.8 mm outer diameter, 2.4 mm inner diameter and containing two semi-circular lumina, see Figure 4.2. The fibre optic sensing array contained 35 pressure sensing regions spaced at 10 mm intervals; fibres usually contain 36 gratings but one of the gratings was removed during the assembly process to facilitate termination of the distal section of the catheter. The fibre optic sensing array is contained in the upper lumen of the extrusion and the other lumen contains the wires to connect the electrodes with the data acquisition system, see Figure 4.2. Sixteen impedance electrodes were also spaced at 10 mm intervals and were located at one end of substrates containing the pressure sensing elements, see Figure 4.3. The optical fibres were connectorised with E-2000 connectors (Huber+Suhner, Sydney, NSW, Australia) and wires from impedance sensors were connected to a 27 PIN ODU connector (ODU MINISNAP PC PANEL SOCKET O-G13C1GP27QF000000, ODU GMBH & CO. KG, M, Mühldorf a. Inn, Germany) and were compatible with the connectors on a Sandhill impedance manometry system (InSight, Sandhill Scientific Inc., Highlands Ranch, CO, USA).

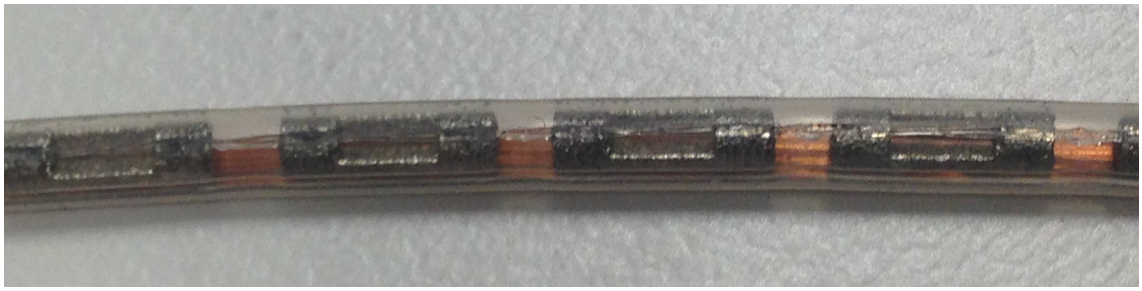

Figure 4.2: Pressure sensor array (top lumen) and electrical wires (bottom lumen) assembled in the dual lumen silicone tube prior to the addition of the external impedance electrodes.

To form the electrodes, the wires are pulled through the outer skin of the second lumen and wrapped around the catheter. The wires are then bonded in place with conductive silver epoxy (EPO-TEK H20E, Epoxy Technology, Billerica, MA, USA), see Figure 4.3.

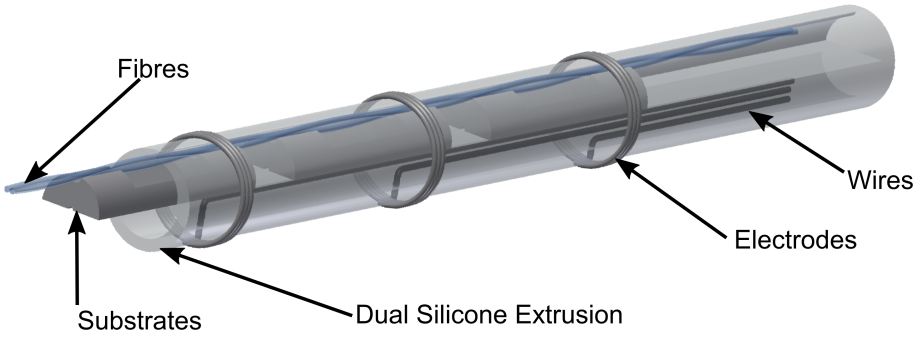

(a)

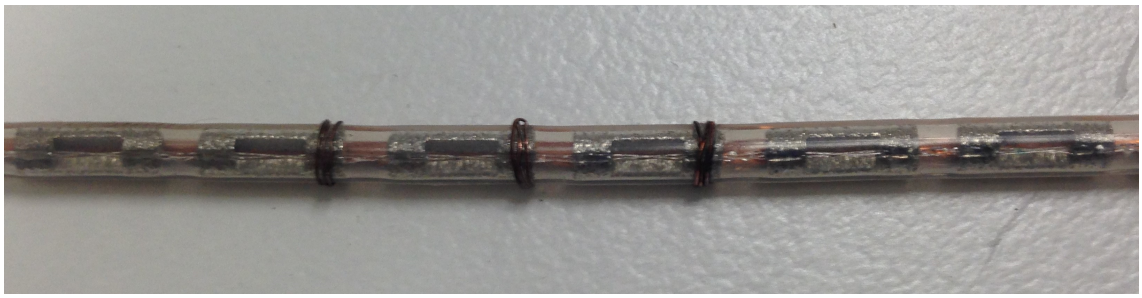

(b)

(c)

Figure 4.3: (a) Schematic of a section of the impedance manometry catheter showing the location of optical fibre sensors, electrical wires, electrodes and dual lumen extrusion. (b) Catheter assembled with electrical wires wrapped around the lumen. (c) Silver electrodes formed by silver-conductive epoxy.

4.2.2 Equipment

Three different data sets were used in the experiments; impedance, pressure, and diameter of the segments. This allowed us to directly correlate contractile activity measured using the optical pressure sensors with the luminal cross-section measured using impedance. The luminal diameter was confirmed using direct video imaging of the preparation.

A digital video camera (Canon Legria HF S20. Ota, Tokyo, Japan), positioned above the preparation was used to record video images to create spatiotemporal maps of changes in

diameter, referred to as 'DMaps' (Hennig et al., 1999).

Intraluminal impedance data were recorded with an Insight system by Bioview impedance manometry software (Sandhill Scientific Inc, Highlands Ranch, CO, USA), connected to the electrodes to record the impedance of the two consecutive pairs of electrodes along the catheter. Data was acquired at a rate of 50 samples per second. The measuring frequency at which impedance is calculated from the system is unknown and has not been reported in any datasheet or manual. Although, Ates et al. (2015) reported a measuring frequency of 2 kHz on his studies for measuring oesophageal mucosal impedance.

A spectral interrogator unit (FBGS FBG-scan 804; FBGS International, Geel, Belgium) with an optical bandwidth of 1510 nm to 1590 nm was used to monitor the manometry sensors. The two fibres were connected to channels 1 and 2 on the interrogator. Custom-software based on NI LabVIEW platform (version 2015 sp1, National Instruments, Austin, Texas, USA) was developed to acquire data from the interrogator unit and to correct data due to the intrinsic errors of spectrometers based on CCD arrays (Parkinson et al., 2018). The interrogator system recorded the pressure profile along all the 35 sensors simultaneously, at a sample rate of 10 Hz, to create spatiotemporal maps of changes in pressure, referred to as 'PMaps' (Costa et al., 2013).

During the experiments, time stamps and an LED indicator at the edge of the bath were recorded simultaneously in all recordings in order to synchronise impedance, pressure and the video.

4.2.3 Calibration

The data measured from the optical interrogator system is given in wavelength (in units of nm). To provide clinically applicable data, the changes in wavelength need to be converted into pressure. In order to calibrate the pressure sensors, the catheter was put in a calibration tube sealed and pressurized to 100 mmHg. The calibration constants for each channel were then calculated by dividing the increase in pressure by the shift in wavelength. This calibration process calibrates all the sensors at once. Note that in gastrointestinal studies, impedance sensors are typically not calibrated, and output data are given in ohms. However, for our studies, the catheter was immersed in a 0.9% NaCl solution to calculate the cell constant prior to use in the organ bath.

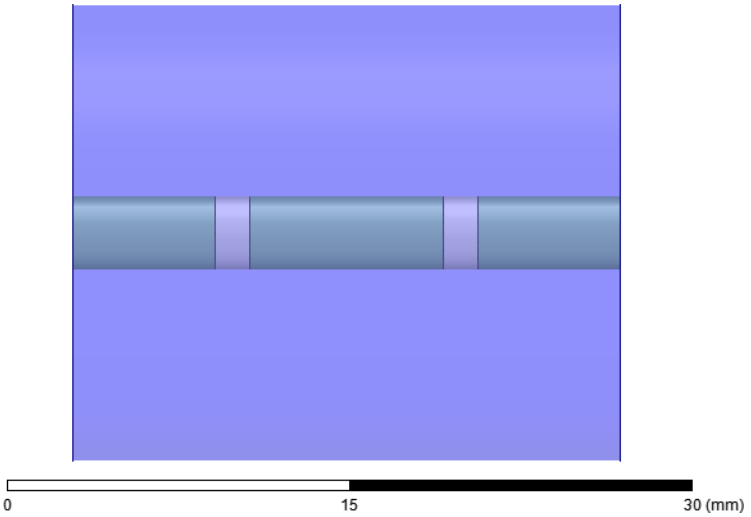

Figure 4.4: Lateral view of the 3D model to simulate the distributed sensitivity of the electrode configuration.

Impedance sensitivity

The sensitivity distribution of the bipolar electrode system used on the catheter was simulated in ANSYS Electronics. Figure 4.4 depicts the model used to simulate the sensitivity distribution of the catheter electrodes (bipolar system). The 3D model consists of a catheter with 2 ring electrodes of 2 mm length and 3 mm outer diameter, which is surrounded by a cylinder (20 mm outer diameter) of 0.9% NaCl, see Figure 4.4.

Analogously to the approach taken in **Chapter 3**, the sensitivity and the total measured impedance for a two-electrode system is the same as given for a four-electrode system (Equation 3.1):

$$S = \frac{\vec{J}_1 \cdot \vec{J}_2}{I^2} \quad \text{and} \quad Z = \int_V \rho \cdot S \, dv \tag{4.1}$$

Where $\vec{J}_1$ is the current density vector when current I is injected between the outer electrodes, $\vec{J}_2$ is the current density vector when current I is injected between the inner electrodes (for bipolar systems $\vec{J}_2 = \vec{J}_1$), and ρ is the resistivity of the medium. The simulated sensitivity presented in **Chapter 3** was positive, zero or negative depending on the dot product of the current density vectors; however, in this instance (two-electrode system), negative sensitivity never occurs as $\vec{J}_1$ and $\vec{J}_2$ are the same. $S > 0$ means that an increase in resistivity of the small volume will increase the total measured impedance, whereas, an S of zero will have no influence on the total measured impedance. The higher the value of S, the greater the influence on the total measured impedance.

4.2.4 *Ex-vivo* experiment

The impedance manometry catheter was tested in an excised section the proximal colon of a guinea-pig. A section of the gut was removed from the laboratory animals by methods approved by the Animal Welfare Committee of Flinders University. The removed section of colon was placed into a beaker containing oxygenated Krebs solution (in mM: $NaCl$, 118; KCl, 4.7; NaH_2PO_4, 1.0; $NaHCO_3$, 25; $MgCl_2$, 1.2; *D- Glucose*, 11; $CaCl_2$, 2.5) and bubbled with 95% O_2/ 5% CO_2. The faecal pellets were gently flushed out of the colonic segment with Krebs solution.

The excised section of gut was then placed into an organ bath containing the same Krebs solution warmed to 36-37℃. The Krebs solution keeps the gut alive for many hours allowing both spontaneous and stimulated muscular activity to occur.

In the organ bath, the anal and oral ends of the proximal colon were attached to T-shaped plastic connectors (Figure 4.5). The catheter was passed through the oral end connector and the vertical arm of the oral T-piece was connected to an infusion pump. Warm (36 - 37℃) Krebs solution was infused through the infusion pump at different rates (2 to 3 mL/min) in order to stimulate contractile activity.

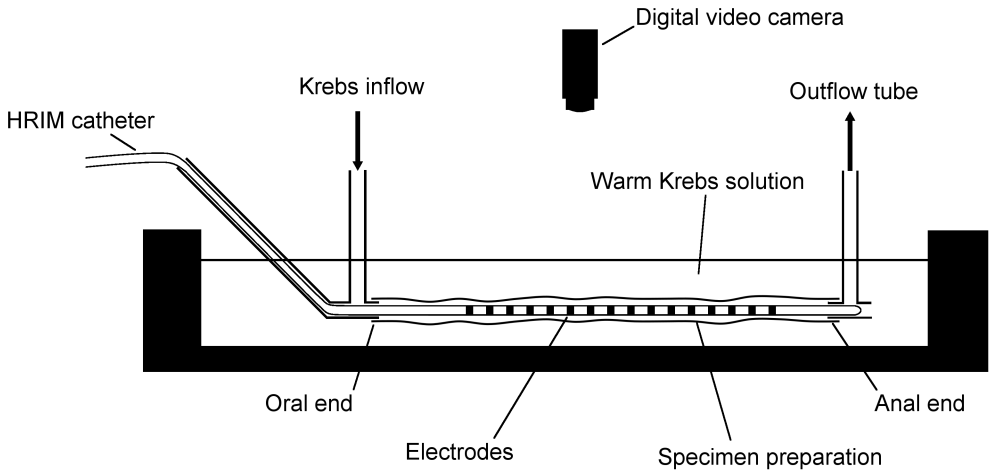

Figure 4.5: Experimental set-up used to carry out the experiments with the custom HRIM catheter.

4.2.5 Construction of diameter maps (DMaps) and pressure maps (PMaps)

The videos were re-sampled down to ten frames per second in Quicktime (Apple, Cupertino, California, USA). Each video was then converted into spatiotemporal maps of

changes in diameter (DMaps) using a custom-written software in Matlab (MathWorks, Natick, MA, USA) (Costa et al., 2013). Based upon the method developed by Hennig et al. (1999), the diameter at each point along the length of the colon was calculated for each frame and converted into grayscale pixels. Regions of minimal diameter (contraction) were represented on maps as white pixels, whereas regions of maximal diameter (distension) were represented by black pixels. The DMaps presented here represent the section of colon located between the inner extremities of the T-shaped connectors.

The recorded manometric and impedance traces were viewed and analysed using software (PlotHRM). The software was written in Matlab (The MathWorks, MA, USA) and Java (Sun Microsystems, CA, USA). The line traces of pressure were converted to spatiotemporal pressure maps (PMaps) using this software.

4.3 Results and discussion

The pressure calibration constants are shown in Figure 4.6. The average and standard deviation sensitivity of the sensors was 1.44 ± 0.18 mmHg/pm. The average and standard deviation of the cell constant of the impedance sensors was 287.34 ± 35.86 m^{-1}. This was compared with the simulated cell constant of similar configuration and electrode size. The simulated cell constant was 117.41 m^{-1} which differs considerably compared to the experimental cell constant. This could be explained as the simulated uses smooth metal ring electrodes whereas the actual electrodes were made of conductive silver epoxy formed roughly around the wires, and the fact that the electrode length for the simulation may not be the same as the one formed with epoxy.

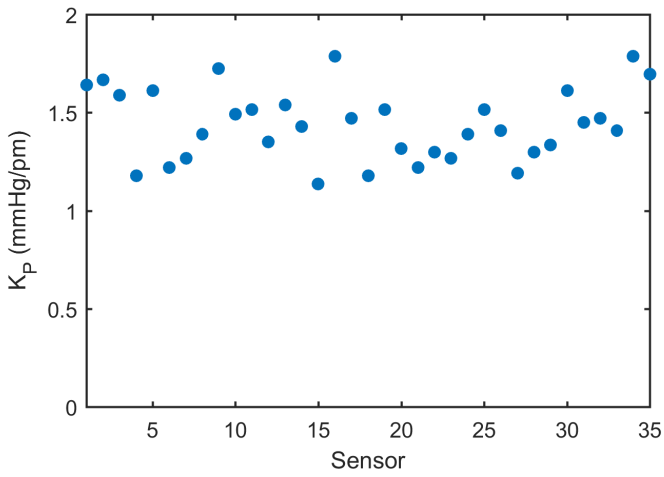

Figure 4.6: Pressure constants for the pressure sensor array of the 35 pressure sensors.

The pressure constants were seen to vary slowly over time (days). This variation could be due to the inherent nature of the silicone and manipulation of the catheter. Therefore, a pressure calibration was carried out before each experiment.

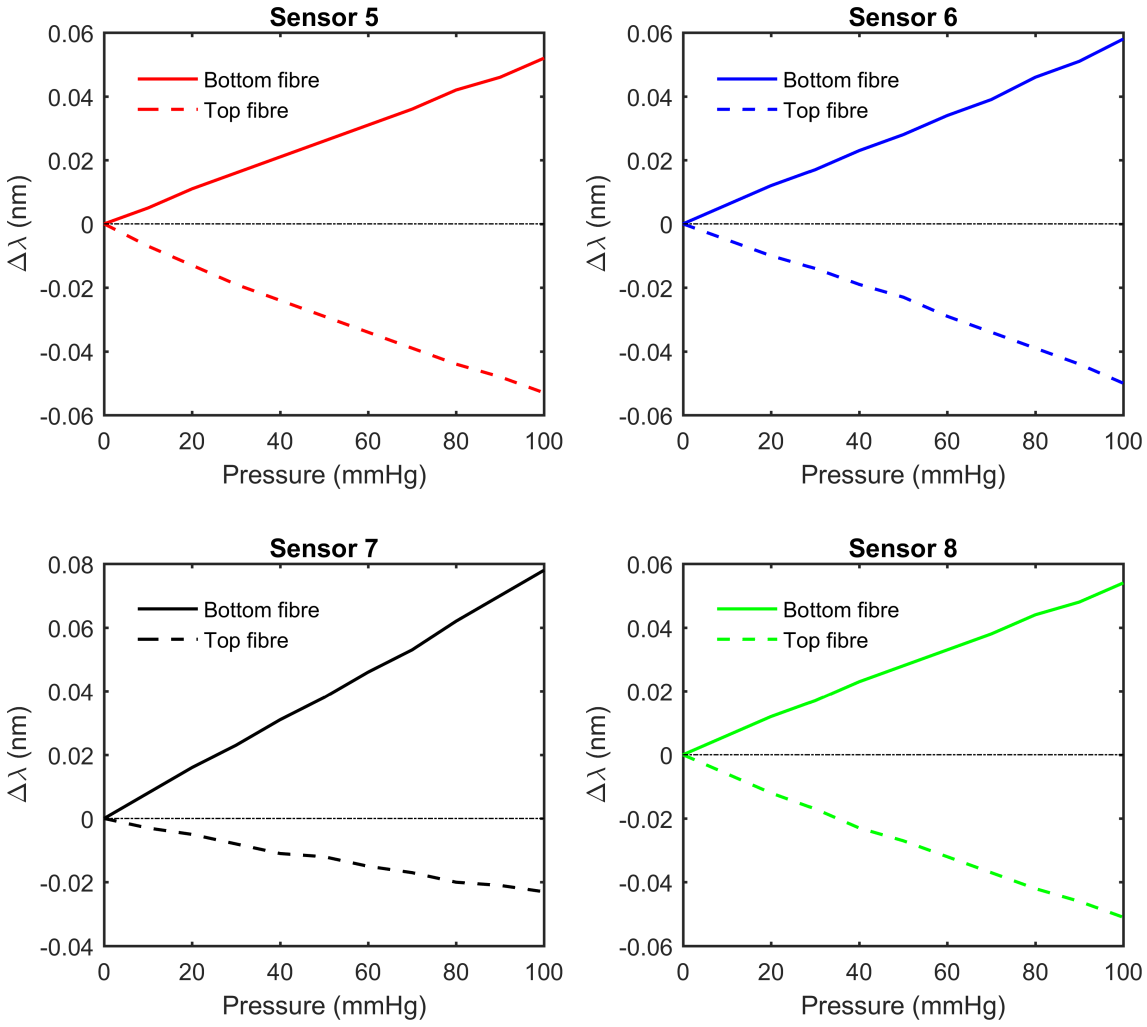

Figure 4.7: Wavelength shift of bottom and top fibres for sensors 5 to 8 along the pressure range 0 to 100 mmHg.

After calibrating the device, the same set up was used to investigate the linearity and symmetry of the pressure sensors by applying pressure increments of 10 mmHg up to 100 mmHg. Figure 4.7 shows the wavelength shift seen on the top and bottom fibres during the pressure increments for sensors 5, 6, 7 and 8. Sensor 5 presents a perfect symmetry which means the grating from top fibre is placed right above the other; sensors 6 and 8 have almost a perfect symmetry, whereas sensor 7 presents a bad symmetry. This means that either the grating in the top fibre is not placed above the other or that the double helix is not symmetric around a common linear axis. However, neither will adversely affect the sensitivity of the device since taking the difference from bottom and top fibres,

the difference should be approximately similar as seen in Figure 4.7 (0.105 nm, 0.108 nm, 0.101 nm and 0.105 nm from sensor 5 to sensor 8 at 100 mmHg).

Finally, Figure 4.8 shows the performance of the algorithm to correct the errors from the spectrometer. Both graphs show the average, maximum and minimal readings of the 35 sensors. Typical error without correction is about ± 10 mmHg at a pressure of 100 mmHg. Using the custom-made software with the compensation method, the error was reduced by a factor of five, resulting in a maximum error of 2%.

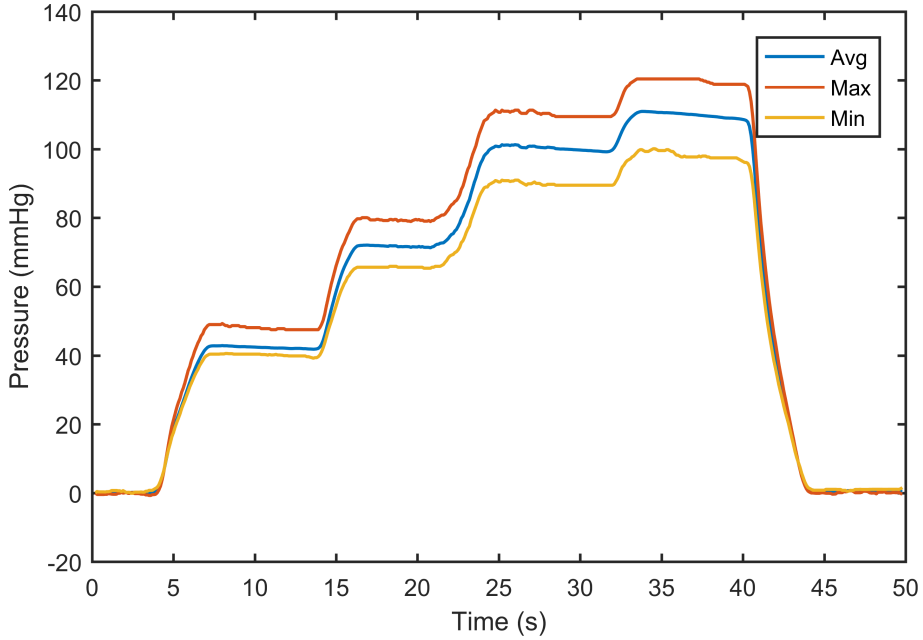

(a)

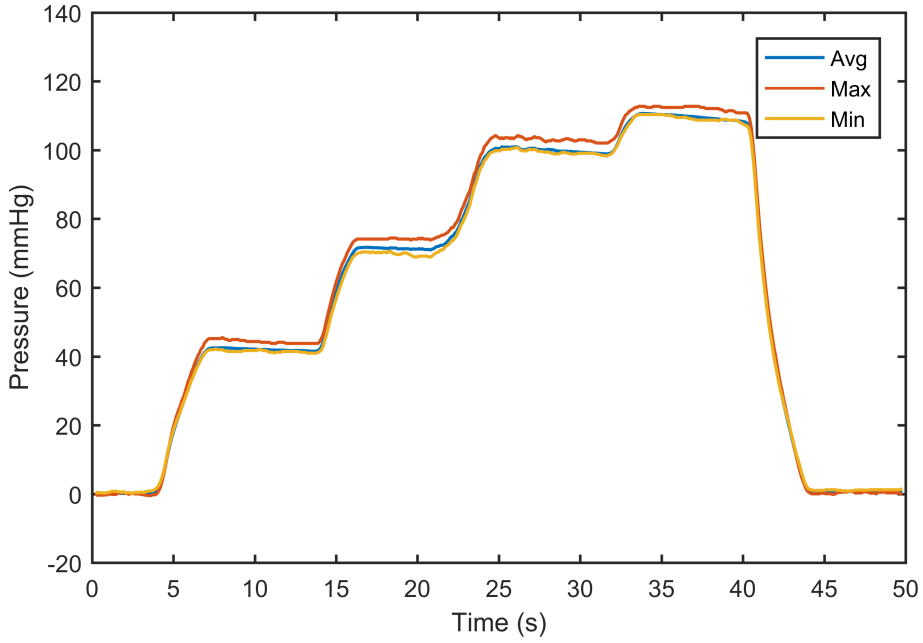

(b)

Figure 4.8: No compensated (a) and compensated (b) data from a recording after calibration.

Impedance sensitivity

Figure 4.9 shows the results from the simulated sensitivity of the catheter configuration. The sensitivity values were normalised; values near to 1 have the highest influence on the total measure impedance, and values near to 0 have very little influence.

The simulated sensitivity in the model shows how the volumes closest to the electrodes have the most influence on the total measured impedance. On the other hand, volumes closer to the mid-point between electrodes have much less influence. A more detailed analysis on distributed sensitivity of the catheter built in this chapter and a commercial High-Resolution-Impedance-Manometry (HRIM) catheter is performed in **Chapter 5**.

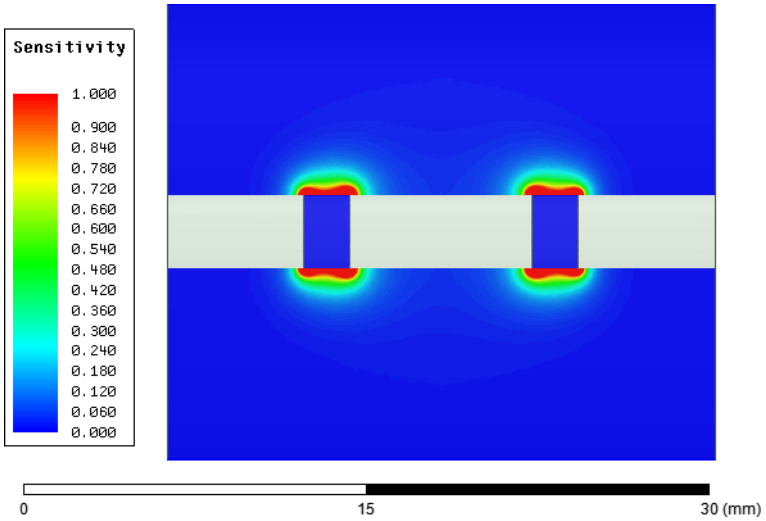

Figure 4.9: Lateral cross-section of the 3D model showing the normalized distributed sensitivity of the electrode configuration. Colours represent the sensitivity of the simulated model; red regions indicate highest influence whereas blue regions indicate none influence on the total measured impedance.

4.3.1 *Ex-vivo* experiment

Data collected from the experiment were processed and plotted in both PMap and DMap formats with the impedance signals shown as line plots in Figures 4.10 (a) and (b). In the PMap shown in Figure 4.10(a), the colours represent changes in pressure ranging from 0 to 60 mmHg. In the DMap shown in Figure 4.10(b), the greyscale represents diameters ranging from 4 to 11 mm. The impedance measurements are only qualitative and are displayed in arbitrary units since the electrical conductivity of the Krebs solution was not quantified during this experiment.

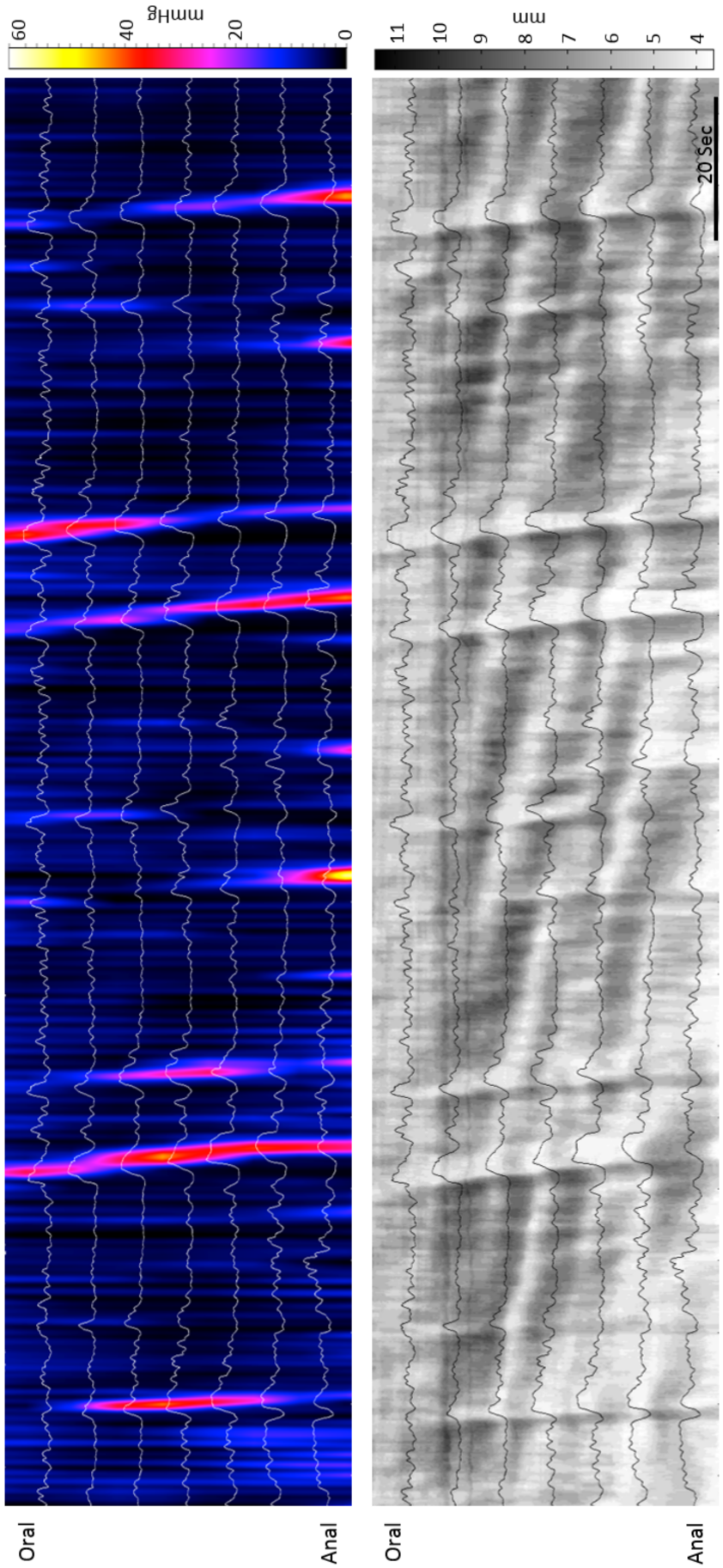

Figure 4.10: Pressure, impedance and changes in diameter of a section of 10 cm guinea pig proximal colon from oral to anal in y-axis and time in x-axis: (a) PMap with impedance signals, colours represent changes in pressure ranging from 0 to 60 mmHg. (b) DMap with impedance signals, greyscale represents diameters ranging from 4 to 11 mm. Impedance is shown in arbitrary units in both instances.

Comparing pressure, impedance and video data shows that an increase in luminal diameter due to the passage of a fluid bolus is closely followed by a contraction and an increase in pressure. In the results, it can be seen these relations clearly. Observing the DMap and PMaps representations, dark regions in DMap mean large diameters due to ingress of content and muscle relaxation. The PMaps indicate that these are regions of low pressure, also indicating that the muscles have relaxed. After relaxation (increase in diameter) a muscular contraction generates a decrease in luminal diameter and increase in intra-luminal pressure. This is also related to impedance as it is inversely proportional to change in diameter when the conductivity of the content is constant.

4.4 Conclusions

This study represents the first truly high resolution (10 mm spaced sensors) impedance fibre optic manometry data studying muscular contractions and the associated movement of luminal content. The use of the FBGs as the pressure sensors has allowed us to form a catheter with a large number of pressure sensors in a limited space and same number of impedance sensors, which in turn has allowed a highly flexible composite catheter with a diameter of < 3 mm which is smaller than commercially available HRIM catheters. The dual lumen nature of the catheter provides additional real estate to run the electrical wiring allowing the pressure and impedance functions to be assembled separately avoiding any mechanical interference between electrical and optical sensors. The custom HRIM catheter data has been validated against data obtained from direct video imaging.

Chapter 5

Experimental results from High Resolution Impedance Manometry catheters

The study presented in this chapter is the subject of the following paper:

Ruiz-Vargas, A, Mohd Rosli, R, Wiklendt, L, Arkwright, JW. Effect of electrode separation on High-Resolution Impedance Manometry catheters for *ex-vivo* animal experiments. *Neurogastroenterology & Motility*. 2018;e13488. doi:10.1111/nmo.13488.

5.1 Introduction

This chapter is a follows on from **Chapter 4**. In this chapter, evaluation of two different electrode separations (10 and 20 mm) on HRIM catheters for assessment of colonic motility and bolus transit studies are presented. *In-silico* and *ex-vivo* experiments were performed to evaluate: 1) the effect of the electrode separation on HRIM catheters, and 2) the impedance signals during the passage of a single isolated bolus and a complex bolus consisting of two closely spaced boluses with no clear gap between to simulate small changes in luminal cross-section on the impedance measurement.

5.2 Materials and methods

5.2.1 Numerical study

The model of the gastrointestinal tract designed in **Chapter 3** has been used for studying the electrode separation of the intraluminal impedance catheter for bolus transit. In this instance, the configuration of the catheter and electrodes were slightly different – as commercial HRIM catheters differ from the catheter used in Chapter 3 – and had the following dimensions: length = 150 mm; outer diameter = 3.2 mm, with two ring electrodes (length = 4 mm; outer diameter = 3.2 mm) separated by either 10 mm or 20 mm. The catheter was positioned on the axis of the model, then, two specific shape boluses were created; a single bolus of 11 mm outer diameter (Figure 5.1(a)), and two consecutive overlapping boluses with different dimensions (first 10 mm and second 11 mm), see Figure 5.1(b). The size of the boluses was based on results from previous experimental studies (Dinning, Costa, Brookes and Spencer, 2012). Twenty-six and thirty-five different static models were created for the single and overlapping boluses, respectively, changing the boluses position by 2.5 mm (from left to right) each time to simulate bolus propulsion.

The electrical properties (at 1 kHz) of different layers of the tissue in the model were the same as used in Chapter 3 and used by Kassanos et al. (2015) and are shown again in Table 5.1. Similarly, the electrical properties for the catheter tube and electrodes were selected from the Material Library provided in ANSYS Electronics (ANSYS Electronics desktop, ANSYS Inc, Canonsburg, Pennsylvania, USA) as in Chapter 3. The luminal content used for the simulations was a saline solution (0.9% NaCl) which has a conductivity of 1.44 S/m and a relative permittivity of 80.

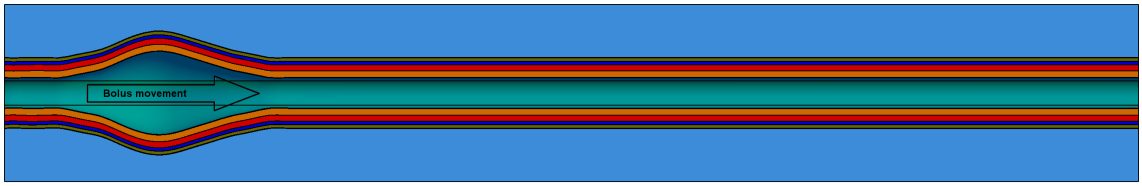

(a)

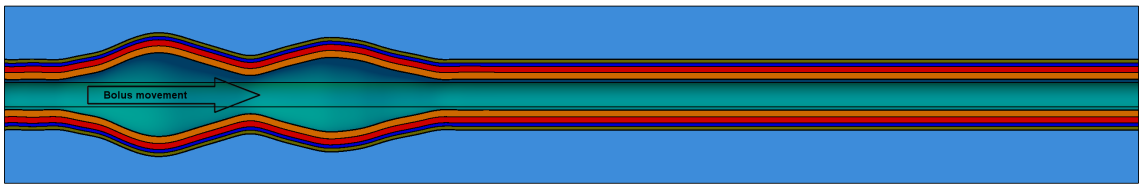

(b)

Figure 5.1: Lateral cross-section of the model simulating (a) one bolus and (b) two consecutive boluses. The electrodes are not represented here, but they are placed in the middle of the model. In both instances, the passage of the bolus goes from left to right. The layers of the GI tract are represented in different colours.

Table 5.1: Electrical properties of different GI tract layers used in the FEM model.

	Electrical properties	
	Conductivity, σ (S/m)	**Relative Permittivity, ε_r**
Mucus	1.1	72
Mucosa	0.532	2.64×10^5
Submucosa	0.383	3.03×10^5
Circular muscularis	0.321	4.35×10^5
Longitudinal muscularis	0.5	1×10^6
Serosa	0.383	3.03×10^5
Surrounding tissue	0.148	1.97×10^5
Luminal content	1.44	80

An excitation current of 10 µA was applied between the pair of electrodes. The different models (with bolus positions at different points along the tract) were then simulated using the DC electrical conduction component of the ANSYS Maxwell software platform. Each simulation was carried out on 12 CPUs Intel ® Xeon ® CPU E5 – 2630 v2 desktop computer running at 2.60 GHz with 128 GB of RAM, with OS Windows 8.1 Enterprise. The models were solved using the 3D model's method. The meshes used in the simulations varied from model to model, with a maximum number of tetrahedral elements of 1,074,087. The tetrahedral elements of each model was dependent on the complexity and was determined automatically by the Maxwell adaptive meshing algorithm.

Impedance sensitivity

Similarly to Chapters 3 and 4, the sensitivity distribution of the bipolar electrode system was also simulated within the lumen to define the region of measurement when there is no presence of a bolus and when a bolus is passing through.

5.2.2 Experimental studies

Four New Zealand rabbits (two rabbits per catheter), weighing 0.96 – 1.10 kg were euthanized humanely by intravenous phenobarbitone sodium injection in accordance with approval by the Animal Welfare Committee of Flinders University (Animal Ethics Number: 820/12). A midline ventral incision was made and the proximal colon was excised. The specimen was placed into a beaker containing oxygenated Krebs solution (in mM: $NaCl$, 118; KCl, 4.7; NaH_2PO_4, 1.0; $NaHCO_3$, 25; $MgCl_2$, 1.2; *D- Glucose*, 11; $CaCl_2$, 2.5) and bubbled with 95% O_2/ 5% CO_2. The faecal pellets were gently flushed out of the colonic segment with Krebs solution.

Catheters

Two catheters were used for these experiments: (1) a high-resolution impedance manometry (HRIM) catheter (Sandhill Scientific, Diversatek Healthcare, Milwaukee, WI, USA), and (2) the custom-made impedance fibre optic manometry catheter presented in Chapter 3. The commercial catheter contains 32 pressure sensors at 10 mm intervals and 16 impedance segments, with ring electrodes at 20 mm intervals (Figure 5.2(a)). The outside diameter of the catheter body was 3 mm, 5 mm at the pressure sensors and 3 mm at the impedance sensors. The custom-made catheter consists of 35 pressure sensors based on fibre optic sensing technology (Arkwright et al., 2011; Arkwright, Underhill, Maunder, Blenman, Szczesniak, Wiklendt, Cook, Lubowski and Dinning, 2009) at 10 mm intervals, 16 impedance segments with a diameter of 2.8 – 3 mm, and a 10 mm electrode separation (Figure 5.2(b)).

The use of optical fibres provides additional space for impedance wiring without reducing the flexibility or adding to the overall diameter of the catheter. In this instance, the outside diameter along the custom-made catheter was 3 mm, and the flexibility of the catheter was qualitatively similar to the Sandhill catheter.

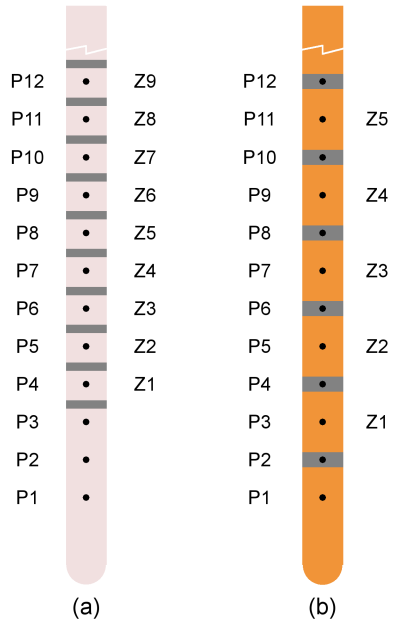

Figure 5.2: Representation of both catheters; (a) configuration of the custom-made fibre optic catheter and (b) configuration of commercial HRIM impedance catheter. Black dots represent the pressure sensors (named as P_i) and dark-grey square represent the position of the electrodes (the impedance values, Z_i, are measured between two neighbouring pairs of electrodes).

Equipment

Three different data sets were recorded in the experiments; impedance, pressure, and diameter of the luminal segments. This allowed us to directly correlate contractile activity measured using the solid state and optical pressure sensors with the luminal cross-section measured using impedance. The dynamically varying luminal diameters were confirmed using direct video imaging of the preparation.

A digital video camera (Canon Legria HF S20. Ota, Tokyo, Japan), positioned above the preparation was used to record video images to create spatiotemporal maps of changes in diameter, referred to as 'Dmaps' (Hennig et al., 1999).

Intraluminal impedance and pressure data from the commercial HRIM catheter were recorded using the Bioview impedance manometry software (Sandhill Scientific Inc, Highlands Ranch, CO, USA). For the custom catheter, two acquisition systems were used: (1) the InSight system for intraluminal impedance data, and (2) an optical interrogator unit (FBGS FBG-scan 804; FBGS International, Geel, Belgium) connected to the fibres for the pressure profile along all the 35 pressure sensors simultaneously.

During the experiments, time stamps were taken in all recordings in order to synchronise impedance, pressure and diameter signals.

Experimental set-up and protocol

The excised sections of proximal colon were then placed into an organ bath containing the same Krebs solution warmed to 36 - 37°C. The specimen was left to equilibrate for 20 to 30 minutes before recording began. The gut was prepared and place in the organ bath as described in Chapter 4 (Section 4.2.4).

5.2.3 Construction of spatiotemporal and composite maps

The videos of each experiment were converted into spatiotemporal maps of changes in diameter (DMaps), in the same way as reported in Chapter 4 (section 4.2.5). The recorded pressure and impedance traces were also converted to spatiotemporal pressure maps (PMaps) and impedance maps (IMaps), interpolating between points at 10 or 20 mm intervals, using a custom written program in Matlab (MathWorks, Natick, MA, USA).

Composite maps, such as DPMaps (DMaps and PMaps) and IPMaps (IMaps and PMaps), were then created in Matlab. Spatial resolution of composite maps were adjusted to that of the lowest resolution method, i.e. for the custom catheter was 10 mm and for the commercial catheter was 20 mm.

5.3 Results

5.3.1 Numerical study

Impedance magnitudes were calculated by dividing the voltage drops across the pair of electrodes by the frequency dependent current. The results are presented in admittance (inverse of impedance) to be in agreement with the variations in diameter. The admittance signals of 10 and 20 mm electrode separation for the passage of one and two consecutive boluses are shown in Figure 5.3. In both instances, changes in admittance occurred slightly earlier with 20 mm electrode separation, whereas for 10 mm electrode separation were seen when the bolus was closer to the centre between the electrodes. In addition, the change in admittance for 20 mm electrode separation is gradual unlike the 10 mm electrode separation, which has a faster rise and fall rate, especially when only one bolus is passing

through.

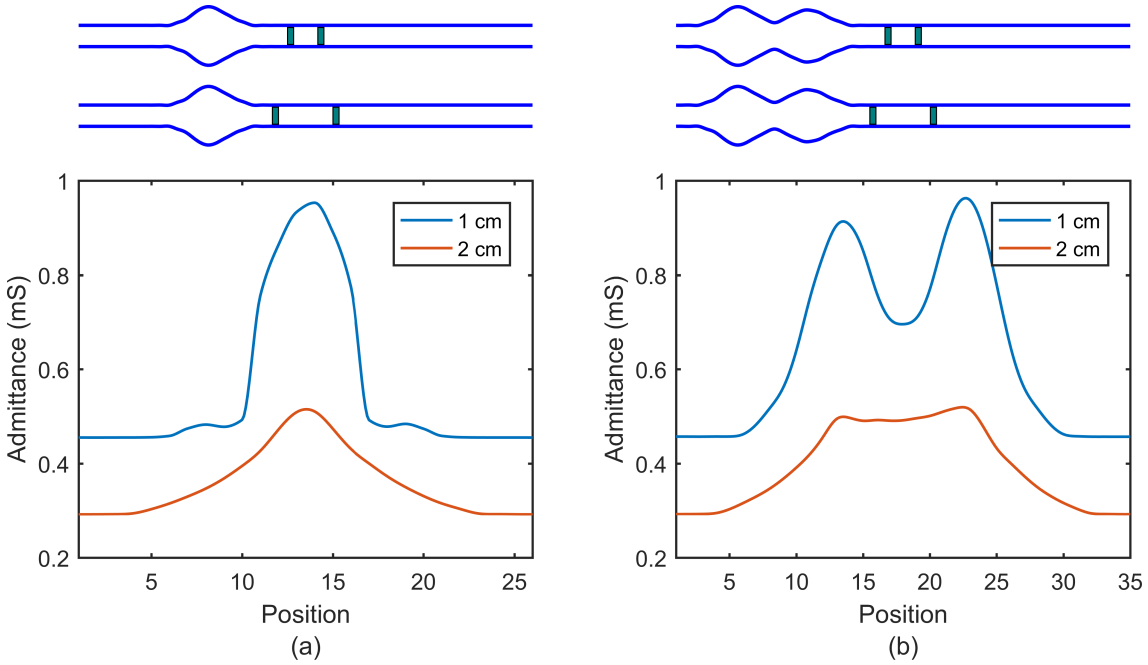

Figure 5.3: Admittance magnitude signals for 10 mm and 20 mm electrode separation for the passage of (a) a single bolus and (b) two consecutive boluses. The position (x-axis) represents the different position of the bolus for each simulation, each position equals a bolus travel of 2.5 mm.

The pertinent outcome, shown in Figure 5.3(b), is that the 20 mm electrode separation is not able to fully resolve the passage of the two consecutive boluses; the admittance magnitude is almost constant as the complex bolus passes through. On the other hand, for 10 mm electrode separation the change in admittance clearly picks up the transition of both boluses and the peaks are proportional to the bolus size.

Figure 5.4 shows the normalized distributed sensitivity on the simulated model with 10 mm and 20 mm electrode separation for the passage of a bolus. When there is no presence of a bolus, the sensitivity is evenly distributed and enclosed along the empty lumen for both cases, see Figures 5.4(a) and 5.4(c). Surprisingly, the distributed sensitivity completely changed when the bolus is in the middle between the electrodes; the volumes that had most contribution were adjacent to the electrodes (Figures 5.4(b) and 5.4(d)).

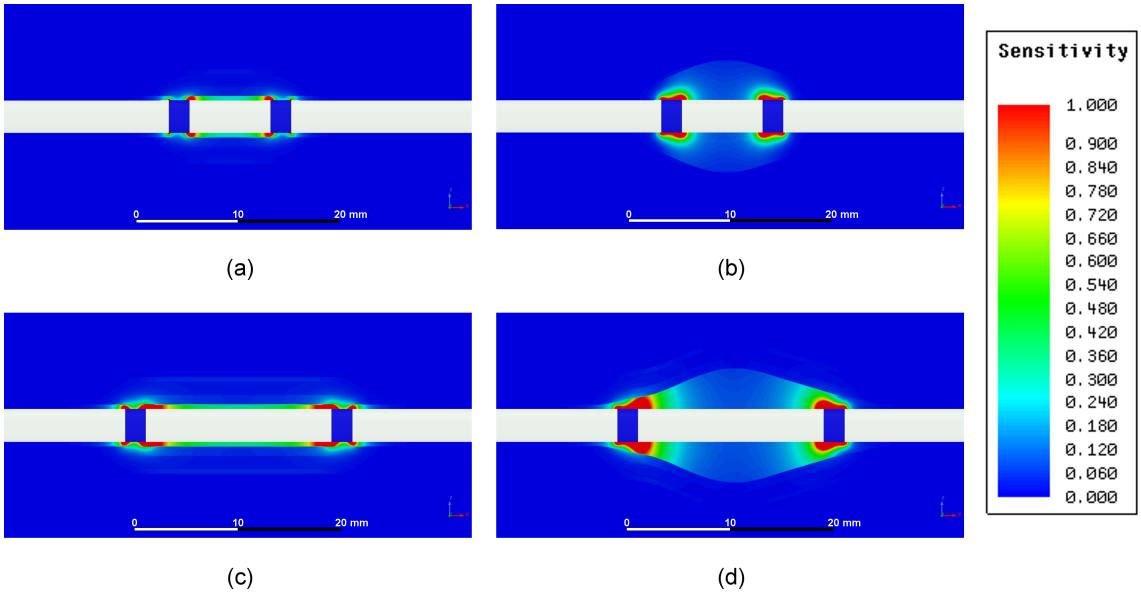

Figure 5.4: Normalised distributed sensitivity on the simulated model for: 10 mm electrode separation (a) with no bolus presence and (b) with presence of a bolus; and for 20 mm electrode separation (c) with no bolus presence and (d) with presence of a bolus.

5.3.2 Experimental studies

Figure 5.5 shows the DMaps produced from the video recordings of studies with each type of catheter (Note: DMaps are produced from the video imaging of the preparation, not from the catheter data). In both instances, myogenic and neurogenic contractions were visible in the DMaps, as previously shown by Dinning, Costa, Brookes and Spencer (2012). Both contractions cause changes in diameter as detected on DMaps, but myogenic contractions are not necessarily propulsive and are initiated by non-neuronal pacemaker cells; neurogenic contractions produce stronger, coordinated contractions causing propulsion of luminal content (Costa et al., 2013; Dinning, Costa, Brookes and Spencer, 2012).

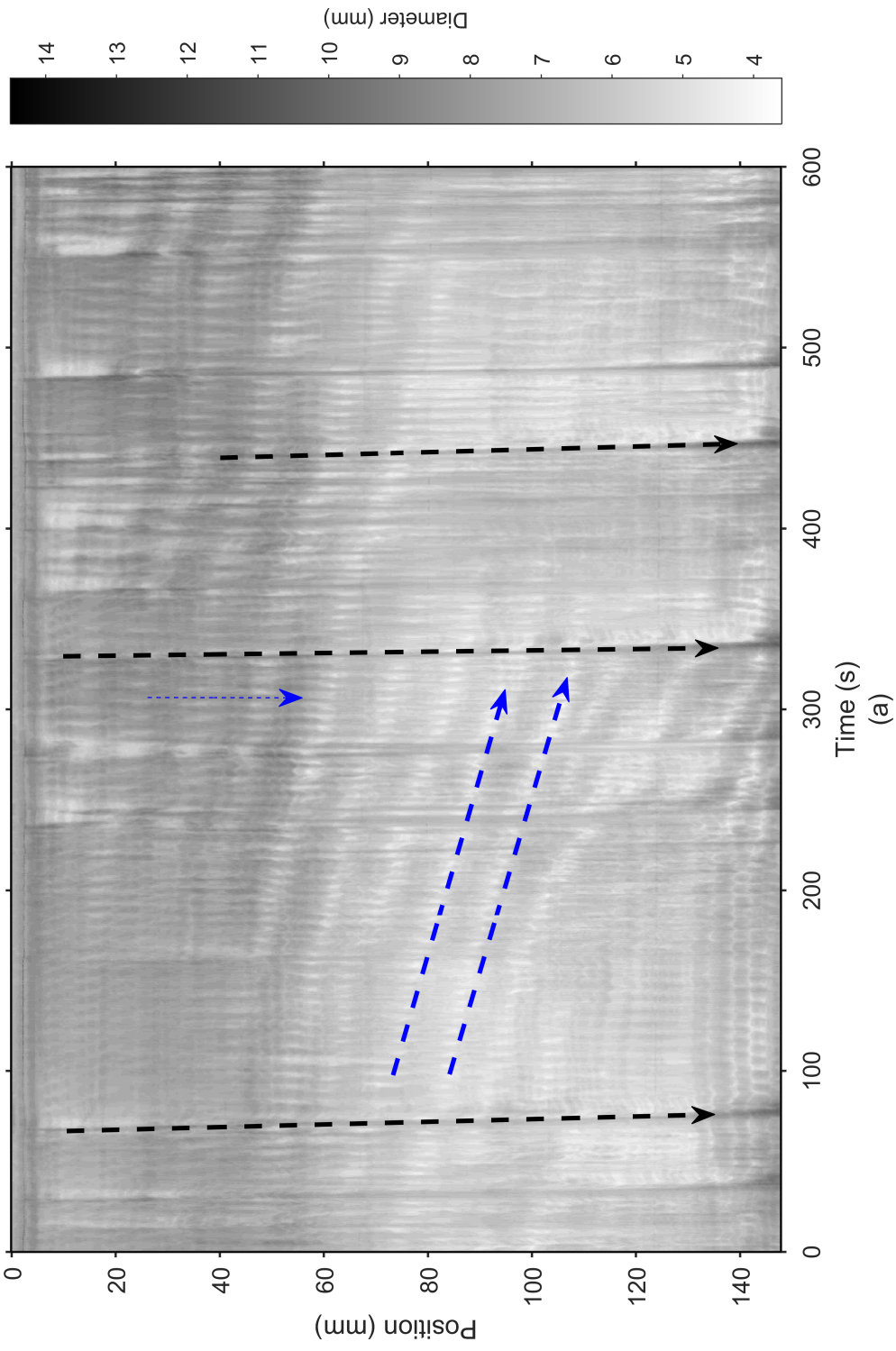

Figure 5.5: DMaps of two recordings for about 1 hour (a) with the custom HRIM catheter and (b) with the commercial HRIM catheter.

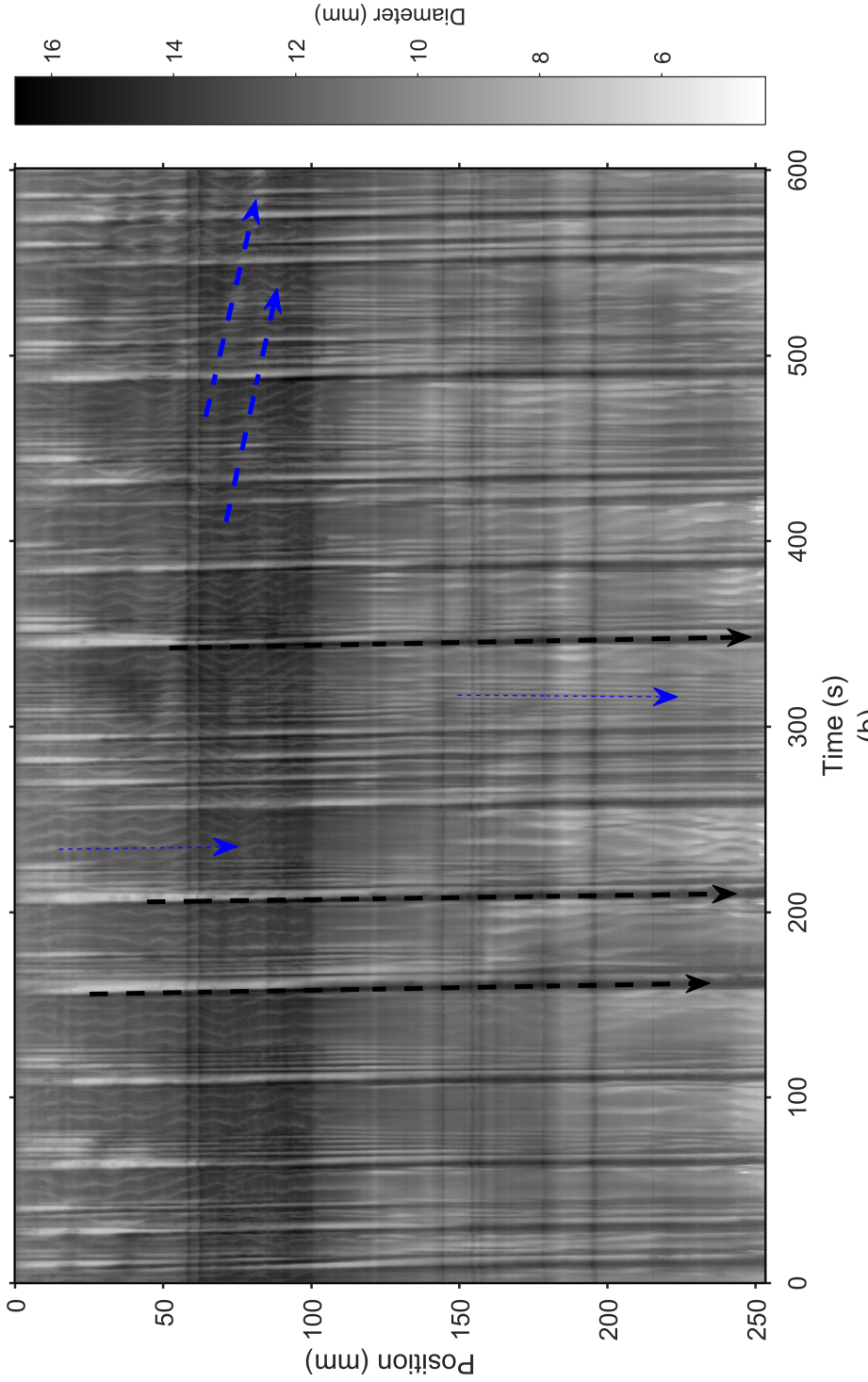

Figure 5.5 continued ...: Neurogenic contractions (thick hatched black arrows) and two types of myogenic contractions (thick hatched blue arrows indicate ripple contractions; thin hatched blue arrow indicate high frequency ripples).

In addition to the DMaps shown above, DPMaps and IPMaps were also obtained for both set-ups. Figures 5.6(a) and 5.6(b) show DP and IP maps respectively for the custom made HRIM catheter and Figures 5.6(c) and 5.6(d) show DP and IP maps respectively for the commercial HRIM catheter respectively. The colour legends on the right correspond to changes in both pressure and diameter, and pressure and admittance for the DPMaps and IPMaps, respectively. Propagating boluses and myogenic contractions can be seen in both DPMaps (striations in green and red colouring seen in Figures 5.6(a) and 5.6(c)), however, myogenic contractions are only resolved in the IPMap from our custom made HRIM catheter (striations in blue colouring seen in Figure 5.6(b)) and not in the IPMap from commercial HRIM catheter (Figure 5.6(d)). On the right side of the composite maps, the legend also shows the points of the selected regions indicated as white lines. In Figure 5.6(a), the Diameter/Pressure legend shows a variation in diameter ($\sim$ 1 mm), and simultaneously, in Figure 5.6(b), the Pressure/Admittance legend shows a considerable variation in admittance ($\sim$ 0.1 mS). On the other hand, in Figure 5.6(c), there is a variation in diameter ($\sim$ 2 mm) on the Diameter/Pressure legend but the variation in admittance (Figure 5.6(d)) is too small ($\sim$ 0.02 mS) to be detected in the composite map (IPMap).

The experimental data for admittance, pressure and diameter recorded during the propagation of a bolus and during a period of myogenic activity were then compared with the simulated results shown in Figure 5.3. Figure 5.7 shows the admittance, pressure and diameter recordings from the commercial and the custom-made HRIM catheters. Figures 5.7(a)-(c) correspond to the custom-made HRIM catheter (10 mm electrode-separation) whereas Figure 5.7(d)-(f) corresponds to the commercial HRIM catheter (20 mm electrode-separation). The admittance and pressure recordings during the propagation of a bolus with its respective diameter signal on top are shown in Figures 5.7(a) and 5.7(d) respectively, and Figures 5.7(b) and 5.7(e) show the admittance and diameter recording of myogenic contractions, respectively for each catheter configuration. Figure 5.7(c) and 5.7(f) show the admittance plotted against diameter during the myogenic events seen in Figures 5.7(b) and 5.7(d), the correlation between admittance and diameter using Pearson's correlation coefficient and a linear fitting to the data points. The PCC values showed a strong correlation for the custom HRIM catheter (PCC = 0.85 CI = 0.83 – 0.86, $p < 0.05$) during myogenic contractions whereas for the commercial HRIM catheter the correlation was weaker (PCC = 0.55, CI = 0.5 – 0.59, $p < 0.05$). The linear fitting for the custom catheter has a sensitivity of 0.047 mS/mm which is approximately ten times bigger than the one for the commercial catheter (0.004 mS/mm).

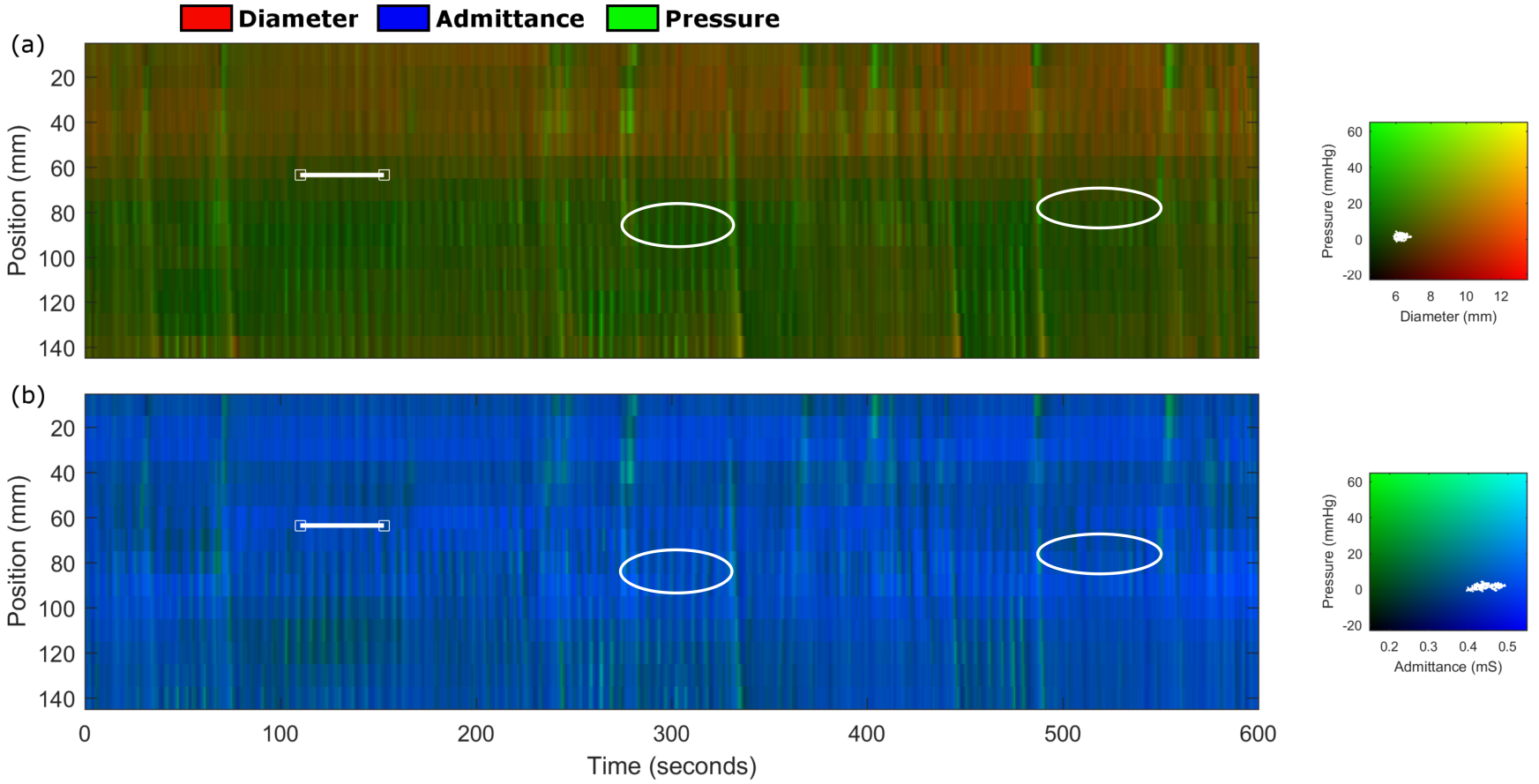

Figure 5.6: Composite maps of admittance, pressure and diameter during experiments carried out with both catheters. (a) DPMap and (b) IPMap for custom HRIM catheter. (c) DPMap and (d) IPMap for commercial HRIM catheter. Legends are shown on the right of the composite maps in conjunction with the data points along the selected time frame in the maps (shown as a white line).

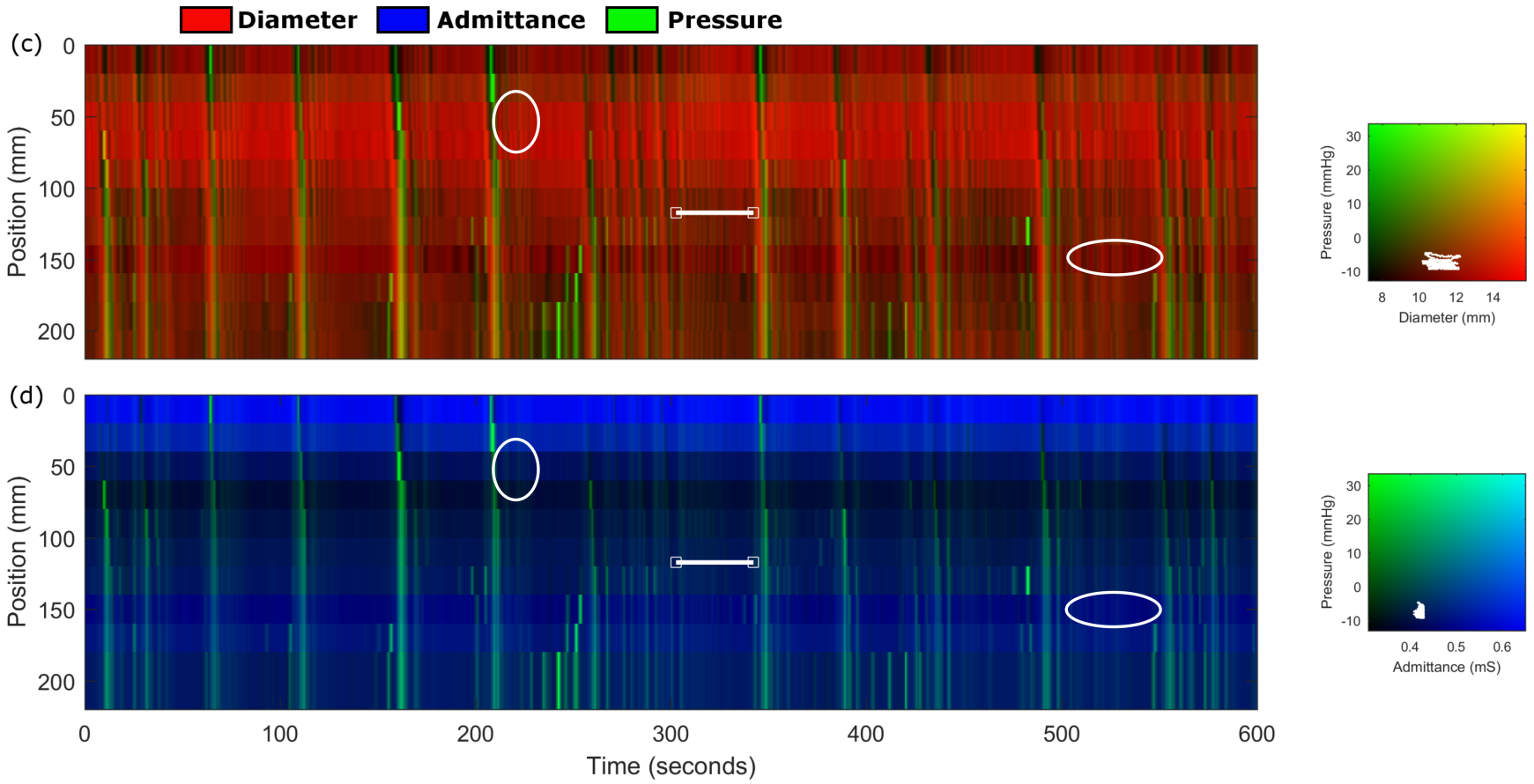

Figure 5.6 continued ...: Neurogenic contractions can be seen in regions where green predominates. Regions of myogenic activity are indicated by the white ellipses and lines. Data points for pressure/diameter and pressure/admittance from the withe lines are shown in the legends. A variation in diameter ($\sim$ 1 mm) (a) and admittance ($\sim$ 0.1 mS) for (b) whereas for (c and d) the variation in diameter was ($\sim$ 2 mm) and in admittance ($\sim$ 0.02 mS).

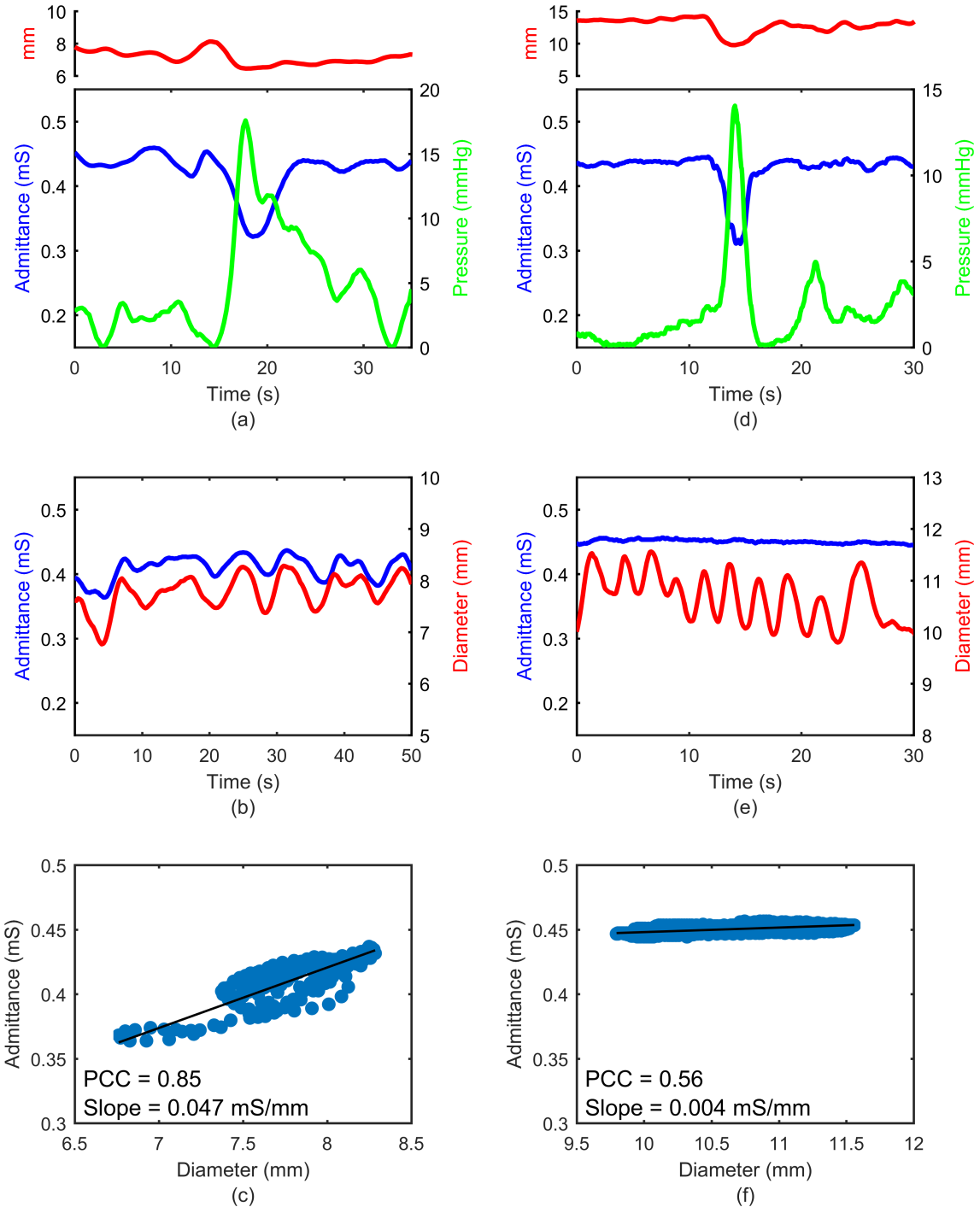

Figure 5.7: Experimental results of 10 mm electrode and 20 mm electrode-separation catheters. (a), (b) and (c) correspond the data obtained with the custom-made catheter (10 mm electrode separation); (d), (e) and (f) to the commercial catheter (20 mm electrode separation. (a) and (d) show the admittance and pressure signal during the passage of a bolus with the diameter signal on top; (b) and (e) show the admittance and diameter signal during myogenic contractions. (c) and (f) show the admittance dispersion against diameter during the myogenic event and the sensitivity of each catheter to changes in diameter.

5.4 Discussion

5.4.1 Numerical study

The normalised sensitivity analysis (Figure 5.4) showed us that regions near the electrodes contribute more to the total measured impedance when there is a propagation of a bolus. A large electrode separation will affect the measurement and prevent resolution of the fine details corresponding to the myogenic activity. This agrees with the admittance magnitude signals shown in Figure 5.3(a) and 5.3(b). In the simulations, the initiation of the changes in measured admittance for the 20 mm electrode separation occurred at least two positions earlier due to the larger separation between electrodes, and those changes were gradual whereas for 10 mm electrode separation the changes were more localised to the bolus, resulting in better spatial resolution, as would be expected for the closer spacing of the electrodes.

Overall, according to the simulation, the 10 mm electrode separation is also more sensitive as its admittance has larger increments as a function of luminal diameter than 20 mm electrode separation. Our previous study shown in Chapter 3, showed that the sensitivity of the impedance measurement can also be increased using luminal content with a higher conductivity.

5.4.2 *Ex-vivo* studies

The DMaps (Figure 5.5), used as the gold standard for identifying myogenic and neurogenic contractions, confirmed that these contractions were present in both sets of experiments (see hatched lines in Figure 5.5). Both catheters were able to detect bolus propagation, see Figures 5.6 and 5.7. The propagation of the bolus can be readily identified in the DMaps due to the larger diameter (darker streaks) induced by the presence of the bolus, and followed by a reduction in diameter (white regions indicating a narrower diameter). In this instance, the propagation of the bolus is also identified from pressure and admittance signals due to the large increase in pressure and decrease in admittance as luminal occlusion occurs to propel the bolus forward, see Figure 5.7(a) and 5.7(d).

Perhaps the most unexpected finding was the detection of subtle myogenic ripples with the admittance data from the custom HRIM catheter. These ripples were evident in the DMaps and DPMaps for both configuration, but were only seen in IPMaps for the custom HRIM catheter (10 mm electrode separation), and can be identified by the striations in blue colouring in the lower plot of Figure 5.6(b). This is also shown in the graphs from

Figure 5.7(b) and 5.7(e); the changes in admittance for the 10 mm electrode separation are correlated with the changes in diameter. However, the changes in admittance for the 20 mm electrode separation did not show any significant correlation with the diameter showing only small fluctuations close to the noise floor of the measurement. It is believed that the identification of myogenic contractions with the custom HRIM catheter was attributed to the increase in sensitivity to changes in diameter seen in Figures 5.7(c) and 5.7(f). Note, that the IPMap's spatial resolution for the custom manometry impedance catheter improved to 10 mm as the electrode intervals were also reduced from 20 mm to 10 mm.

5.4.3 Comparison of numerical and experimental results

The numerical results agree qualitatively with the experimental results during the propagation of the bolus. The admittance values in the numerical data are in the range of 0.2 – 1 mS, which are in close agreement with the experimental data within 0.2 – 0.5 mS. Some differences between the numerical and experimental results were seen (Figures 5.3, 5.7(a) and 5.7(d)), for example during the bolus passage in the numerical results, there is a large increase in admittance due to the passage of the bolus. However, in the experimental data for bolus propagation during neurogenic contraction, only a slight increase in admittance was seen by the custom HRIM catheter due to the bolus, followed by a decrease in admittance (Figures 5.7(a) and 5.7(d)). This difference between the numerical and experimental results could be explained by the fact that, to simplify the model and keep calculation time to a manageable level, the simulation assumes that the catheter is on the axis of the lumen and the lumen remained open. On the other hand, the observed decrease in the experimental results is explained by the occlusion of the lumen at the trailing edge of the bolus due to the neurogenic contraction, which helps propel the bolus, squeezing the gut onto the catheter. The luminal wall has lower conductivity than the Krebs solution content; hence when the lumen gets in contact or closer with the electrodes, a decrease in admittance occurs according to Equation 4.1 (Chapter 4, Section 4.2.3) of total measured impedance as a function of the distributed sensitivity.

The admittance trend during the two consecutive boluses from the simulated model agrees with the admittance trend from the experimental results during myogenic contractions for both configurations. It can be seen, in Figures 5.3(b) and 5.7(b) and 5.7(e), that the changes in diameter are followed by a proportional change in admittance for the custom HRIM catheter, however, for the commercial HRIM catheter, the changes in diameter are not followed by the admittance signal. After the subtle changes in diameter due to the small contractions, there is not a full occlusion of the lumen onto the catheter. That

is why, the large decrease in admittance was not observed, unlike the ones observed for neurogenic contractions.

5.4.4 Benefits of closely spaced HRIM catheters in small and large bowel studies

The improvements in data from HRIM catheters with reduced electrode separation will have the potential to provide additional information in all regions of the GI tract, especially from regions below the stomach that are hard to monitor, and where contractions cannot be initiated on demand. The ability for the closely spaced electrodes to pick up fine detail of changes in luminal diameter linked to high resolution manometry data will allow more complex motor patterns to be analysed without the need for video imaging modalities.

A significant advantage of using optical fibre sensors for the manometric function of the catheter is that up to 36 pressure sensors can be located on a single length of 0.2 mm diameter optical fibre. This allows us to manufacture catheters with up to 144 discrete sensing elements (containing 4 optical fibres) without increasing the outer diameter of the catheter. This leaves considerably more volume within the catheter to contain the wires needed for the impedance electrodes. This approach will allow us to make catheters for the lower gastrointestinal tract that are longer and contain more sensing elements than conventional solid state catheters of the same diameter while at the same time providing more space for impedance wiring. However, increasing the number of impedance wires will still limit the flexibility of the catheter, and hence ultimately limit the number of impedance electrodes that can be included in a given diameter.

5.5 Conclusions

The aim of the study was to examine the effect of electrode separation in HRIM catheters for assessment of colonic motility. Both configurations were able to detect bolus propagations; however, only the 10 mm electrode separation was able to differentiate between two closely spaced boluses and also detect myogenic contractions from IPMaps from the admittance signal. As the animal studies move towards *in-vivo* experiments, it would be a significant improvement to be able to detect these ripples since video images of the luminal activity would not be viable.

Chapter 6

Development of an electrical impedance probe with built-in pressure and temperature sensors

The study presented in this chapter is the subject of the following paper:

Ruiz-Vargas, A, Ivorra, A, Arkwright JW. Design, construction and validation of an electrical impedance probe with contact force and temperature sensors suitable for *in-vivo* measurements. *Scientific Reports*. 2018;8(1):14818. doi:10.1038/s41598-018-33221-4.

6.1 Introduction

Chapter 6 describes the design, and construction of an electrical impedance pencil probe incorporating a temperature compensated contact force sensor to address the variability issue common to bioimpedance measurements (**Aim 4**). The pencil probe has been designed to fit into the instrument port of an endoscope, making it suitable for *in-vivo* diagnostics. An *ex-vivo* assay on a section of excised proximal colon from a guinea pig is performed to validate the data and compare the results to previously published results.

Bioimpedance measurements can be performed by inserting needle electrodes into the tissue or by surface electrodes in contact with the tissue (Rigaud et al., 1996). Using needles, there is a risk of damaging the tissue. Contact electrodes avoid damaging the tissue. However, in *in-vivo* studies, it has been shown that contact electrodes produce measurements with big variability (González-Correa et al., 2005; Knabe et al., 2013; Lundin et al., 2011). That is, measurements with contact electrodes are much less repetitive than those with needle electrodes. It is thought that the main reason for such lack of repeatability is variability in the applied contact-force. This force causes an increase in the pressure within the tissue which pushes away the extra-cellular fluids hence causing an increase in the impedance (Zhou et al., 2016). In addition, if the sample is sandwiched between the probe and an insulating surface (as it is the case in the present study), this force compresses the tissue sample and reduces its thickness hence causing a further increase in the impedance.

The variability of readings of a small probe (diameter 3.2 mm) due to the force applied has been demonstrated to be significant in *in-vitro* studies (González-Correa et al., 2005; Lundin et al., 2011). In these studies, the applied force was recorded by a weighing scale and the contact pressure was calculated as the ratio between the force and the contact area of the probe. González-Correa et al. (2005) showed an increase up to 80% on resistivity readings on human gastric tissue for a contact pressure range of 1 kPa to 50 kPa. Lundin et al. (2011) reported the resistivity readings taken in a rabbit oesophagus when applying light and hard force manually, showing a higher resistivity when hard force was applied.

Keshtkar and Keshtkar (2008) studied the effect of the probe size on the variability of readings, where concluded that the smaller the probe, the bigger the variability. Because larger probe size avoids the expulsion of fluid below the tip. However, the size of the probe is critical for minimally invasive clinical procedures when using an endoscope.

In general, solid-state pressure sensors are not suitable for this application because of their size. A further issue for electrical sensors for these sort of applications is that the long leads are susceptible to electrical noise and cross-talk due to the close proximity with the

impedance sensor wiring. For these reasons, an alternative option based on fibre optics sensing technology was used. A similar approach, using fibre optic sensing technology, has been used before on catheters for cardiac radio frequency ablation to prevent damage during ablation (Ho et al., 2012).

As mentioned in Chapter 4, fibre optic techniques are particularly suitable for biomedical applications due to the small size, high flexibility and immunity to electromagnetic interference (Baldini et al., 2008; Dziuda et al., 2012; Peng-fei et al., 2011; Pleros et al., 2009). In particular, fibre Bragg gratings (FBGs) have the advantage of high sensitivity and stability and have been used to measure pressure, strain and temperature (Hung et al., 2012; Kennedy et al., 2012; Mignani and Baldini, 1995; Peng-fei et al., 2011; Poeggel et al., 2012) making them highly suitable for this application.

6.2 Materials and methods

6.2.1 Design and construction

Figure 6.1 shows the tip of the developed four-electrode probe with an integrated temperature compensated fibre optic force sensor. The tip is composed of three parts; two Polyether Ether Ketone (PEEK) (Ketron PEEK 1000, Dotmar Plastic Solutions, Adelaide, South Australia, Australia) parts and a compliant silicone pad. The design (see 6.1) consists of 5 holes; four for the electrodes arranged in a square configuration and separated 0.9 mm from the axis, and one (in the centre) that holds two optical fibres containing FBGs (draw tower gratings (DTG), FBGS, Geel, Belgium). The finished tip was 3.2 mm in diameter which makes it suitable for use in endoscope port. Polyether Ether Ketone (PEEK) was used for its biocompatibility and good mechanical properties. The two PEEK parts of the tip were CNC-machined in the Australian National Micro-Fabrication (ANFF-SA) facilities.

The silicone part that acts as a compliant layer was formed in a mould made out of 3 pieces of acrylic sheets. In order to clean and activate the PEEK's surface to promote bonding of the silicone part, the two PEEK parts were placed in an air plasma at < 1 mbar prior to assembly. The two parts were then aligned and separated by pins and introduced into the acrylic mould. Silicone (Sylgard 184 Silicone Elastomer Kit, Down Corning, Midland, Michigan, USA) was poured into the mould and left in a vacuum to degas the silicone. At the end, the tip was baked for an hour at 80℃.

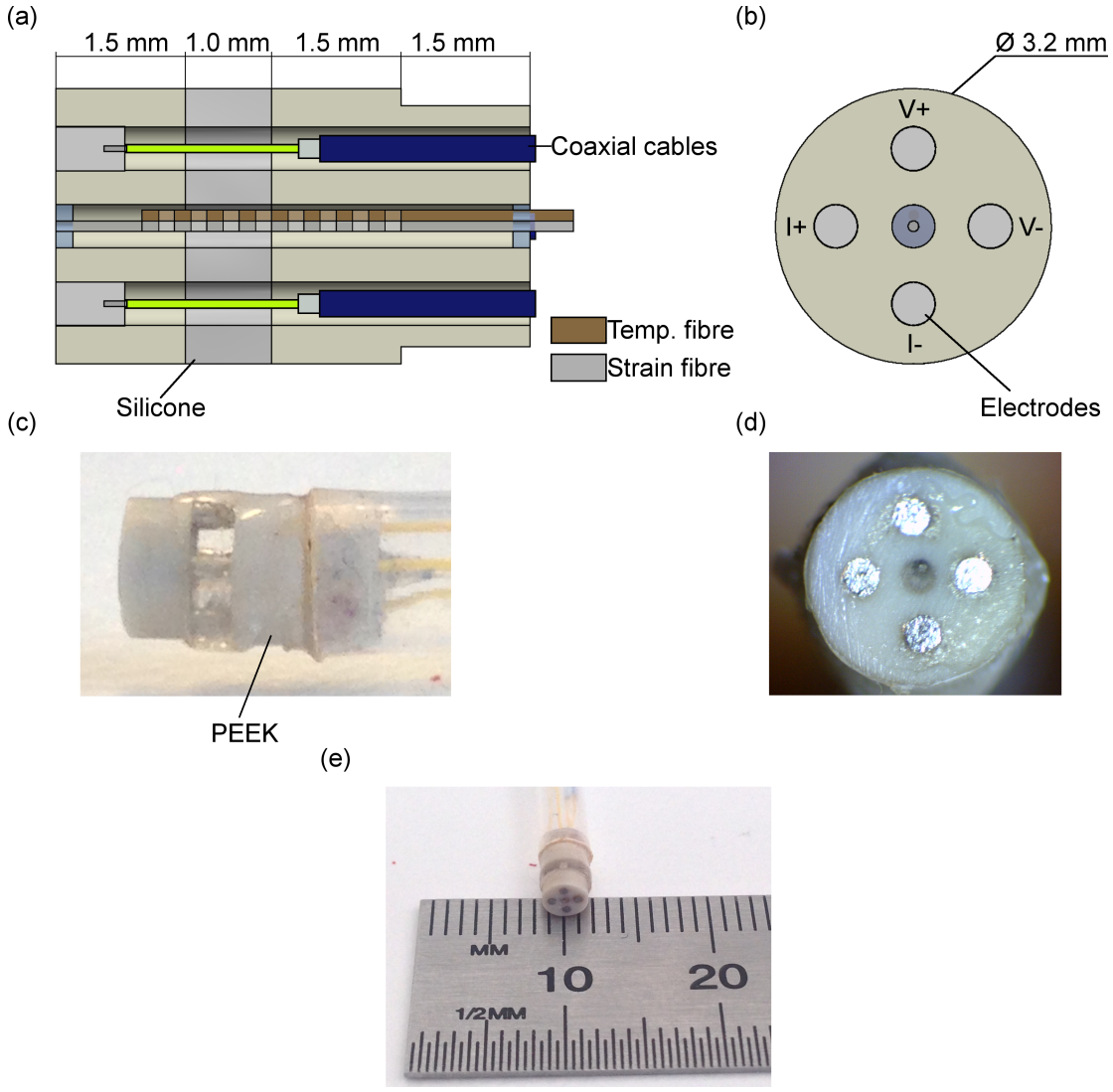

Figure 6.1: Drawings and images of electrical impedance probe: (a) Lateral cross-section of the probe design with coaxial cables, electrodes and fibres assembled. (b) Front view of the probe design. (c) Lateral view and (d) front view of the pencil probe. (e) Device end-effector after assembly.

The two optical fibres containing the FBGs were passed through the hole and then clamped and placed under tension using a linear translation stage. The two gratings were positioned next to each other and one of the fibres was broken off close to the distal end of the grating (this grating was used as the temperature reference grating). Both fibres were glued with UV light glue (EPO-TEK OG198-55, Epoxy Technology, Billerica, Massachusetts, USA) at the proximal end of the tip, and the sensing fibre was glued to the distal end of the tip (this fibre contained the contact-force sensing grating).

Electrodes were made of platinum wires (0.5 mm in diameter and 0.7 mm in length). These were pressed into the tip and wedged in place using the core of the coaxial cables

(Temp-Flex 50MCX-37, Molex, Lisle, Illinois, USA). UV glue (EPO-TEK OG198-55) was then applied to the surface of the tip to seal any cavities. The parts were then cured for another hour in the oven at 80℃. Once cured, the electrodes were filed and polished to form the tip.

Finally, optical fibres and coaxial cables were passed through a 2.8 mm inner diameter and 3.3 mm outer diameter PolyTetraFlouroethelene tube (PTFE AWG 10T, Adtech Polymer Engineering Ltd, Aston Down East, Stroud, UK). Then, the PTFE tube was attached to the end of the tip with the same UV glue used before, see Figure 6.1(e). DB-9 connector and E-2000 connectors were used for the coaxial cables and optical fibres respectively.

6.2.2 Equipment

Figure 6.2 shows a picture of the whole measurement system and experimental set-up. The tip sensor was connected to a custom-made bioimpedance measurement system (BMS), described in Appendix B, and a Micron Optics sm130 interrogator (MOI) (sm130, Micron Optics, Atlanta, Georgia, USA).

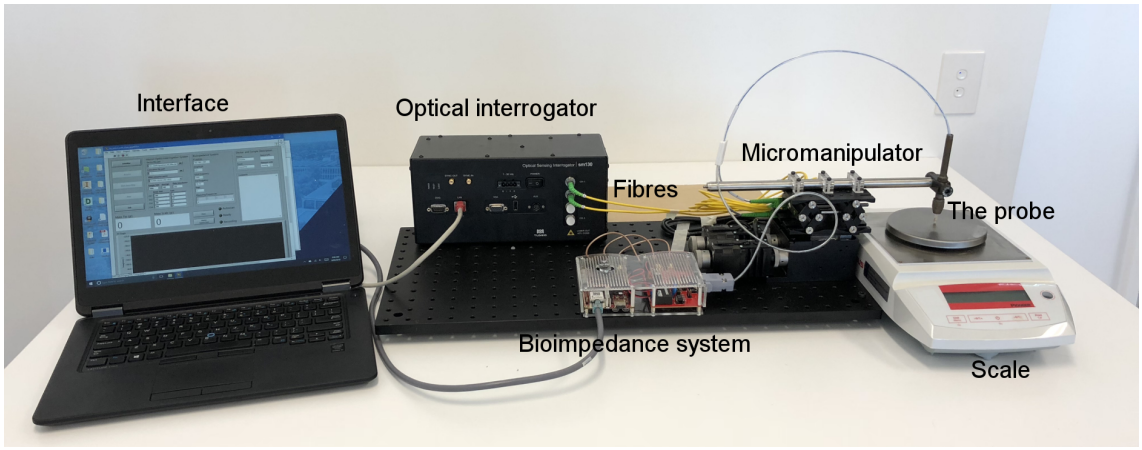

Figure 6.2: Experimental set-up used during the bioimpedance measurements on the tissue.

The BMS is capable of measuring complex impedance from 10 Hz to 1 MHz in a four-electrode configuration. An alternating current with a maximum amplitude of 10 µA, which is below the maximum auxiliary current allowable by safety standard IEC 60601-1 for any electromedical device, was applied between two opposite electrodes at each predetermined measuring frequency, and simultaneously the voltage drop between the other two electrodes was measured.

The MOI interrogator uses a scanning laser covering the range 1510 nm to 1590 nm

wavelength to monitor FBGs at 1 kHz. To reduce the noise a 100 times average was used, decreasing the effective sampling rate down to 10 Hz.

A force scale (Pioneer PA143, Ohaus, Parsippany, New Jersey, USA) was used to calibrate the device and compare with the data from the force sensor.

Output data from the BMS, the MOI and the scale were displayed and recorded in real time using a custom software application built in LabVIEW (version 2015 sp1, National Instruments, Austin, Texas, USA).

6.2.3 Impedance calibration

Agar-agar models (Ivorra et al., 2009) were used to calibrate the impedance probe. These models consisted of gel phantoms that mimic the conductive properties of biological tissues. Two Agar-Agar models prepared with 0.9% (0.150 M) and 0.09% (0.0150 M) NaCl saline solutions were used to calibrate the impedance probe and determine the spectral range of the whole impedance measurement system. The conductivities of these two samples (1.440 S/m and 0.144 S/m) approximates the range of conductivities of gastrointestinal tissue (Mulett-Vásquez et al., 2016). The probe was positioned on each Agar-Agar model and the complex impedance values at 14 different frequencies in the frequency range of 1 kHz to 1MHz, separated logarithmically, were obtained. A hundred measurements were taken to generate average values of the impedance magnitude and phase angle at each frequency.

From those measurements, I evaluated the useful frequency range and calculated the cell constant of the electrode configuration. The cell constant (K, units: m^{-1}) is a scale factor for converting the resistance values (R, units: Ω) into resistivity (ρ, units: Ω.m), and is calculated from Equation A.8 from Appendix A.

$$K = \frac{R}{\rho} \tag{6.1}$$

In addition, the cell constant was also computed through a simulation in ANSYS Maxwell (ANSYS Electronics Desktop, ANSYS Inc, Canonsburg, Pennsylvania, USA). The model consisted of a cylindrical PEEK part (length = 2 mm, outer diameter = 3.2 mm) containing four platinum electrodes (length = 2mm, outer diameter = 0.5 mm, spread and separated 0.9 mm from the axis), a lower surface of glass and a layer of saline content between the tip and the glass. The electrical properties for the model were obtained from the Material Library provided in ANSYS Electronics as follows:

- PEEK permittivity, $\varepsilon_r = 3.2$;
- Platinum electrodes permittivity, $\varepsilon_r = 1$, conductivity, $\sigma = 9.3$ MS/m; and
- Glass permittivity, $\varepsilon_r = 5.5$.

The cell constant was analysed as a function of distance between the tip and the bed surface. In addition, the sensitivity depth of the probe was analysed and calculated using the method presented by González-Correa et al. (1999).

6.2.4 Contact-force calibration and validation

The following set-up was prepared to characterize the contact force sensor. The probe was held vertically in a hollow pin vice that was attached to a vertical translation stage. The probe was then pushed down onto a weighing scale, wavelengths were recorded at 0 grams and 100 grams to calculate the change in wavelength per gram. After the calibration of the force sensor, the probe was pushed against the scale in increments of 0.01 mm until it reached around 70 grams and then was retracted in increments of 0.01 mm until it reached 0 grams. The data from the tip was acquired at 10 Hz while the acquisition frequency of the scale was fixed at 11.7 Hz.

Two additional experiments were performed to validate the contact force sensor using agar models which have similar elastic properties as soft tissue (Li et al., 2011): Firstly I used the same set up as for calibration, but in this case, different increments were used, and were applied more rapidly; secondly the probe was handled manually to give different peak intensities.

6.2.5 Temperature compensation

FBGs are inherently temperature dependent, and so to remove the temperature from the measurement of a different parameter, it is common to use two FBGs; one sensitive to both temperature and force, and the other to temperature alone. This was achieved by bonding the temperature and force sensitive FBG under tension to the PEEK sections of the probe and the temperature sensitive FBG to only one section of the PEEK probe so that it was not affected by force applied to the probe tip. Figure 6.1(a) shows a schematic of the functional components of the FBG sensing elements. The configuration was tested in an oven using a separate thermocouple (U1186A, Keysight Technologies, Santa Rosa, California, USA) to track the ambient temperature. The tip sensor was placed inside a

hollow plastic tube inside of an oven to reduce air currents and to provide a more uniform heating environment. The temperature was increased from 21 to 40℃ and data was recorded from both FBGs until the temperature measured on the thermocouple reached a steady state.

6.2.6 *Ex-vivo* assay

A segment of proximal colon from a guinea pig was used. The section was removed from the laboratory animal by methods approved by the Animal Welfare Committee of Flinders University (Animal Ethics Number: 845/12). All methods were performed in accordance with the relevant guidelines and regulations. The removed section of colon was placed into a beaker containing oxygenated Krebs solution immediately after excision (in mM: $NaCl$, 118; KCl, 4.7; NaH_2PO_4, 1.0; $NaHCO_3$, 25; $MgCl_2$, 1.2; *D- Glucose*, 11; $CaCl_2$, 2.5) and bubbled with 95% O_2/ 5% CO_2. The colonic segment was cleaned with Krebs solution. Then the segment was cut, opened and fixed with pins onto a tray with a hard silicone surface, Figure 6.3.

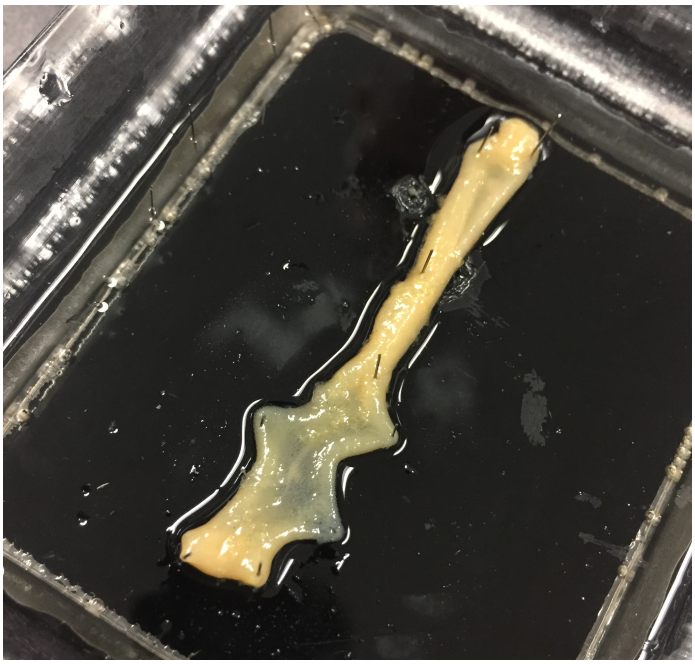

Figure 6.3: Pinned open proximal colon of a guinea pig used on the experiment.

The preparation was placed on the electronic weighing scale, see Figure 6.2. The probe was then lowered downwards onto the tissue while the system was recording the force from the weighing scale and from the tip, and the bioimpedance measurements. The sampling frequency for the force data was 10 Hz and 11.7 Hz for the tip and scale, respectively.

Twenty bioimpedance measurement at different frequencies in the frequency range of 5 kHz to 1 MHz were performed at a data acquisition rate of 1.5 Hz, which was the maximum sample frequency achievable by the system under these conditions.

6.3 Results

6.3.1 Impedance calibration

Figure 6.4 shows the impedance magnitude and phase angle of the probe for the spectral range 1 kHz to 1MHz. Saline solutions exhibit no dielectric dispersion at frequencies up to 1 MHz, so impedance magnitude and phase angle should be constant. From the results, it can be concluded that for conductivities similar to 0.150 M NaCl the error in phase is $< 4°$ and the relative error in magnitude is $< 0.9\%$ from 1 kHz to 1 MHz. Whereas for conductivities similar to 0.0150 M NaCl, the error in phase and the relative error in magnitude increased to 50° and 25%, respectively, due to the effect of the stray capacitances of the probe and BMS system. When the systematic error is not significant the scaling factor of the probe and BMS system is 53.8 m^{-1}. This cell constant value was calculated averaging the measured resistance values for the frequency range 1 kHz to 200 kHz and assuming that the resistivity of the 0.09% NaCl Agar-Agar model is 0.144 S/m. Mean and standard deviation of resistance for the interval were 373.61 Ω and 1.12 Ω, respectively.

The simulated cell constant was 78 m^{-1} for sample thickness larger than 3 mm. However, the cell constant was 6% and 19% larger if the distance between the probe surface and the glass surface were changed to 2 mm and 1.5 mm respectively. Nonetheless, ninety percent of the information of our probe comes from the region above a depth of 0.79 mm, see Figure 6.5. These results of depth penetration are similar to those by González-Correa et al. (1999); they reported that their probe had a depth of 0.77 mm.

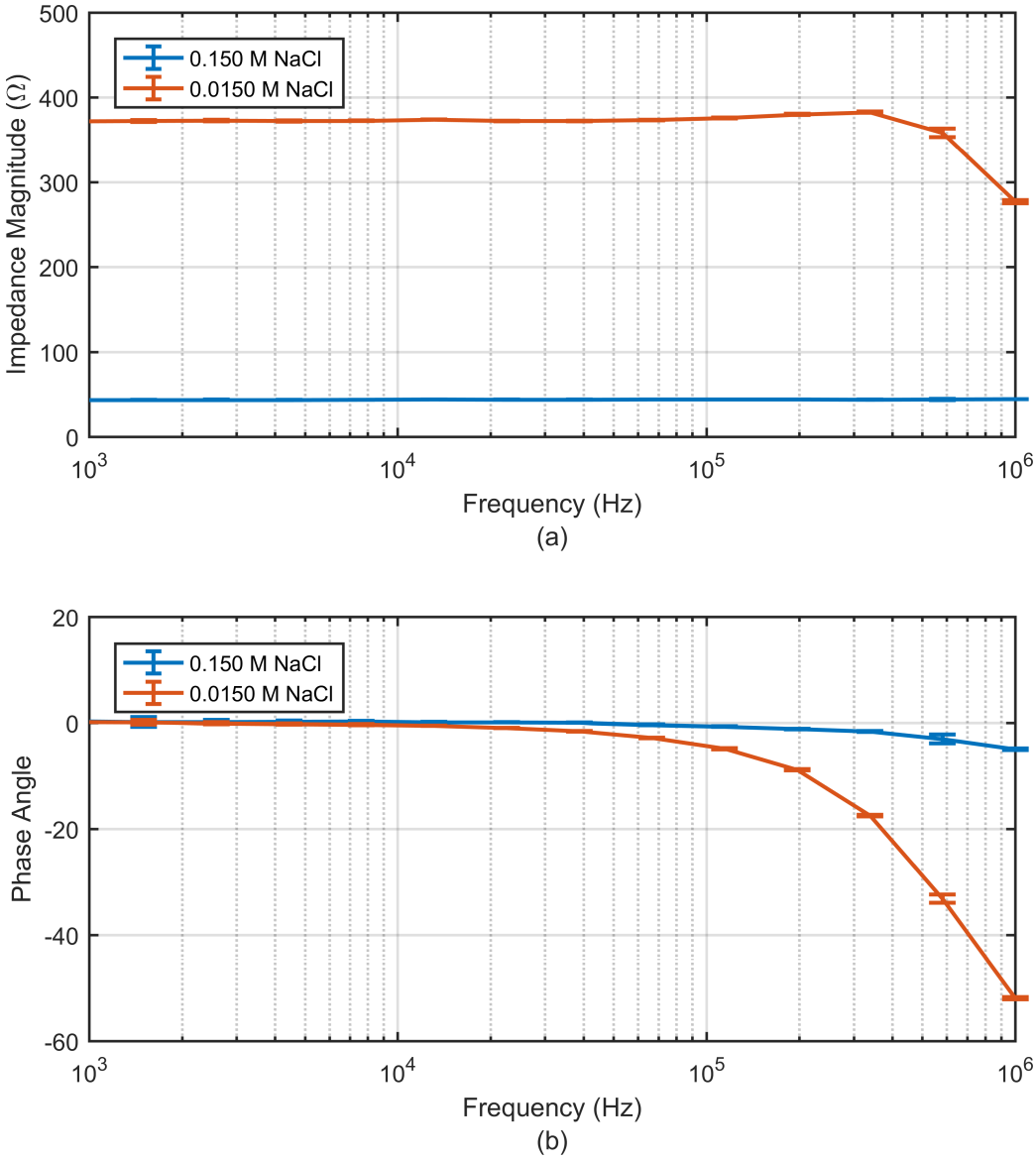

Figure 6.4: Impedance measurement of the Agar-Agar samples made from 0.15 M and 0.015 M NaCl: (a) impedance magnitude and (b) phase angle along the frequency range 1 kHz to 1 MHz.

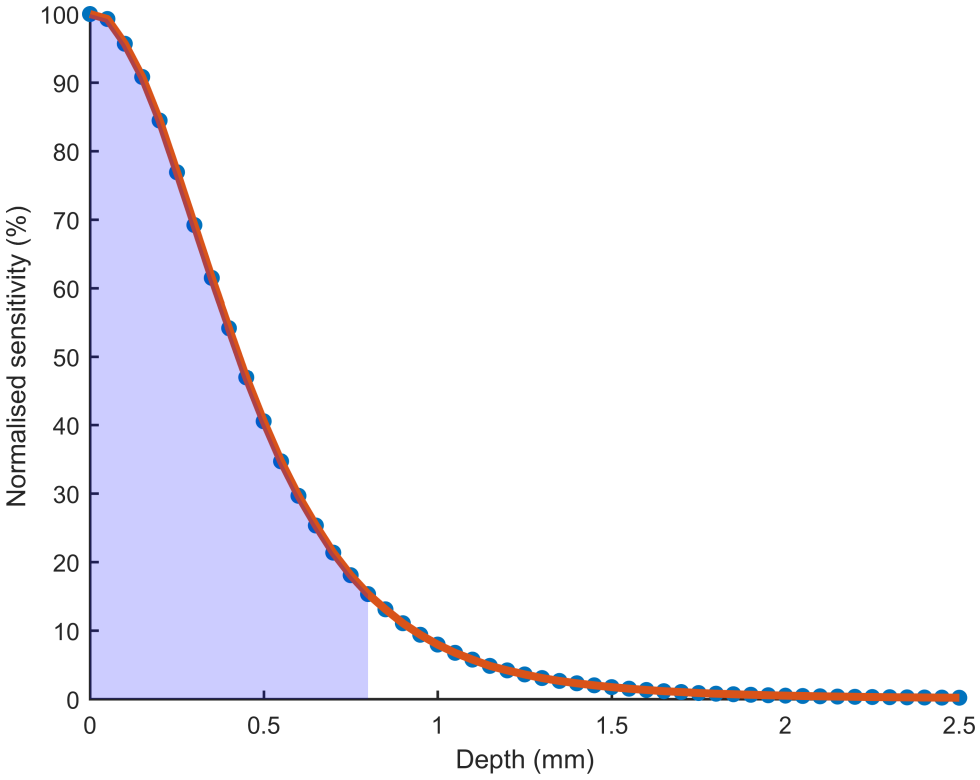

Figure 6.5: Normalised sensitivity as a function of depth. The shaded area indicates the 90^{th} percentile of the measurement and is confined to the region above a depth of 0.79 mm.

6.3.2 Contact-force calibration

The calibration factor determined from the change in wavelength between 0 and 100 grams load was -0.01 nm/g. Figure 6.6 shows the points measured during a test while adding force and then releasing it using the -0.01 nm/g calibration factor. A slight hysteresis was observed between loading and unloading of the force sensor with a maximum difference of 2 grams. For the purposes of this work, the sensor was assumed to be linear over the region of interest.

Figure 6.7 shows two graphs of two different recordings of the tip sensor on the Agar-Agar model. Figure 6.7(a) corresponds to the data obtained by loading the tip sensor with a micromanipulator whereas Figure 6.7(b) corresponds to manual loading. Small differences of 1 to 2 grams are observed between the tip sensor and the weight scale signals when the force is applied. The variable baseline offset seen in Figure 6.7(b) was likely due to the slight hysteresis in the response of the silicone returning to its initial state.

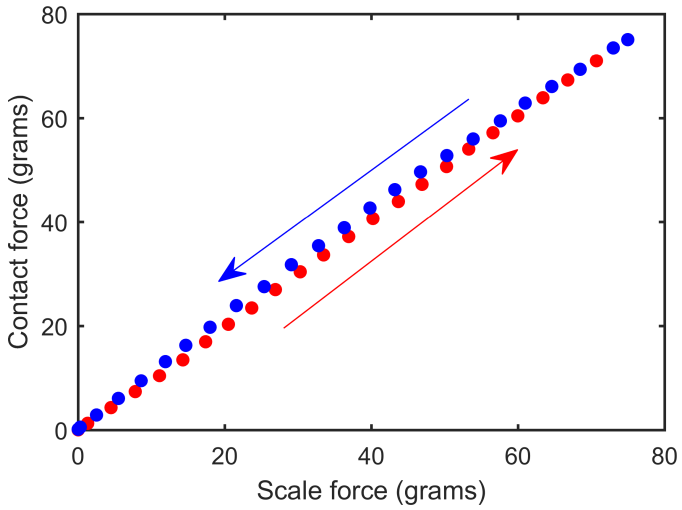

Figure 6.6: Points measured during a test while adding force and then realising it.

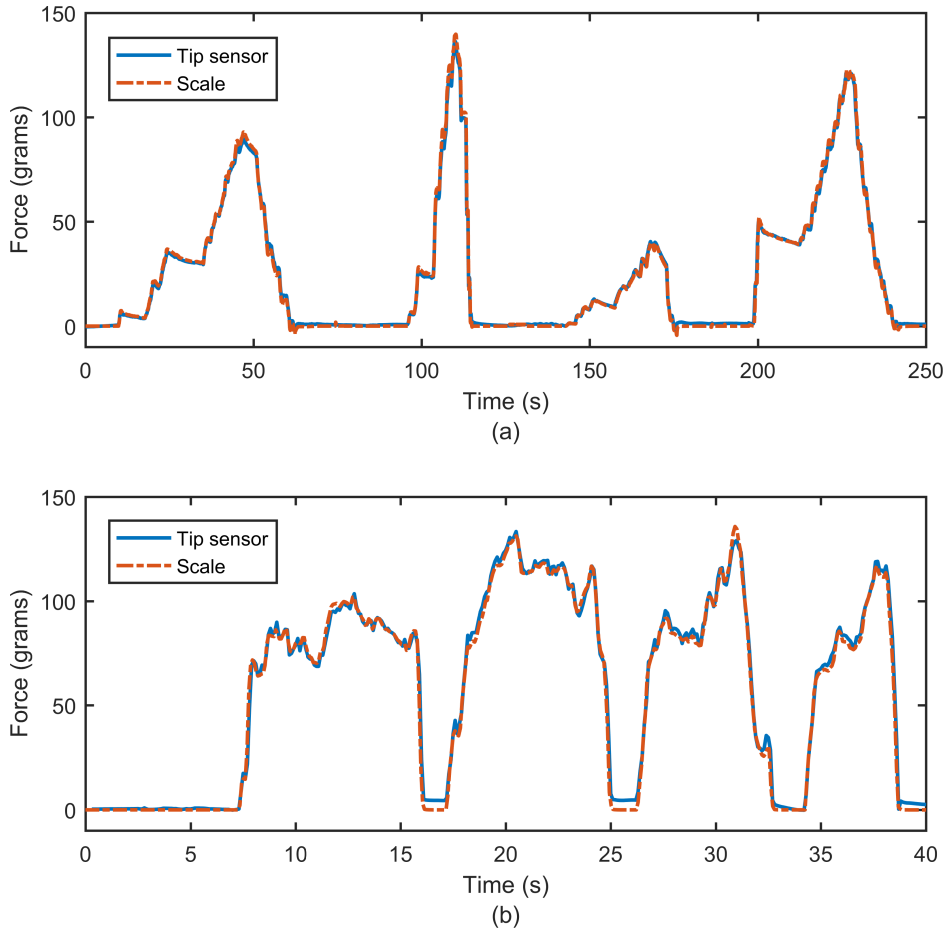

Figure 6.7: Force test done on an Agar-Agar model. (a) With a micromanipulator pushing downwards, and (b) handled manually.

6.3.3 Temperature compensation

Figure 6.8 displays the results obtained from the temperature compensation test. The graph on the left side shows the wavelength shift for the contact-force sensor fibre ($\delta\lambda_1$), the temperature sensor fibre ($\delta\lambda_2$), and the temperature profile measured from a thermocouple (accuracy $\pm$ 1.1℃ and temperature range -20 to 200℃) located next to the tip sensor. In general, the wavelength shift of an FBG is dependent on both temperature and strain (see Equation A.16), however, the design of the probe tip ensures that wavelength of FBG 1 is susceptible to temperature and strain whereas FBG 2 is only susceptible to temperature. The differential wavelength shifts between FBG 1 and FBG 2 seen in Figure 6.8 is due to the strain induced from the thermal expansion of the package (ε_{pk}), see Figure 6.8(a).

It is worth noticing, that there is a delay on the heat transfer to the fibre. The thermocouple reacted to the change in temperature before the contact-force sensor due to the thermal insulation of the tip sensor packaging.

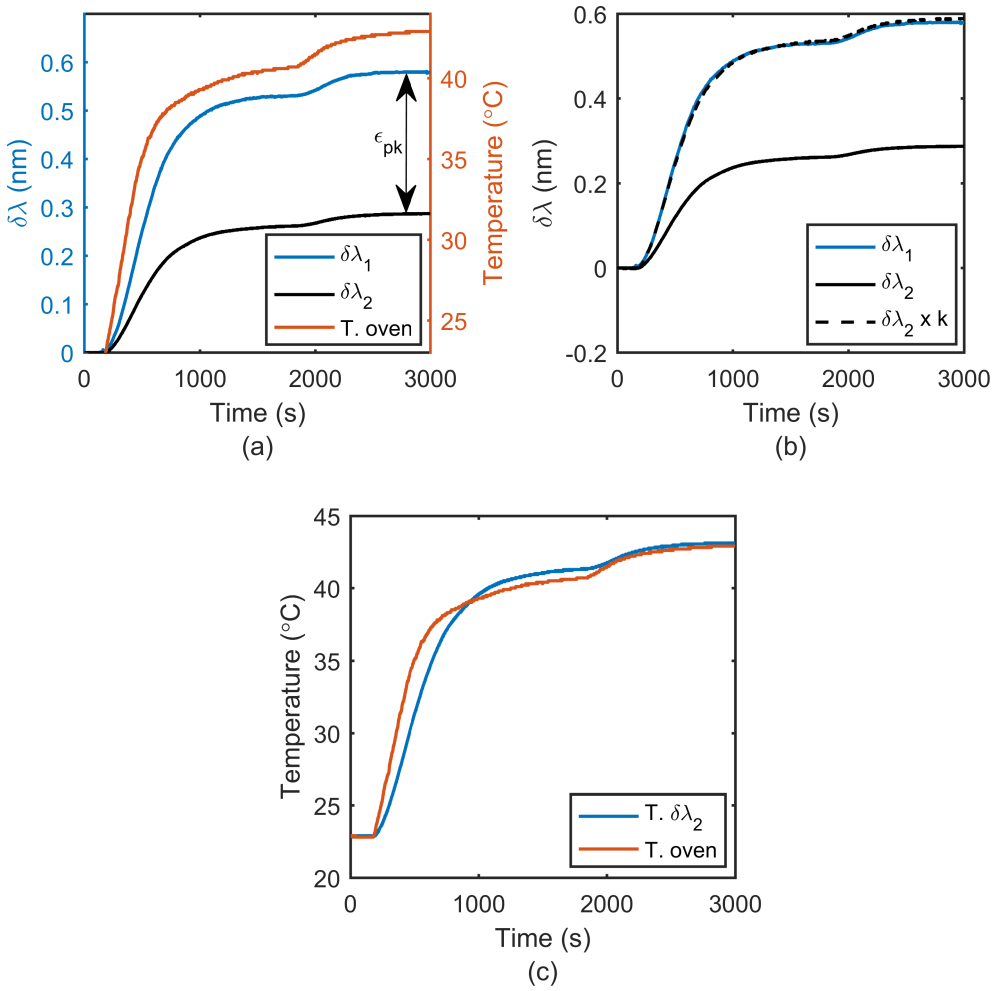

Figure 6.8: Temperature compensation: (a) Wavelength shift for the force sensor FBG 1 ($\delta\lambda_1$) and temperature sensor FBG 2 ($\delta\lambda_2$), and the temperature profile during the experiment. (b) Wavelength shift ($\delta\lambda_1$) and ($\delta\lambda_2$), and a comparison of the wavelength shift after a correction factor, k, has been applied to $\delta\lambda_2$. (c) Temperature increment from the thermocouple and the reference grating ($\delta\lambda_2$).

Figure 6.8(b) shows the wavelength shift of both FBG 1 and 2 ($\delta\lambda_1$ and $\delta\lambda_2$) and compares the wavelength shift of FBG 1 with wavelength shift of FBG 2 multiplied by a constant, k. The k is the ratio of wavelength shift of fibre 1 and 2 ($k = 2.038$) when both fibres reach steady state at a specific temperature and there is zero mechanical strain. The difference between $\delta\lambda_1$ and $\delta\lambda_2$ multiplied by the k factor due to temperature effect is very small. The k factor was measured multiple times 2.050, 2.034 and 2.017 before and after the experiment (mean = 2.036 and std = 0.012).

Figure 6.8(c) compares the temperature from the thermocouple and the temperature from the reference grating obtained from Equation A.16. The difference in temperature between thermocouple and reference grating was less than 1℃ degree for steady state.

6.3.4 *Ex-vivo* assay

The results of the *ex-vivo* experiment are presented in Figure 6.9. Figure 6.9(a) shows the force measured using the fibre optic force sensor, and the contact pressure values (derived from the measured force divided by the surface of the distal tip of the probe; 8.0425 mm^2) shown in Figure 6.9(b). Points were selected in order to overcome the mismatch of sample frequencies of pressure and impedance, making sure that at least the three previous pressure points of the selected resistivity points varied by less than 1 gram.

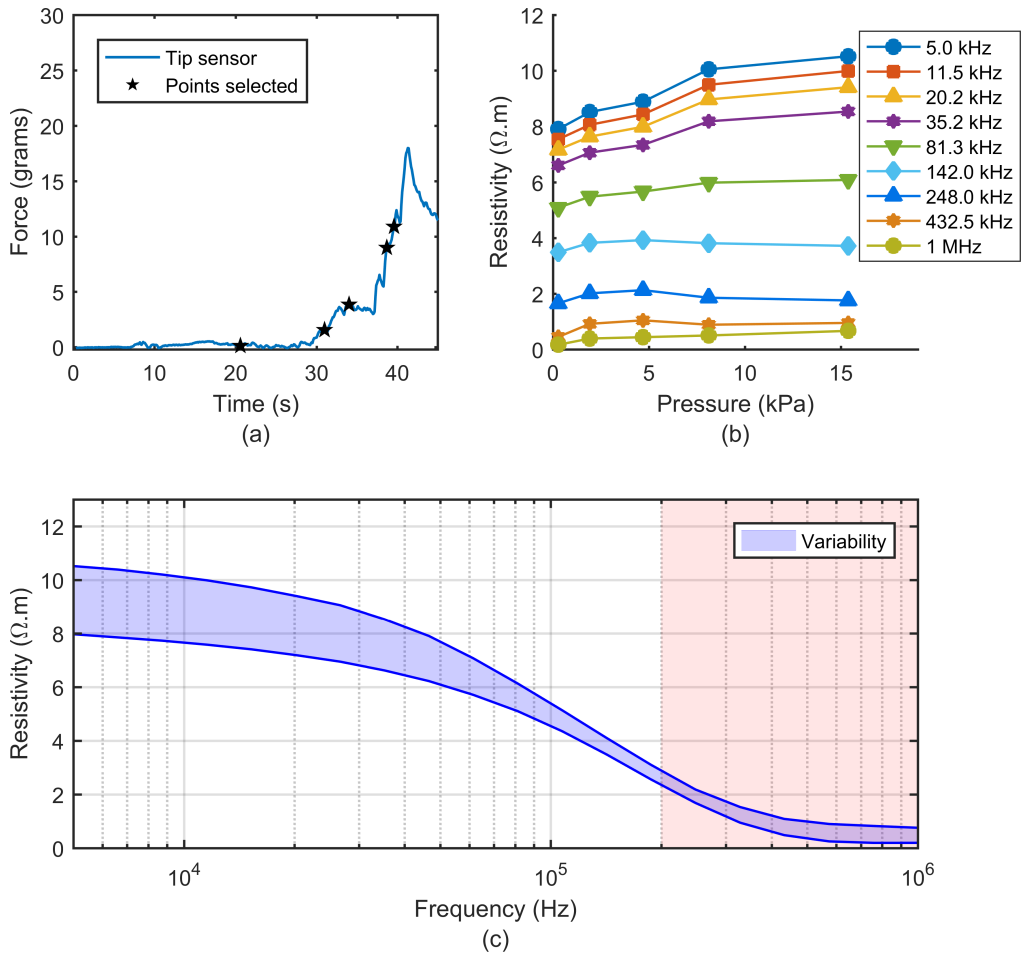

Figure 6.9: Results of the *ex-vivo* experiment: (a) Force values in grams obtained during a recording. The stared points in (a) are the points selected for representing the changes in impedance versus contact pressure. (b) Resistivity values in the frequency range of 5 kHz to 1 MHz at different pressures. (c) Variability of resistivity measurements along the frequency range 5 kHz to 1 MHz during the measurement shown in (a), note that the shaded area from 200 kHz to 1 MHz indicates at which frequency data is unreliable according to the validation presented above.

Figure 6.9(b) compares the resistivity values obtained by dividing the real part of the impedance by the cell constant, K, at the different contact pressure points indicated in Figure 6.9(a) (0.28, 1.92, 4.7, 8.12 and 15.38 kPa) for frequencies of 5, 11.5, 20.2, 35.2, 81.3, 142, 248, 432.5 kHz and 1 MHz. However, only frequencies from 5 to 142 kHz were considered since they are within the viable frequency range of the BMS and are close to the frequencies used in a study performed by González-Correa et al. (2005). The resistivity readings, shown in Figure 6.9(b), increased considerably with contact pressure for the frequency range of 5 kHz to 81.3 kHz, whereas at 142 kHz the change was much less significant. Figure 6.9(c) shows the variability of resistivity measurements along the full frequency range during the measurement for the full pressure range (0 to 15.38 kPa). The shaded area indicates the frequencies ($>$ 200 kHz) at which the data become unreliable according to the validation performed with the 0.09% NaCl sample (see Section impedance calibration above). As seen before in Figure 6.9(b) a large increase in resistivity can be seen at low frequencies, whereas at high frequencies ($\sim$ 100 kHz) the increase in resistivity decreases.

6.4 Discussion and conclusions

According to the *in-vitro* assays performed here, the developed system should be capable of measuring the impedance of soft living tissues with an error in magnitude of less 0.9% and an error in phase of less 4° degree in the frequency range from 1 kHz to 1 MHz for conductivities of 1.44 S/m. Parasitic capacitances, which are a source of systematic errors causing a decrease in the measured modulus of the impedance, become significant at high frequencies ($>$ 200 kHz) for tissue conductivities of 0.144 S/m, because it is at high frequencies when the displacement currents through capacitances are relevant. It is more noticeable for the highest resistivity because those parasitic paths to stray current (instead of going through the sample) become more "preferable" as the impedance of the sample increase. The frequency range is consistent with the frequency range found in similar studies using four-electrode setups (González-Correa et al., 2005). The lower limit of the frequency range is imposed by the sample rate of the BMS needed to keep up with the sample rate of the fibre optic sensors; the upper limit is mostly imposed by the stray capacitances of the wires within the probe, and to a lesser degree in the bioimpedance measurement system.

The difference between the simulated and the experimental cell constant might be attributed to engineering tolerances in the electrode positioning. Inspection under a microscope showed errors of about 250 µm in the fabricated tip. Simulations with such errors

were performed, in which cell constant varied from about 50 m^{-1} to about 100 m^{-1} which suggests this hypothesis is valid.

The FBG sensors provided a useful method to assess the contact force and temperature during the bioimpedance measurements. The contact-force sensor was compared with data recorded by an electronic scale. Maximum differences of 1 to 2 grams were observed during the assays.

The temperature test showed that multiplying the reference grating by a constant factor can compensate the temperature effect on the grating under strain. The standard deviation of the k factor ($\pm$ 0.012) could induce an error of less than 1 gram, so would not affect significantly the measurements; however, the k factor may change over time due to degradation of silicone and further long-term studies would be needed to confirm this. Furthermore, the temperature change from the thermocouple and the fibre are similar, albeit with a slight lag in response of the fibre due to the insulating properties of the tip sensor packaging. This could be improved by increasing the thermal conductivity of the package. The delay in thermalisation was of the order of 120 s and so should not affect *in-vivo* measurement to any great degree as body temperature is nominally constant and measurements would take longer than this to set up and acquire data. Care may be needed however if irrigation fluid is used as part of an endoscopic procedure.

In this instance, in the *ex-vivo* assay results, the maximum change in resistivity due to variations in applied contact pressure was 33% over the range 0 to 15.38 kPa at 5 kHz. The increase in resistivity was found to reduce at higher frequencies being a minimum of 6.6% for at 142 kHz. This increase in apparent resistivity may be explained by the fact that the tissue sample under test gets compressed resulting in both a thickness reduction, which increases the cell constant, and an increase in tissue pressure which causes extracellular fluid migration and an actual increase in tissue resistivity as explained by Zhou et al. (2016).

During the experiment, we observed that the thickness of the sample always appeared to be above 2 mm (not measured). This implies that, according to the simulation results, the maximum increase in impedance we would observe due to a decrease in the sample of 3 to 2 mm would be in the order of 6%. Therefore, the 33% increase in impedance must be mostly attributed to an actual increase in the resistivity of the tissue rather than the proximity of the lower surface.

The above observations highlight the need to control contact pressure to make sure the variability is as small as possible at low frequencies.

The impact of contact force on the bioimpedance measurements is lower when impedance is measured at a sufficiently high frequency, as it can be seen in Figure 6.9(c). This can be explained by the fact that the current at high frequencies passes through extracellular and intracellular liquid, and cell membranes (Pethig and Kell, 1987). Intracellular liquid is constrained by the cells when a low mechanical compression is applied, unlike the extracellular liquid that is rapidly pushed aside (Zhou et al., 2016). Therefore, the variability is reduced at high frequencies due to the constrained nature of intracellular liquid and the current's path at high frequencies.

The resistivity results are consistent with resistivity values obtained in sections of rabbit colon done by Mulett-Vásquez et al. (2016) where resistivity values at 19.2 kHz were within the range of 8.7 to 6.6 Ω.m from proximal to distal colon, respectively. Also, these results qualitatively agree with the ones obtained by Gonzalez et al on columnar gastric tissue of rats (González-Correa et al., 2005). Although, the resistivity values of the colon are slightly larger than those for the columnar gastric tissue and much lower than those for the squamous epithelium, these discrepancies can be attributed to both the difference in animal tissue and the difference in structure between gastric columnar and colonic columnar epithelium, which contains more glands surrounded by a vast array of secretory and goblet cells than gastric columnar epithelium.

Reporting the resistivity values alone cannot provide details of structural changes or ischemic damage. However, in this instance, data were reported as the real part of impedance only (resistivity) for the sake of simplicity and to be in accordance with previous published data. Other parameters, that can be obtained from the data set – such as phase angle, Cole parameters (α, τ_Z, R_∞ and R_0) and/or distribution of relaxation times (DRT), can provide further information on tissue condition (Ramírez-Chavarría et al., 2018; Rigaud et al., 1995; Zou and Guo, 2003). We have specifically focused on variations in resistivity, in the knowledge that more complex data will also be more consistent if the contact pressure is controlled.

This study set out to develop and evaluate a new medical device for measuring the contact-force applied during bioimpedance measurements on biological samples up to 1 MHz; however, our results indicate that stray capacitances limit the device performance above 200 kHz. The device will allow us to perform a more detail study on the data variability due to the contact pressure effect on the bioimpedance measurements. Its small dimensions make it suitable for endoscopic and colonoscopic procedures.

Chapter 7

Standardising bioimpedance measurements based on electrode contact pressure

Part of the work presented in this chapter is the subject of the following refereed conference paper:

Ruiz-Vargas A, Ivorra, A, Arkwright, JW. Monitoring the effect of contact pressure on bioimpedance measurements. In: *2018 40th Annual International Conference of the IEEE Engineering in Medicine and Biology Society (EMBC)*. IEEE; 2018:4949-4952. doi:10.1109/IECBES.2016.7843433.

7.1 Introduction

This work is a continuation of **Chapter 6** and presents a preliminary investigation into the effect of large exerted contact pressure and address the variability on bioimpedance measurements (**Aim 5**). To do that, a generalised linear contact pressure compensation method was developed with a set of bioimpedance measurements on five segments of resected human colon. This initial approach did not show the expected reduction of variability, and so an alternative method based on data derived from each individual measurement is presented. This chapter presents the results of the initial compensation method and also the suggested method that promises to reduce the variability and add extra information about tissue state.

7.2 Materials and methods

7.2.1 Equipment, probe and calibration

The equipment and pencil probe use for these experiments are the same ones presented in Chapter 6.

The calibration process for the impedance sensor and contact pressure were the same as in Chapter 6. Only this time sodium chloride solution with a concentration of 0.09% (conductivity, $\sigma = 0.144\,S/m$) was used to calculate the cell constant at 9.6 kHz. These calibrations (impedance and pressure) were carried out at the beginning of each experiment as these were performed at different times.

7.2.2 Experiment protocol

Five sections of a human distal colon, each 1.5 cm in length, were obtained from larger sections resected surgically to remove malignancies and/or diseases. Methods were approved by Southern Adelaide Clinical Human Research Ethics Committee (ethics approval no. 50.07), and all patients provided written informed consent prior to their involvement. Within 4 hours following surgery the segment was placed onto a plastic tray (Figure 7.1(a)); cleaned, cut, opened and fixed with pins onto the tray. Note that some specimens took longer to get in the laboratory than others due to the surgical procedure.

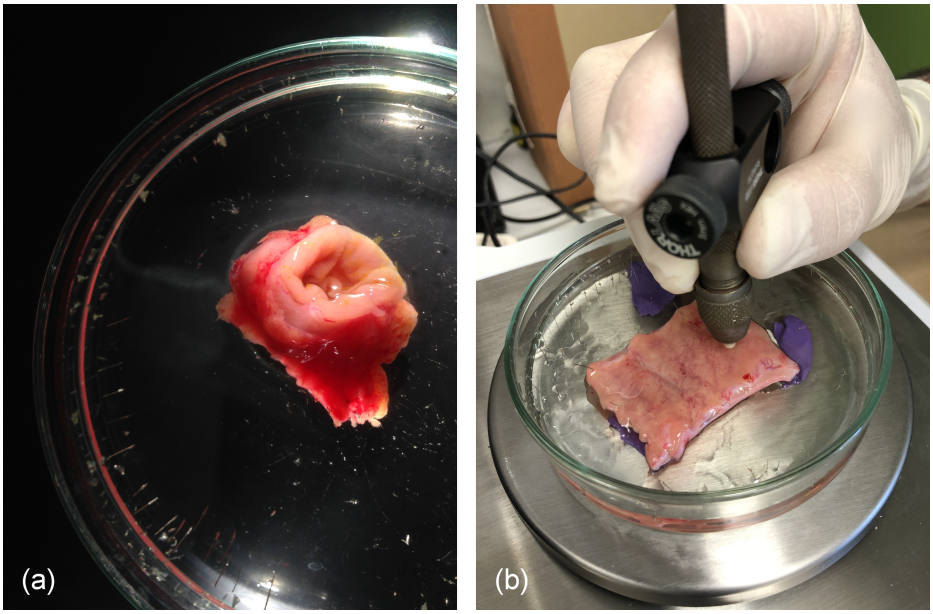

Figure 7.1: (a) Resected specimen before preparation. (b) During a measurement of the resected specimen after preparation.

The probe (held in the hollow vice pin) was then pushed manually onto the tissue while the system was recording the contact pressure and the bioimpedance measurements (See Figure 7.1(b)). Each user took measurements at one location repeatedly (3 times each point). In the first two trials, the exerted contact force was incrementally increased, trying not to exceed a contact pressure of 20 kPa. In the third trial, the exerted contact force was increased considerably to exceed 20 kPa. Between trials, the probe was lifted off the tissue for about 5 – 10 seconds to allow the tissue to recover, and then next trial was made. Selection of measurement location on the specimen for each user was sufficiently far apart to avoid any memory effects from previous measurements. The time difference between users' measurements was less than 5 minutes. In some instances, a drop of mucus was observed on the tip of the probe which was removed using a lint-free tissue.

Bioimpedance measurements were performed at a measuring frequency of 9.6 kHz and at a data acquisition rate of 10 Hz; the contact force was acquired simultaneously at 10 Hz. The measuring frequency was chosen based on previous experiments performed by Gonzalez-Correa et al. (2003), as it was found that pathological changes are better picked up at low frequencies.

7.2.3 Statistical analysis

To evaluate the variability of contact pressure, resistivity data (from the three trials) were categorized into four pressure groups: group 1 (< 5 kPa), group 2 (5 – 10 kPa), group 3 (10 – 20 kPa), and group 4 (> 20 kPa). A linear mixed model (LMM) was used to control for nesting the measurements under specimen with a factor of user (2 levels) and a factor of pressure (4 levels) entered as fixed factors; to compare the bioimpedance measurements among the pressure groups. Statistical analyses were carried out using SPSS Statistics, version 23 (IBM Corp., Armonk, NY, USA).

7.2.4 Generalised linear compensation method

The generalised linear contact pressure compensation method consists of applying a coefficient, k, to the measured resistivity at a given pressure in order to convert it to that at a given reference pressure. The corrected resistivity is then given by Equation 7.1:

$$R_{reported} = k \times R_{measured} \tag{7.1}$$

Where $R_{reported}$ is the compensated resistivity value at a given reference pressure, $R_{measured}$ is the resistivity value measured at a specific pressure. The coefficient, k, is the ratio (Equation 7.2) between the resistivity at a chosen reference pressure, $r_{(P_{reference})}$, and the resistivity at a given measured frequency, $r_{(P_{measured})}$, calculated from the generalised linear curve fit (Equation 7.3), obtained previously from data set of different specimens from the same anatomical region (see Figure 7.2).

$$k = \frac{r_{(P_{reference})}}{r_{(P_{measured})}} \tag{7.2}$$

$$r_{(P)} = m \cdot P + r_0 \tag{7.3}$$

Where, the parameters, 'm' and 'r_0', are the gradient and the extrapolated resistivity value at 'zero contact pressure' for the data set from different specimens, and P is the pressure. Similar methods are used to compensate the effect of temperature on conductivity measurements in saline solution (Grimnes and Martinsen, 2008).

For example, if a resistivity value was obtained at a pressure of 2.5 kPa, and we wanted

to report for standard pressure (5 kPa). The equation, then, will be:

$$R_{reported} = \frac{r_{(5kPa)}}{r_{(2.5kPa)}} \times R_{measured} \tag{7.4}$$

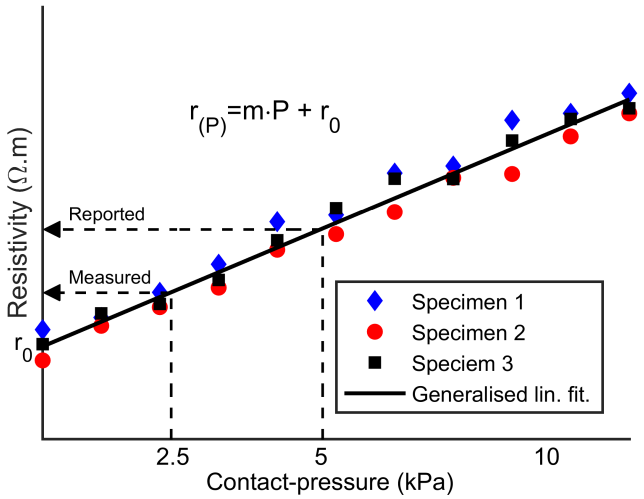

Figure 7.2: Example of contact-pressure compensation. The coefficient, k, is calculated based on the linear curve fitting in which is then applied to convert the resistivity measured at a specific contact-pressure to that at the reference contact-pressure (5 kPa). Simulated data points.

The reference contact pressure used in the generalised linear compensation method was 0 kPa. Two data points from each user (one from each trial) per specimen were chosen to apply the compensated method. Points were selected around 5 kPa and 15 kPa as contact pressure above 20 kPa were considered to be excessive by the users.

7.2.5 Numerical study of mucus thickness

As mentioned above, sometimes during the experiments different quantities of mucus were observed on the specimens and underneath the probe. For that reason, a simulation was performed in ANSYS Maxwell (ANSYS Electronics Desktop, ANSYS Inc, Canonsburg, Pennsylvania, USA) to model and quantify the effect of mucus thickness on our measurements. Figure 7.3 shows the model used to perform such simulation. The model consisted of a lower surface made out of glass (thickness = 1 mm), a human colon segment (thickness = 4 mm), and a mucus layer (thickness variable from 0 to 200 µm). The probe had the same dimensions as in the experimental set-up, and was placed in the middle of the model

above the mucus layer.

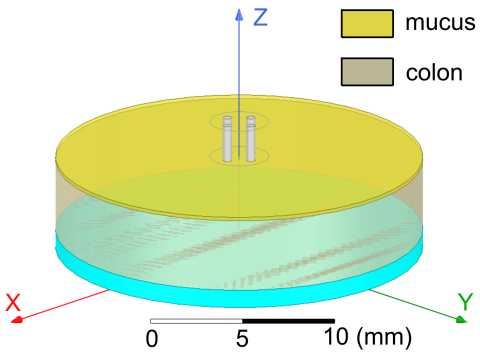

Figure 7.3: Schematic of the 3D simulation performed in ANSYS Maxwell.

The electrical properties for the probe case (plastic: $\varepsilon_r = 3.2$), electrodes (platinum: $\varepsilon_r = 1$, $\sigma = 9.3\,MS/m$) and glass surface (glass: $\varepsilon_r = 5.5$) were obtained from the Material Library provided in ANSYS Electronics. The electrical properties for the human colon ($\varepsilon_r = 14230$, $\sigma = 0.24\,S/m$ at 9.6 kHz) and mucus ($\varepsilon_r = 72$, $\sigma = 1.1\,S/m$ at 9.6 kHz) were obtained from (Gabriel, Lau and Gabriel, 1996*b*; Walker et al., 2002), respectively.

7.3 Results

7.3.1 *Ex-vivo* studies

Figure 7.4 shows a scatter plot of the resistivity data against pressure for all measurements made by both users. A Pearson's correlation test was performed on the combined data set from both users to determine the linear relationship between resistivity and pressure, giving a Pearson's Correlation Coefficient equal to 0.79.

Results from the statistical analysis are presented in Figure 7.5 in combination with mean and standard deviation values of resistivity for each contact pressure group. Resistivity was different for all pressure groups with a $p < 0.001$, except between group 1 (< 5 kPa) and group 2 (5-10 kPa) that had a p-value of 0.002 with a mean difference 0.318 Ω.m. A clear relationship can be seen be between resistivity and contact pressure.

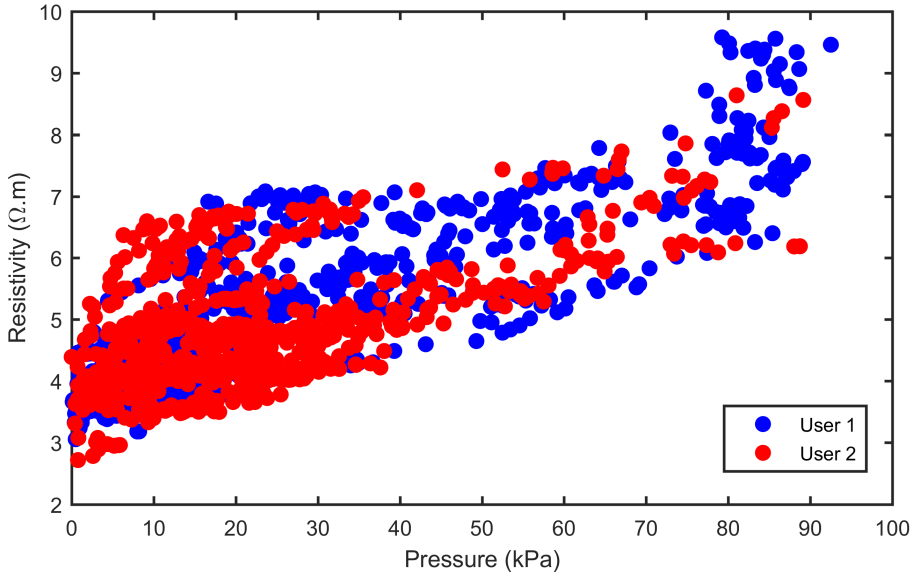

Figure 7.4: Scatter plot of all combined contact pressure and resistivity for each user.

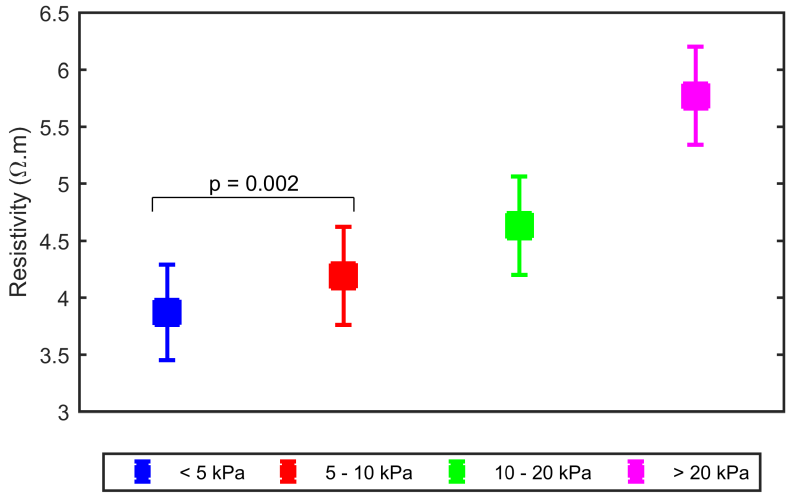

Figure 7.5: Results from the comparison between groups of contact pressure with combined data from both users. P-values were lower than *0.001* between all the groups, except between group 1 and 2 (as stated).

Effects of excessive contact pressure

Figure 7.6 shows the effect of exerting large contact pressure on bioimpedance measurements during the third trial. In this instance, an extra trial was made after the third trial to see the effect of large exerted pressure. As expected, large contact pressures did alter

the tissue, increasing resistivity values by approximately 1 Ω.m. This is believed to be due to migration of extracellular fluid away from the point of contact and possible due to rupture of the cells beneath the probe tip.

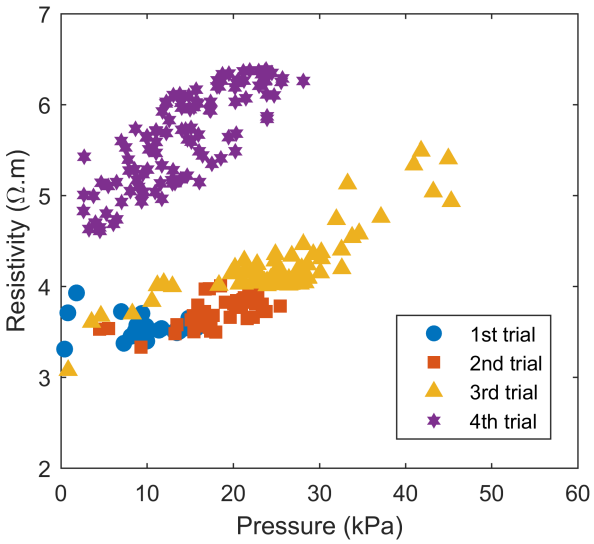

Figure 7.6: Effect of large exerted contact pressure. X-axis represent the contact pressure exerted during resistivity measurements shown in Y-axis.

7.3.2 Generalised linear compensation

Looking at Figure 7.4 and the trend observed in Figure 7.5, it makes sense to apply a generalised linear compensation method. To do this, only the data from the first two trials were considered towards calculating the generalised linear fitting, since during the third trial a large amount of contact pressure was exerted that compromised the tissue making the values recorded during the 4^{th} trial significantly different. The generalised linear fitted equation for the compensation method was the following:

$$r_{(P)} = 0.0678 \cdot P + 3.6178 \tag{7.5}$$

Where $r_{(P)}$ is the pressure dependent resistivity.

Figure 7.7(a) shows selected points from each user, and Figure 7.7(b) shows the compensated data points from the selected points using Equation 7.1. Observing the results, the correction applied some compensation to the data which improved the spread in results between 3 and 4 Ω.m, and reduced the difference between trials and users (e.g. user 1 for specimens 3 and 5, and user 2 for specimen 4), but for other cases, applying the correction

actually increased the difference between samples (e.g. user 1 for specimens 1 and 4).

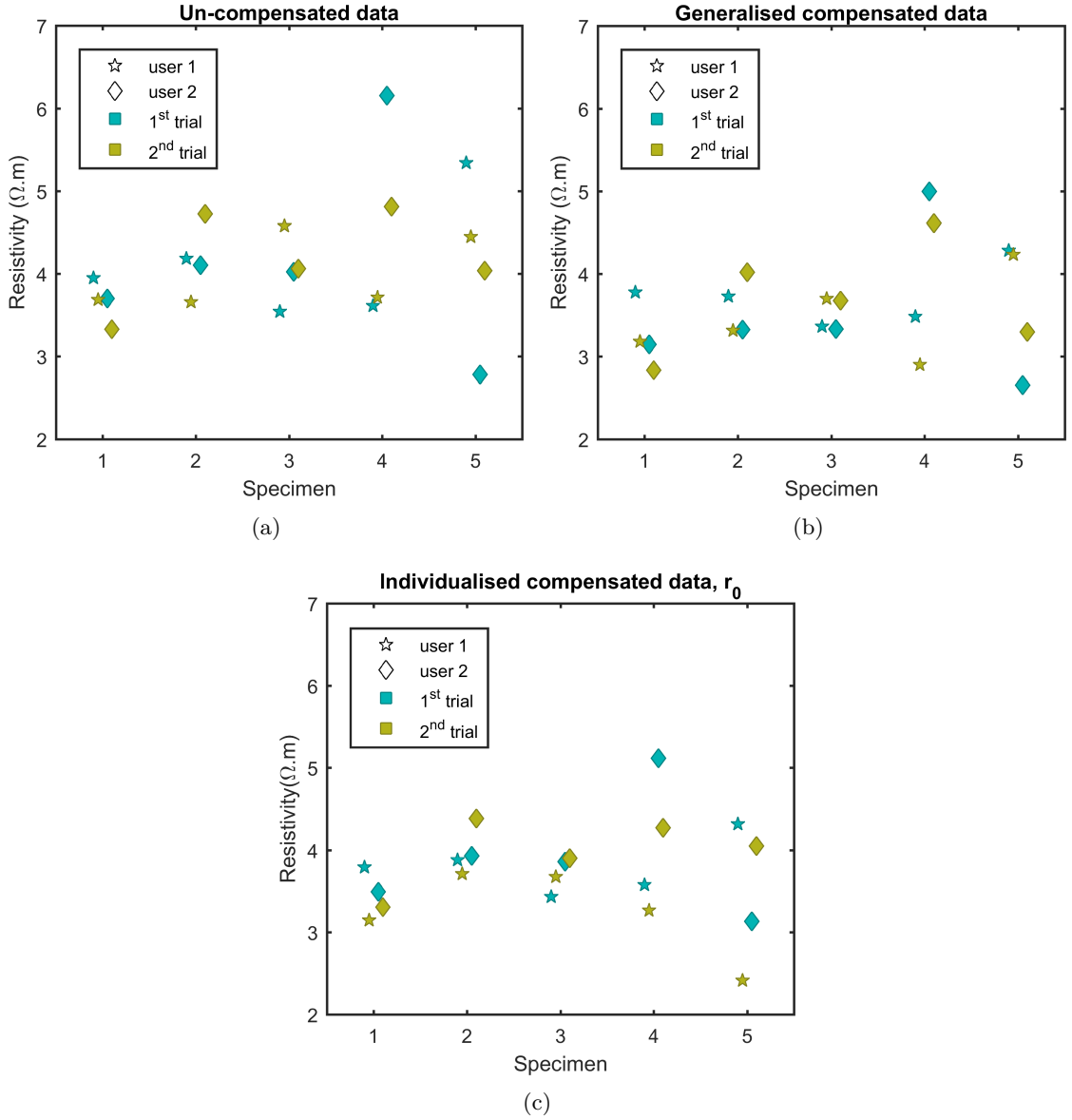

Figure 7.7: Two (a) un-compensated and (b) generalised compensated data points (extrapolated to 0 kPa, r_0) for each user and specimen. (c) Extrapolated values, r_0, obtained from the individualised compensation method. Stared points belong to user 1 and diamond points belong to user 2. Grey and green colours correspond to the first and second trial respectively.

This increase in difference seen between some samples after applying the general method is explained by the fact that some measurement sites had a different gradient compared to that calculated from all the data sets. The variation in corrected resistivity data and the effect of excessive pressure indicates that applying all previously acquired data may not be

the best approach. Hence a second approach based on individualised linear compensation of the data recorded during each trial was proposed. This modified method is presented in the following sub-section.

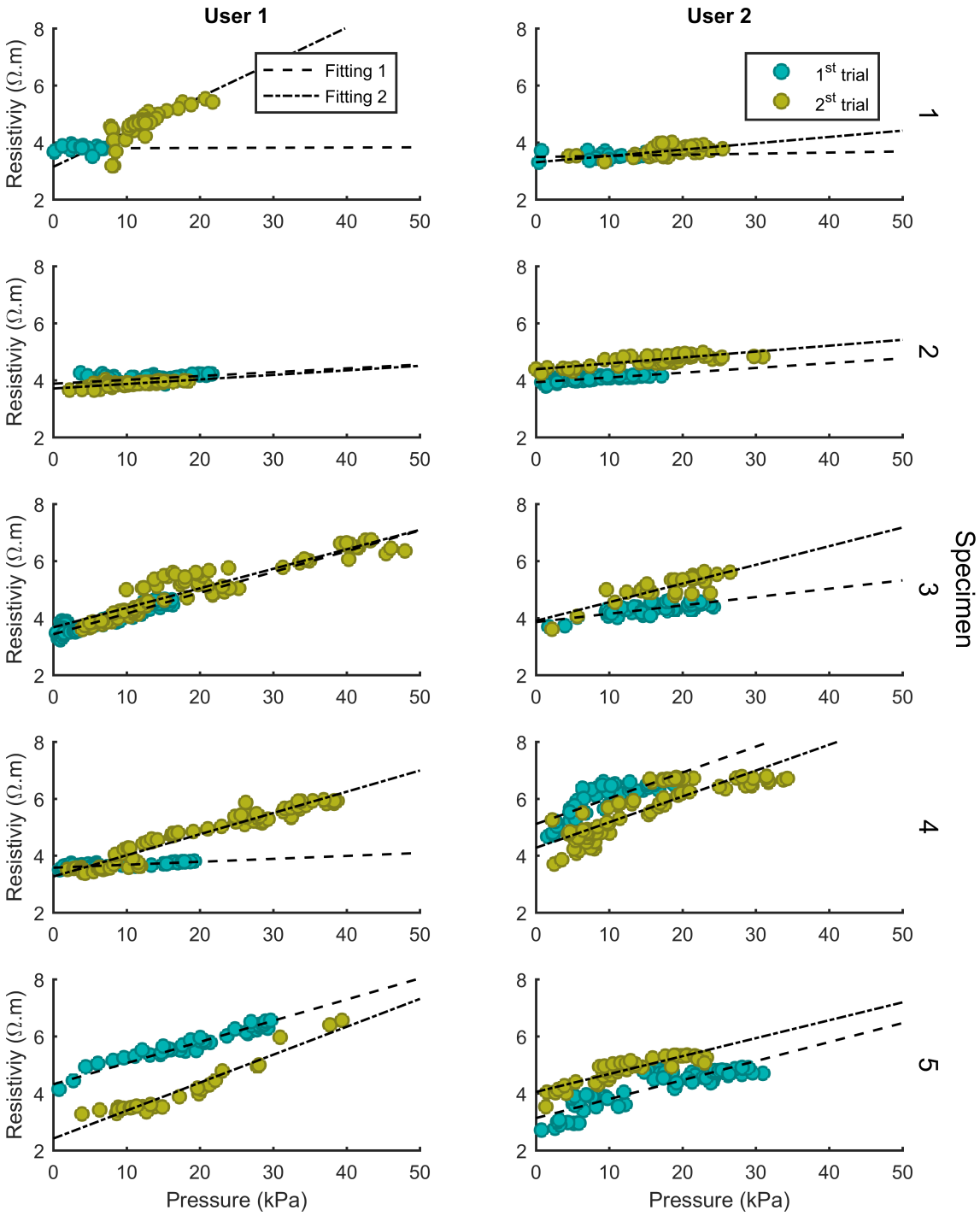

Figure 7.8: Plot of different data points for each user, specimen and trial. Individual linear fitting curves for first and second trial are represented in dash and dash-point lines, respectively. Grey and green colours correspond to the first and second trial respectively.

7.3.3 Individualised linear compensation

The individual data for each user, trial and specimen are shown in Figure 7.8 in conjunction with the individualised linear fittings. It can be seen how these are different in some instances. Reporting individualised linear fittings is possible due to the number of samples taken at different pressures during each trial. The extrapolated parameters, r_0, are represented in Figure 7.7(c), showing that the parameter values improve slightly with respect to the generalised method, although in some instances more difference between samples can again be seen (e.g. specimen 5). In general, the different resistivity values converge between 3 and 4 Ω.m.

The gradients for each user and each trial are represented in Figure 7.9. Looking at Figure 9, what stands out from the gradients is the dominance of two regions from 0 to 0.03 Ω.m/kPa and 0.06 to 0.1 Ω.m/kPa, possibly indicating variations in sub-surface morphology or tissue damage. There is also a noticeable trend in the gradients of the first and second trial. If the gradient of first trial is in the lower region, the second can be in either the first region with almost no variation (specimens 1 and 2) or in the upper region with a higher gradient. Whereas if the gradient of the first trial is in the upper region, the gradient of the second trial is always in the same upper region.

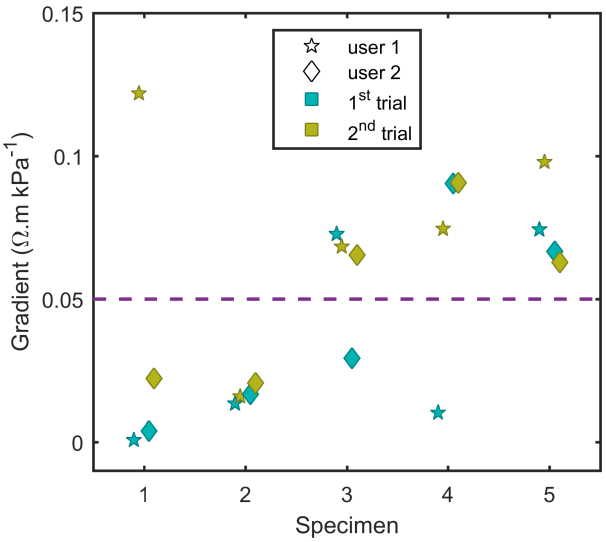

Figure 7.9: Parameters m for the suggested method. Stared points belong to user 1 and diamond points belong to user 2. Grey and green colours correspond to the first and second trial respectively.

7.3.4 Numerical study of mucus thickness

Results from the *in-silico* study to investigate the effect of mucus thickness on bioimpedance measurements are presented in Figure 7.10. A clear linear relationship can be seen between mucus thickness and change in resistivity. A mucus layer of 200 µm could lead to a change in measurement of 33% (i.e. if the nominal resistivity value without mucus was 4.17 Ω.m, the read value would be 2.79 Ω.m).

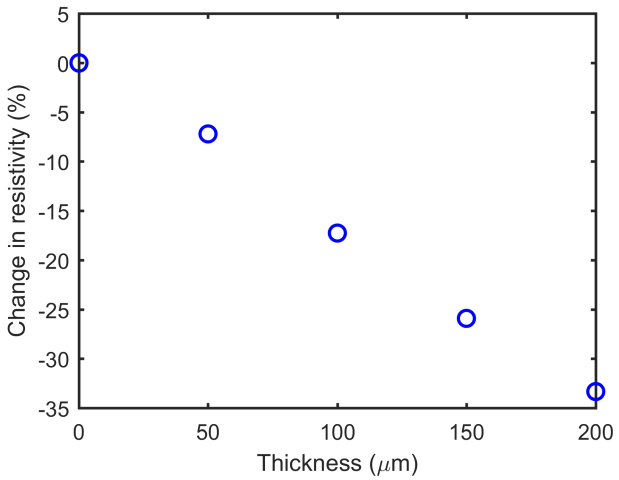

Figure 7.10: Simulated resistivity of a sample with different thin layer of mucus. X-axis represents the thickness of the mucus layer in µm, and Y-axis the change in the simulated resistivity in percentage.

7.4 Discussion

A set of experiments were performed on five segments of resected human colon to study the effect of contact pressure on bioimpedance measurements. The data were then used to propose a generalised linear pressure compensation method, which showed a reduction on variability of the measurements. However, in some instances, the method not only failed to reduce the variability but in fact increased it. The increase in difference between samples when the general method is applied is explained by the fact that applying this compensation method on bioimpedance measurements, we are assuming that all the samples under test have same resistivity contact pressure gradient.

It can be seen in Figures 7.8 and 7.9 that this is not the case, contact-pressure does not have the same effect on all the measurement sites, and in some instances the gradient changes after performing a first measurement. We hypothesized that the change in gradient may

be attributed to: 1) heterogeneities of living tissues, 2) sites, that are far from capillaries and/or vessels that provide nutrients, might suffer of cell death sooner than other sites, and 3) morphological changes induced after performing a first set of measurements.

Looking at Figure 7.7, it could be deduced that the individualised suggested method might not add any improvement to the general method, but Figure 7.11 showed that, overall, further improvement was achieved by the individualised proposed method. Furthermore, although they have not been studied in detail, the individualised gradients may also provide more information about subsurface morphology of the tissue.

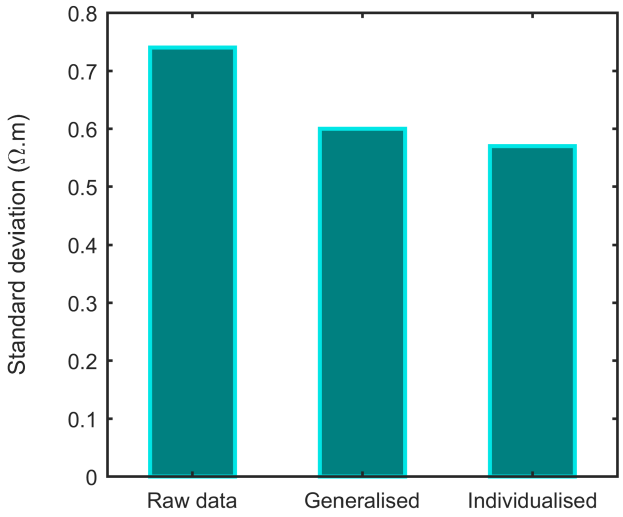

Figure 7.11: Bar plots of the standard deviation from all raw data, generalised compensated data and the individualised compensated data.

By reporting individual r_0 and m parameters, the problem of different gradients is solved but the mucus layer is still a confounding factor on bioimpedance measurements that might offset the r_0 readings as shown in Figure 7.10. For example, this can be seen, Figure 7.7(a), in specimen 5 for user 1 and 2, where the difference between the first and the second attempt is quite large). Note that a 200 µm mucus layer can change up to 33% the reading, which can explain the offset between the first and second trial in specimen 5. It is believed that in this instance the added error for the general pressure compensation method (due to the unmatched gradient from each site), it is actually helping to reduce that difference between trials seen in Figure 7.7(b). On the other hand, surprisingly, looking at the individual gradients, it seems that the m parameters behave differently; the mucus layer seem to have less effect on the gradients (e.g. in specimen 5 for both users the r0 values are apart whereas the m values are much closer, especially for user 2).

This is the first time that resistivity-contact pressure gradients are being reported, albeit other studies used the stiffness and elasticity (mechanical properties) readings of samples to differentiate between normal and malignant tissue (Lekka, 2016; Prabhune et al., 2012). Similarly, the gradient parameter, m, could be potentially valuable to add information on bioimpedance measurements to distinguish between normal and malignant tissue since it is dependent on electrical and mechanical (electromechanical) properties.

While this approach is starting to look promising, it still requires further investigation to determine the maximum recommended contact pressure and also the protocol used to gather the data. A suggested protocol for the individualised proposed method could be as follows:

1. calibrate pressure and impedance sensors before use;
2. clean probe tip to remove any residual mucous layer;
3. perform the measurement slowly increasing the contact pressure;
4. reach a pre-determined target pressure; and
5. release contact pressure.

Then, data analysis will plot resistivity over contact pressure to individually fit a linear curve per measurement and determine extrapolated resistivity at 0 kPa, r_0, and the gradient, m.

Overall, the resistivity results obtained during these studies were consistent but slightly lower than the data published (colon; resistivity 4.17 Ω.m) in (Gabriel, Gabriel and Corthout, 1996). The simulated results showed that this could be attributed to different mucus layer.

7.5 Conclusion

A new method to standardize bioimpedance measurements is suggested here, based on continuous variation of contact pressure from 0 up to pre-determined target pressure, (below 20 kPa). The proposed method has taken into consideration the electromechanical properties of the sample (i.e. resistivity changes over contact-pressure), which might have the potential to differentiate tissue conditions. Ultimately both gradient and intercept data may be required to accurately assess tissue condition, and protocols may need to

be refined to ensure that confounding factors such as mucosal contamination are avoided. Future work is required to fully validate this method and identify the usability for *in-vivo* measurements.

Chapter 8

Conclusions and future directions

8.1 Conclusions

The aims of the research reported in this thesis were to improve some of the current technologies based on bioimpedance for the diagnosis of FGIDs. Limitations of the technology were found in the literature, and based on those limitations the aims of the thesis were set out.

More specifically, the aims were:

1. To develop a method to distinguish between luminal content during *in-vitro* experiments by means of impedance spectroscopy measurements.
2. To develop a new HRIM catheter based on fibre optic sensors with closer electrode separation.
3. To evaluate the effect of closer electrode separation (10 mm) on animal models, and compare the data with data from commercial HRIM catheters.
4. To monitor and control the contact pressure on bioimpedance measurements in a manner suitable for *in-vivo* measurements.
5. To standardize bioimpedance measurements based on controlled variation of contact pressure in order to reduce the variability in data.

To be able to carry out all the stated aims three catheters, instrumentation and multiple software interfaces were designed, built, and implemented; and tested in either *in-vitro* or *ex-vivo* experiments. More specifically:

1. A bioimpedance measurement system to measure electrical impedance on biological tissues, which was able to set different measuring frequencies, acquire and send data to a computer or laptop, and to be used with the four-electrode catheter and the pencil probe.
2. A four-electrode catheter for bolus transit studies to identify the nature of the luminal content, using five measuring frequencies from 1 kHz to 1 MHz logarithmically spaced, tested in a section of guinea pig proximal colon.
3. A novel custom HRIM catheter with closely spaced electrodes, tested in a section of a guinea-pig distal colon and two sections of rabbit proximal colon; and compared with experimental results from a commercial HRIM catheter.

4. A novel pencil probe with four electrodes, contact pressure and temperature sensors, tested in a section of guinea pig colon and five resected sections of human colon.

5. A 3D simulated model to validate and provide insightful details to the experimental results from the bolus transit studies.

6. Three software applications were implemented to communicate and interface with the built bioimpedance measurement system and the additional equipment (optical interrogator units), set equipment's parameters, save and display acquired data in real-time.

The main conclusions of the work described in this thesis are as follows:

1. This is the first time that complex impedance (impedance magnitude and phase angle) and different measuring frequencies have been used for bolus transit studies. Impedance magnitude and phase angle can differentiate between liquid and air moisture content. The differences between impedance magnitude of liquid and gas were found to be larger at low frequencies ($\sim$ 1 kHz), whereas for phase angle they were larger at high frequencies ($\sim$ 177.81 kHz).

2. Phase angle showed a better correlation with luminal diameter than impedance magnitude for liquid content. The best correlation between phase angle and luminal diameter ($PCC = 0.87$) was found at a measuring frequency of 177.81 kHz.

3. The 3D simulated results provided strong qualitative agreement with respect the experimental results.

4. Fibre optic sensors reduce the need for excessive wire counts in HRIM catheters, allowing closer spacing of impedance electrodes.

5. Improving spatial resolution of impedance sensors gives better results for small animal studies, allowing the detection of subtle changes in luminal diameter, such as myogenic contractions, in composite Impedance Pressure Maps (IPMaps).

6. Reducing the electrode separation increases the sensitivity to changes in diameter and to spatial resolution of bolus measurements. That is, a small change in volume or conductivity will be better picked up on closer electrode separation than wider separation as the resulting impedance is dependent on the conductivity over the volume between the pair of electrodes and the luminal wall.

7. The variations commonly seen in bioimpedance measurements are largely due to variations in contact force, and this has been addressed by designing a device that

contains an in-built contact pressure sensor suitable for use via the instrument of an endoscope.

8. The experimental results showed that monitoring and controlling contact pressure reduces the variability in bioimpedance measurements. Furthermore, by recording the bioimpedance and contact pressure simultaneously provides a mean of standardizing *in-vivo* bioimpedance measurements.

9. A proposed technique for standardizing bioimpedance measurements based on continuous variation of contact pressure to generate individual intercept and gradient is suggested.

The results presented in this thesis were limited in several ways. The limitations were:

1. The number of specimens used to validate the devices was limited due to access to suitable tissue types. The low specimen number could be a limitation, and a study with more specimens might be required; however, the 3D simulated results in this thesis and the agreement with other published works adds confidence to the results.

2. Lateral forces have not been considered in the pencil probe, as it is easy to exert a perpendicular measurement on *in-vitro* experiments; however, that may not be the case during *in-vivo* measurements, where the probe accesses the tissue through the port of the endoscope.

3. Although the results from the suggested data compensation methods are promising, the results have not been correlated with histological studies of the samples taken. Histological examination is likely to provide more insights into correlations between bioimpedance measurements and tissue sub-types.

8.2 Future work and directions

The work presented in this thesis set out to develop new and improved methods based on electrical impedance to gain a better understanding of FGIDs. The findings in this thesis add new knowledge and insight, and will lead to further work in GI diagnostics including the following:

Firstly, the closer space impedance electrodes and the use of electrical impedance spectroscopy findings provide improved sensitivity and a way to characterize different luminal

content. These findings will extend bolus presence techniques to small animal studies and improve human measurements.

Secondly, the development of the pencil probe will allow further experimentation on contact pressure dependency on bioimpedance measurements, and a possible compensation method for tissue characterization on *ex-vivo* and *in-vivo* measurements. Further *ex-vivo* experimentation including histology studies is required to validate this method and to link gradient with tissue sub-type and/or condition.

These findings open the door to a new range of *in-vivo* human measurements and gain further knowledge and insight on FGIDs (both functional and structural disorders); however, further design and development of the devices are needed to enable *in-vivo* use.

Finally, it would be possible to combine both the custom HRIM catheter and the pencil probe together. This would be possible due to the use of fibre optic pressure sensor that provides a way to manufacture multiple pressure elements in a single fibre, and combine it with bioimpedance devices suitable for *in-vivo* biopsy and assays.

8.3 Concluding statement

The work presented in this thesis provides with new and improved methods, based on bioimpedance technique in combination with fibre optic sensing, for having a better understanding of functional and motility mechanisms of the lower GI tract. The additional information provided by the developed methods will allow researchers and clinicians to understand and gain insight on the physiology and pathophysiology of FGIDs. Further work is now required to evaluate the potential of such methods on *in-vivo* experiments, and to fully validate the proposed contact pressure compensation method for tissue characterization. This may allow the identification of new motor patterns in more realistic *in-vivo* environments.

References

Abdool, Z., Sultan, A. H. and Thakar, R. (2012), 'Ultrasound imaging of the anal sphincter complex: a review.', *The British journal of radiology* **85**(1015), 865–75.

Abdul Rahman, M. S., Mukhopadhyay, S. C. and Yu, P.-L. (2014), *Novel Sensors for Food Inspection: Modelling, Fabrication and Experimentation*, Vol. 10 of *Smart Sensors, Measurement and Instrumentation*, Springer International Publishing, Cham.

Abid, S. and Lindberg, G. (2007), 'Electrogastrography: Poor correlation with antroduodenal manometry and doubtful clinical usefulness in adults', *World Journal of Gastroenterology* **13**(38), 5101–5107.

Al-Zaben, A. and Chandrasekar, V. (2004), 'Computation of intraluminal impedance', *Physiological Measurement* **25**(1), 61–70.

Al-Zaben, A. and Chandrasekar, V. (2005), 'Effect of esophagus status and catheter configuration on multiple intraluminal impedance measurements', *Physiological Measurement* **26**(3), 229–238.

Albuquerque, A. (2015), 'Endoanal ultrasonography in fecal incontinence: Current and future perspectives', *World Journal of Gastrointestinal Endoscopy* **7**(6), 575.

American Cancer Society (2015), 'Global Cancer Facts & Figures 3rd Edition.', *American Cancer Society* (800), 1–64.

American Cancer Society (2017), 'Cancer Prevention & Early Detection: Facts & Figures 2017-2018', *American Cancer Society* .

Arkwright, J. W., Blenman, N. G., Underhill, I. D., Maunder, S. A., Spencer, N. J., Costa, M., Brookes, S. J., Szczesniak, M. M. and Dinning, P. G. (2011), 'A fibre optic catheter for simultaneous measurement of longitudinal and circumferential muscular activity in the gastrointestinal tract.', *Journal of biophotonics* **4**(4), 244–51.

Arkwright, J. W., Blenman, N. G., Underhill, I. D., Maunder, S. A., Szczesniak, M. M., Dinning, P. G. and Cook, I. J. (2009), 'In-vivo demonstration of a high resolution

optical fiber manometry catheter for diagnosis of gastrointestinal motility disorders.', *Optics express* **17**(6), 4500–4508.

Arkwright, J. W., Underhill, I. D., Maunder, S. a., Blenman, N., Szczesniak, M. M., Wiklendt, L., Cook, I. J., Lubowski, D. Z. and Dinning, P. G. (2009), 'Design of a high-sensor count fibre optic manometry catheter for in-vivo colonic diagnostics.', *Optics express* **17**(25), 22423–22431.

Ates, F., Yuksel, E. S., Higginbotham, T., Slaughter, J. C., Mabary, J., Kavitt, R. T., Garrett, C. G., Francis, D. and Vaezi, M. F. (2015), 'Mucosal Impedance Discriminates GERD From Non-GERD Conditions', *Gastroenterology* **148**(2), 334–343.

Australian Institute of Health and Welfare (2017), *Cancer in Australia. Cancer series no. 101.*

Aziz, Q., Fass, R., Gyawali, C. P., Miwa, H., Pandolfino, J. E. and Zerbib, F. (2016), 'Esophageal disorders', *Gastroenterology* **150**(6), 1368–1379.

Baldini, F., Giannetti, A., Mencaglia, A. and Trono, C. (2008), 'Fiber optic sensors for biomedical applications', *Current Analytical Chemistry* **4**(4), 378–390.

Barthel, A., Nacke, T., Frense, D. and Pliquett, U. (2012), 'Electrodes – the challenge in electrical characterization of biological material', *Journal of Physics: Conference Series* **407**, 12027.

Beltran, N. E., Garcia, L. E. and Garcia-Lorenzana, M. (2013), 'Gastric tissue damage analysis generated by ischemia: Bioimpedance, confocal endomicroscopy, and light microscopy', *BioMed Research International* **2013**.

Beltran, N. E. and Sacristan, E. (2015), 'Gastrointestinal ischemia monitoring through impedance spectroscopy as a tool for the management of the critically ill', *Experimental Biology and Medicine* pp. 1–11.

Beltran, N. E., Sanchez-Miranda, G., Godinez, M., Diaz, U. and Sacristan, E. (2006), 'Gastric impedance spectroscopy in elective cardiovascular surgery patients.', *Physiological measurement* **27**(3), 265–277.

Bredenoord, A. J. and Smout, A. J. P. M. (2013), 'Advances in motility testing- current and novel approaches', *Nature reviews. Gastroenterology & hepatology* **10**(8), 463–72.

Bredenoord, a. J., Weusten, B. L. a. M., Timmer, R. and Smout, a. J. P. M. (2004), 'Minimum sample frequency for multichannel intraluminal impedance measurement of the oesophagus', *Neurogastroenterology and Motility* **16**(6), 713–719.

Brown, B. H. (2003), 'Electrical impedance tomography (EIT): a review.', *Journal of medical engineering & technology* **27**(3), 97–108.

Camilleri, M. (1995), 'The functional gastrointestinal disorders: Diagnosis, pathophysiology, and treatment', *Gastroenterology* **109**(4), 1404.

Carlson, D. A., Lin, Z., Rogers, M. C., Lin, C. Y., Kahrilas, P. J. and Pandolfino, J. E. (2015), 'Utilizing functional lumen imaging probe topography to evaluate esophageal contractility during volumetric distention: A pilot study', *Neurogastroenterology and Motility* **27**(7), 981–989.

Cassilly, D., Kantor, S., Knight, L. C., Maurer, A. H., Fisher, R. S., Semler, J. and Parkman, H. P. (2008), 'Gastric emptying of a non-digestible solid: assessment with simultaneous SmartPill pH and pressure capsule, antroduodenal manometry, gastric emptying scintigraphy', *Neurogastroenterology & Motility* **20**(4), 311–319.

Chao, P. J., Huang, E. Y., Cheng, K. S. and Huang, Y. J. (2013), 'Electrical impedance spectroscopy as electrical biopsy for monitoring radiation sequelae of intestine in rats', *BioMed Research International* **2013**.

Cole, K. S. and Cole, R. H. (1941), 'Dispersion and Absorption in Dielectrics I. Alternating Current Characteristics', *The Journal of Chemical Physics* **9**(4), 341.

Cook, B. J., Lim, E., Cook, D., Hughes, J., Chow, C. W., Stanton, M. P., Bidarkar, S. S., Southwell, B. R. and Hutson, J. M. (2005), 'Radionuclear transit to assess sites of delay in large bowel transit in children with chronic idiopathic constipation', *Journal of Pediatric Surgery* **40**(3), 478–483.

Costa, M., Wiklendt, L., Arkwright, J. W., Spencer, N. J., Omari, T., Brookes, S. J. H. and Dinning, P. G. (2013), 'An experimental method to identify neurogenic and myogenic active mechanical states of intestinal motility.', *Frontiers in systems neuroscience* **7**(April), 7.

de Jonge, C. S., Smout, A. J. P. M., Nederveen, A. J. and Stoker, J. (2018), 'Evaluation of gastrointestinal motility with MRI : Advances , challenges and opportunities', *Neurogastroenterology & Motility* **30**(October 2017), 1–7.

Dean, D. a., Ramanathan, T., Machado, D. and Sundararajan, R. (2008), 'Electrical impedance spectroscopy study of biological tissues', *Journal of Electrostatics* **66**(3-4), 165–177.

Dinning, P. G. (2018), 'A new understanding of the physiology and pathophysiology of colonic motility?', *Neurogastroenterology & Motility* (February), e13395.

Dinning, P. G., Arkwright, J. W., Costa, M., Wiklendt, L., Hennig, G., Brookes, S. J. H. and Spencer, N. J. (2011), 'Temporal relationships between wall motion, intraluminal pressure, and flow in the isolated rabbit small intestine.', *American journal of physiology. Gastrointestinal and liver physiology* **300**(4), G577–G585.

Dinning, P. G., Arkwright, J. W., Gregersen, H., O'Grady, G. and Scott, S. M. (2010), 'Technical advances in monitoring human motility patterns: Review article', *Neurogastroenterology and Motility* **22**(4), 366–380.

Dinning, P. G., Costa, M., Brookes, S. J. and Spencer, N. J. (2012), 'Neurogenic and myogenic motor patterns of rabbit proximal, mid, and distal colon', *AJP: Gastrointestinal and Liver Physiology* **303**(1), G83–G92.

Dinning, P. G., Hunt, L. M., Arkwright, J. W., Patton, V., Szczesniak, M. M., Wiklendt, L., Davidson, J. B., Lubowski, D. Z. and Cook, I. J. (2012), 'Pancolonic motor response to subsensory and suprasensory sacral nerve stimulation in patients with slow-transit constipation.', *The British journal of surgery* **99**(7), 1002–10.

Dinning, P. G., Wiklendt, L., Gibbins, I., Patton, V., Bampton, P., Lubowski, D. Z., Cook, I. J. and Arkwright, J. W. (2013), 'Low-resolution colonic manometry leads to a gross misinterpretation of the frequency and polarity of propagating sequences: Initial results from fiber-optic high-resolution manometry studies', *Neurogastroenterology and Motility* **25**(10), 640–649.

Dinning, P. G., Wiklendt, L., Maslen, L., Gibbins, I., Patton, V., Arkwright, J. W., Lubowski, D. Z., O'Grady, G., Bampton, P. a., Brookes, S. J. and Costa, M. (2014), 'Quantification of in vivo colonic motor patterns in healthy humans before and after a meal revealed by high-resolution fiber-optic manometry', *Neurogastroenterology & Motility* pp. n/a–n/a.

Drossman, D. a. (2006), 'The functional gastrointestinal disorders and the Rome III process.', *Gastroenterology* **45 Suppl 2**, II1–I5.

Drossman, D. A. (2016), 'Functional gastrointestinal disorders: History, pathophysiology, clinical features, and Rome IV', *Gastroenterology* **150**(6), 1262–1279e2.

Dudykevych, T., Gersing, E., Thiel, F. and Hellige, G. (2001), 'Impedance analyser module for EIT and spectroscopy using undersampling.'.

Dziuda, L., Skibniewski, F. W., Mariusz Krej and Lewandowski, J. (2012), 'Monitoring Respiration and Cardiac Activity Using Fiber Bragg Grating-Based Sensor', *IEEE Transactions on Biomedical Engineering* **59**(7), 1934–1942.

Everhart, J. (2008), *The Burden of Digestive Diseases in the United States*, us departm edn, US Government Printing Office, 2008; NIH Publication No. 09-6443, Washington, DC.

Fischer, J., Dejmkova, H. and Barek, J. (2011), 'Electrochemistry of Pesticides and its Analytical Applications', *Current Organic Chemistry* **15**(17), 2923–2935.

Foster, K. R. and Schwan, H. P. (1989), 'Dielectric properties of tissues and biological materials: a critical review.'.

Fox, M. R., Kahrilas, P. J., Roman, S., Gyawali, C. P., Scott, S. M., Rao, S. S., Keller, J. and Camilleri, M. (2018), 'Clinical measurement of gastrointestinal motility and function: who, when and which test?', *Nature Reviews Gastroenterology & Hepatology* **15**(9), 568–579.

Frenette, C. T. and Strum, W. B. (2007), 'Relative rates of missed diagnosis for colonoscopy, barium enema, and flexible sigmoidoscopy in 379 patients with colorectal cancer', *Journal of Gastrointestinal Cancer* **38**(2-4), 148–153.

Gabriel, C., Gabriel, S. and Corthout, E. (1996), 'The dielectric properties of biological tissues : I. Literature survey', *Physics in Medicine and Biology* **41**(11), 2231–2249.

Gabriel, C., Peyman, a. and Grant, E. H. (2009), 'Electrical conductivity of tissue at frequencies below 1 MHz.', *Physics in medicine and biology* **54**(16), 4863–4878.

Gabriel, S., Lau, R. W. and Gabriel, C. (1996*a*), 'The dielectric properties of biological tissues: II. Measurements in the frequency range 10 Hz to 20 GHz', *Physics in medicine and biology* **41**(11), 2251–2269.

Gabriel, S., Lau, R. W. and Gabriel, C. (1996*b*), 'The dielectric properties of biological tissues: III. Parametric models for the dielectric spectrum of tissues.', *Physics in medicine and biology* **41**(11), 2271–2293.

Galmiche, J. P., Clouse, R. E., Bálint, A., Cook, I. J., Kahrilas, P. J., Paterson, W. G. and Smout, A. J. (2006), 'Functional Esophageal Disorders', *Gastroenterology* **130**(5), 1459–1465.

González, C. a., Villanueva, C., Kaneko-Wada, F. T. and Sacristán, E. (2007), 'Gastric tonometry and impedance spectroscopy as a guide to resuscitation therapy during experimental septic shock in pigs', *In Vivo* **21**(6), 989–1002.

Gonzalez, C., Villanueva, C., Othman, S. and Sacristan, E. (2003), 'Classification of impedance spectra for monitoring ischemic injury in the gastric mucosa in a septic

shock model in pigs', *Proceedings of the 25th Annual International Conference of the IEEE Engineering in Medicine and Biology Society* **3**, 3–6.

González-Correa, C. A., Brown, B. H., Smallwood, R. H., Kalia, N., Stoddard, C. J., Stephenson, T. J., Haggie, S. J., Slater, D. N. and Bardhan, K. D. (1999), 'Virtual biopsies in Barrett's esophagus using an impedance probe'.

Gonzalez-Correa, C. A., Brown, B. H., Smallwood, R. H., Stephenson, T. J., Stoddard, C. J. and Bardhan, K. D. (2003), 'Low frequency electrical bioimpedance for the detection of inflammation and dysplasia in Barrett's oesophagus', *Physiological Measurement* **24**(2), 291–296.

González-Correa, C. a., Brown, B. H., Smallwood, R. H., Walker, D. C. and Bardhan, K. D. (2005), 'Electrical bioimpedance readings increase with higher pressure applied to the measuring probe.', *Physiological measurement* **26**(2), S39–S47.

González-Sosa, J., Ruiz-Vargas, A., Arias, G. and Ivorra, A. (2014), 'Fast flow-through non-thermal pasteurization using constant radiofrequency electric fields', *Innovative Food Science and Emerging Technologies* **22**(January), 116–123.

Grimnes, S. and Martinsen, Ø. G. (2007), 'Sources of error in tetrapolar impedance measurements on biomaterials and other ionic conductors', *Journal of Physics D: Applied Physics* **40**(1), 9–14.

Grimnes, S. and Martinsen, Ø. G. (2008), *Bioimpedance and bioelectricity basics*, Academic.

Hennig, G. W., Costa, M., Chen, B. N. and Brookes, S. J. H. (1999), 'Quantitative analysis of peristalsis in the guinea-pig small intestine using spatio-temporal maps', *Journal of Physiology* **517**(2), 575–590.

Ho, S. C. M., Razavi, M., Nazeri, A. and Song, G. (2012), 'FBG sensor for contact level monitoring and prediction of perforation in cardiac ablation', *Sensors* **12**(1), 1002–1013.

Hoad, C. L., Menys, A., Garsed, K., Marciani, L., Hamy, V., Murray, K., Costigan, C., Atkinson, D., Major, G., Spiller, R. C., Taylor, S. A. and Gowland, P. A. (2016), 'Colon wall motility: Comparison of novel quantitative semi-automatic measurements using cine MRI', *Neurogastroenterology and Motility* **28**(3), 327–335.

Hung, K., Lee, C. C., Chan, W. M. and Kwok, P. (2012), Development of novel wearable sensors for mobile health, *in* 'Proceedings of 2012 IEEE-EMBS International Conference on Biomedical and Health Informatics', IEEE, pp. 745–747.

Ivorra, A. (2005), Contributions To the Measurement of Electrical Impedance for Living Tissue, PhD thesis.

Ivorra, A., Genescà, M., Sola, A., Palacios, L., Villa, R., Hotter, G. and Aguiló, J. (2005), 'Bioimpedance dispersion width as a parameter to monitor living tissues.', *Physiological measurement* **26**(2), S165–S173.

Ivorra, A. and Rubinsky, B. (2007), 'In vivo electrical impedance measurements during and after electroporation of rat liver', *Bioelectrochemistry* **70**(2), 287–295.

Ivorra, A., Shini, M. and Rubinsky, B. (2009), 'Linear Superposition Electrical Impedance Tomography Imaging With Multiple Electrical/Biopsy Probes', *IEEE Transactions on Biomedical Engineering* **56**(5), 1465–1472.

Kahrilas, P. J. and Sifrim, D. (2008), 'High-Resolution Manometry and Impedance-pH/Manometry: Valuable Tools in Clinical and Investigational Esophagology', *Gastroenterology* **135**(3), 756–769.

Kassanos, P., Ip, H. M. D. and Yang, G. Z. (2015), 'A tetrapolar bio-impedance sensing system for gastrointestinal tract monitoring', *2015 IEEE 12th International Conference on Wearable and Implantable Body Sensor Networks, BSN 2015* .

Kennedy, B. F., Koh, S. H., McLaughlin, R. A., Kennedy, K. M., Munro, P. R. T. and Sampson, D. D. (2012), 'Strain estimation in phase-sensitive optical coherence elastography.', *Biomedical optics express* **3**(8), 1865–79.

Keshtkar, A. and Keshtkar, A. (2008), 'The effect of applied pressure on the electrical impedance of the bladder tissue using small and large probes.', *Journal of medical engineering & technology* **32**(6), 505–511.

Keshtkar, A., Keshtkar, A. and Smallwood, R. H. (2006), 'Electrical impedance spectroscopy and the diagnosis of bladder pathology.', *Physiological measurement* **27**(7), 585–596.

Keshtkar, A., Salehnia, Z., Keshtkar, A. and Shokouhi, B. (2012), 'Bladder cancer detection using electrical impedance technique (Tabriz Mark 1)', *Pathology Research International* **2012**(1967).

Keshtkar, a., Salehnia, Z., Somi, M. H. and Eftekharsadat, a. T. (2012), 'Some early results related to electrical impedance of normal and abnormal gastric tissue', *Physica Medica* **28**(1), 19–24.

Keysight Technologies (n.d.), 'E4990A Impedance Analyzer, 20 Hz to 10/20/30/50/120 MHz | Keysight (Agilent)'.

URL: *https://www.keysight.com/en/pd-2405177-pn-E4990A/impedance-analyzer-20-hz-to-10-20-30-50-120-mhz?cc=AU&lc=eng*

Khafaji, M., Shahrokhian, S. and Ghalkhani, M. (2011), 'Electrochemistry of Levo-Thyroxin on Edge-Plane Pyrolytic Graphite Electrode: Application to Sensitive Analytical Determinations', *Electroanalysis* **23**(8), 1875–1880.

Kierszenbaum, A. L. and Tres, L. (2015), *Histology and cell biology : an introduction to pathology*, 4th ed. edn, Elsevier Inc., Philadelphia.

Knabe, M., Kurz, C., Knoll, T., Velten, T., Vieth, M., Manner, H., Ell, C. and Pech, O. (2013), 'Diagnosing early Barrett's neoplasia and oesophageal squamous cell neoplasia by bioimpedance spectroscopy in human tissue.', *United European gastroenterology journal* **1**(4), 236–41.

Kuizenga, M. H., Sia, T. C., Dodds, K. N., Wiklendt, L., Arkwright, J. W., Thomas, A., Brookes, S. J., Spencer, N. J., Wattchow, D. a., Dinning, P. G. and Costa, M. (2014), 'Neurally mediated propagating discrete clustered contractions superimposed on myogenic ripples in ex vivo segments of human ileum', *AJP: Gastrointestinal and Liver Physiology* **308**(1), G1–G11.

Lacy, B. E., Mearin, F., Chang, L., Chey, W. D., Lembo, A. J., Simren, M. and Spiller, R. (2016), 'Bowel disorders', *Gastroenterology* **150**(6), 1393–1407e5.

Laufer, S., Ivorra, A., Reuter, V. E., Rubinsky, B. and Solomon, S. B. (2010), 'Electrical impedance characterization of normal and cancerous human hepatic tissue.', *Physiological measurement* **31**(7), 995–1009.

Leaper, M., Johnston, M. J., Barclay, M., Dobbs, B. R. and Frizelle, F. A. (2004), 'Reasons for failure to diagnose colorectal carcinoma at colonoscopy', *Endoscopy* **36**(6), 499–503.

Lekka, M. (2016), 'Discrimination Between Normal and Cancerous Cells Using AFM', *BioNanoScience* **6**(1), 65–80.

Li, C., Huang, Z. and Wang, R. K. (2011), 'Elastic properties of soft tissue-mimicking phantoms assessed by combined use of laser ultrasonics and low coherence interferometry', *Optics Express* **19**(11), 10153.

Li, N., Xu, H., Wang, W., Zhou, Z., Qiao, G. and Li, D. D.-U. (2013), 'A high-speed bioelectrical impedance spectroscopy system based on the digital auto-balancing bridge method', *Measurement Science and Technology* **24**(6), 065701.

Li, Z., Carter, D., Eliakim, R., Zou, W., Wu, H., Liao, Z., Gong, Z., Wang, J., Chung, J. W., Song, S. Y., Xiao, G., Duan, X. and Wang, X. (2014), The Current Main Types

of Capsule Endoscopy, *in* 'Handbook of Capsule Endoscopy', Springer Netherlands, Dordrecht, pp. 5–45.

Lindner, E., Mörbitz, J., Chojetzki, C., Becker, M., Brückner, S., Schuster, K., Rothhardt, M. and Bartelt, H. (2011), Draw tower fiber Bragg gratings and their use in sensing technology, *in* S. J. Mihailov, H. H. Du and G. Pickrell, eds, 'Proceedings SPIE 8028, Fiber Optic Sensors and Applications VIII', Vol. 8028, International Society for Optics and Photonics, p. 7.
URL: *http://proceedings.spiedigitallibrary.org/proceeding.aspx?articleid=1350838*

Locke, G. R., Zinsmeister, A. R., Fett, S. L., Melton, L. J. and Talley, N. J. (2005), 'Overlap of gastrointestional symptom complexes in a US community', *Neurogastroenterology and Motility* **17**(1), 29–34.

Longstreth, G. F., Thompson, W. G., Chey, W. D., Houghton, L. A., Mearin, F. and Spiller, R. C. (2006), 'Functional Bowel Disorders', *Gastroenterology* **130**(5), 1480–1491.

López-Amo, M. and López-Higuera, J. (2011), Multiplexing techniques for FBG sensors, *in* A. Cusano, A. Cutolo and J. Albert, eds, 'Fiber Bragg Grating Sensors: Recent Advancements, Industrial Applications and Market Exploitation', chapter 6, pp. 99–115.

Lundin, P., Karpefors, M., Carlsson, K., Hansen, M. B. and Ruth, M. (2011), 'Bioimpedance spectroscopy: A new tool to assess early esophageal changes linked to gastroesophageal reflux disease?', *Diseases of the Esophagus* **24**(7), 462–469.

Madsen, J. L. (2014), 'Scintigraphic assessment of gastrointestinal motility: A brief review of techniques and data interpretation', *Clinical Physiology and Functional Imaging* **34**(4), 243–253.

Malleo, D., Nevill, J. T., Van Ooyen, a., Schnakenberg, U., Lee, L. P. and Morgan, H. (2010), 'Note: Characterization of electrode materials for dielectric spectroscopy', *Review of Scientific Instruments* **81**(1).

Mary, D. A., North, P. J. and Hunt, J. N. (1979), 'Scanning esophageal impedance probe for measurement of luminal cross section', *Am J Physiol* **236**(5), E545–9.

Mazzeo, B. a. (2009), 'Parasitic capacitance influence of potential-sensing electrodes on four-electrode liquid impedance measurements', *Journal of Applied Physics* **105**(9).

Mazzeo, B. a. and Flewitt, A. J. (2007), 'Two- and four-electrode, wide-bandwidth, dielectric spectrometer for conductive liquids: Theory, limitations, and experiment', *Journal of Applied Physics* **102**(10).

McAdams, E. T. (2006), Bioelectrodes, *in* J. G. Webster, ed., 'IEEE Engineering in Medicine and Biology Magazine', second edn, Vol. 25, pp. 120–166.

McAdams, E. T. and Jossinet, J. (1995), 'Tissue impedance: a historical overview.', *Physiological measurement* **16**(3 Suppl A), A1–A13.

McEwan, A., Cusick, G. and Holder, D. S. (2007), 'A review of errors in multi-frequency EIT instrumentation', *Physiological Measurement* **28**(7).

McMahon, B. P., Frøkjær, J. B., Liao, D., Kunwald, P., Drewes, A. M. and Gregersen, H. (2005), 'A new technique for evaluating sphincter function in visceral organs: Application of the functional lumen imaging probe (FLIP) for the evaluation of the oesophagogastric junction', *Physiological Measurement* **26**(5), 823–836.

Menys, A., Keszthelyi, D., Fitzke, H., Fikree, A., Atkinson, D., Aziz, Q. and Taylor, S. A. (2017), 'A magnetic resonance imaging study of gastric motor function in patients with dyspepsia associated with Ehlers-Danlos Syndrome-Hypermobility Type: A feasibility study', *Neurogastroenterology and Motility* **29**(9), 1–9.

Menys, A., Taylor, S. A., Emmanuel, A., Ahmed, A., Plumb, A. A., Odille, F., Alam, A., Halligan, S. and Atkinson, D. (2013), 'Global Small Bowel Motility: Assessment with Dynamic MR Imaging', *Radiology* **269**(2), 443–450.

Mignani, A. and Baldini, F. (1995), 'In-vivo biomedical monitoring by fiber-optic systems', *Journal of Lightwave Technology* **13**(7), 1396–1406.

Mishra, V., Singh, N., Tiwari, U. and Kapur, P. (2011), 'Fiber grating sensors in medicine: Current and emerging applications', *Sensors and Actuators, A: Physical* **167**(2), 279–290.

Mohd Rosli, R., Leibbrandt, R. E., Wiklendt, L., Costa, M., Wattchow, D. A., Spencer, N. J., Brookes, S. J., Omari, T. I. and Dinning, P. G. (2018), 'Discriminating movements of liquid and gas in the rabbit colon with impedance manometry', *Neurogastroenterology and Motility* **30**(5), 1–11.

Mostafa, R. (2008), 'Rome III: The functional gastrointestinal disorders, third edition, 2006', *World Journal of Gastroenterology* **14**(13), 2124.

Mulett-Vásquez, E., Correa-Florez, A., Dussán-Lubert, C., Miranda-Mercado, D. A. and González-Correa, C. A. (2016), In vitro luminal measurements of colon electrical impedance in rabbits, *in* 'IFMBE Proceedings', Vol. 54, Springer, Singapore, pp. 28–31.

Neuman, M. R. (2010), Biopotential Electrodes, *in* 'Medical Instrumentation: Application and Design', p. 713.

Nguyen, H. N., Silny, J. and Matern, S. (1999), 'Multiple intraluminal electrical impedancometry for recording of upper gastrointestinal motility: Current results and further implications', *American Journal of Gastroenterology* **94**(2), 306–317.

Nguyen, N. Q., Holloway, R. H., Smout, A. J. and Omari, T. I. (2013), 'Automated impedance-manometry analysis detects esophageal motor dysfunction in patients who have non-obstructive dysphagia with normal manometry', *Neurogastroenterology & Motility* **25**(3), 238–e164.

Nowakowski, a., Palko, T. and Wtorek, J. (2005), 'Advances in electrical impedance methods in medical diagnostics', *Bulletin Of The Polish Academy Of Sciences Technical Sciences* **53**(3).

Odegaard, S., Nesje, L. B., Hausken, T. and Gilja, O. H. (2015), 'Ultrasonography in gastroenterology', *Scandinavian Journal of Gastroenterology* **50**(6), 698–707.

Ogawa, A., Mizuta, I., Fukunaga, T., Takeuchi, N., Honaga, E., Sugita, Y., Mikami, A., Inoue, Y. and Takeda, M. (2004), 'Electrogastrography abnormality in eating disorders', *Psychiatry and Clinical Neurosciences* **58**(3), 300–310.

Omari, T. I., Dejaeger, E., Van Beckevoort, D., Goeleven, A., Davidson, G. P., Dent, J., Tack, J. and Rommel, N. (2011), 'A method to objectively assess swallow function in adults with suspected aspiration', *Gastroenterology* **140**(5), 1454–1463.

Omari, T. I., Wiklendt, L., Dinning, P., Costa, M., Rommel, N. and Cock, C. (2014), 'Upper esophageal sphincter mechanical states analysis: a novel methodology to describe UES relaxation and opening', *Front Syst Neurosci* **8**(January), 241.

Othman, S., Sacristan, E., Gonzalez, C., Pinzon, J., Aguado, J., Flores, P. and Infante, O. (2003), 'In situ impedance spectroscopy of the intestinal mucosa in an ischemia-reperfusion model', *Proceedings of the 25th Annual International Conference of the IEEE Engineering in Medicine and Biology Society* **4**, 3207–3210.

Pandolfino, J. E. and Kahrilas, P. J. (2009), 'New technologies in the gastrointestinal clinic and research: Impedance and high-resolution manometry', *World Journal of Gastroenterology* **15**(2), 131–138.

Parkinson, L. A., Cook, P. R., Ruiz-Vargas, A. and Arkwright, J. W. (2018), 'Correction of Peak Tracking Ripple in Solid State Spectrometers', *Journal of Lightwave Technology* **36**(18), 3912–3918.

Peery, A. F., Crockett, S. D., Barritt, A. S., Dellon, E. S., Eluri, S., Gangarosa, L. M., Jensen, E. T., Lund, J. L., Pasricha, S., Runge, T., Schmidt, M., Shaheen, N. J., Sandler,

R. S. and Author, C. (2015), 'Burden of Gastrointestinal, Liver, and Pancreatic Diseases in the United States HHS Public Access', *Gastroenterology* **149**(7), 1731–1741.

Peng-fei, L., Guo-jun, L., Qiang, Z., Yong-jie, W. and Fang, L. (2011), A study of the development and application of fiber Bragg grating pressure sensors, *in* '2011 Academic International Symposium on Optoelectronics and Microelectronics Technology', IEEE, pp. 232–235.

Pethig, R. and Kell, D. B. (1987), 'The passive electrical properties of biological systems: Their significance in physiology, biophysics and biotechnology', *Physics in Medicine and Biology* **32**(8), 933–970.

Peyman, a., Gabriel, C. and Grant, E. H. (2007), 'Complex permittivity of sodium chloride solutions at microwave frequencies', *Bioelectromagnetics* **28**(4), 264–274.

Pleros, N., T. Kanellos, G., Papaioannou, G. Y., Kanellos, G. T. and Papaioannou, G. Y. (2009), Optical fiber sensors in orthopedic biomechanics and rehabilitation, *in* '9th International Conference on Information Technology and Applications in Biomedicine, ITAB 2009', number November, IEEE, pp. 5–7.

Podczeck, F., Mitchell, C. L., Newton, J. M., Evans, D. and Short, M. B. (2008), 'The gastric emptying of food as measured by gamma-scintigraphy and electrical impedance tomography (EIT) and its influence on the gastric emptying of tablets of different dimensions (Journal of Pharmacy and Pharmacology (2007) 59, (1527-1536))', *Journal of Pharmacy and Pharmacology* **60**(4), 533.

Poeggel, S., Leen, G., Bremer, K. and Lewis, E. (2012), 'Miniature Optical fiber combined pressure- and temperature sensor for medical applications', *2012 IEEE Sensors* **4**(1), 1–4.

Poeggel, S., Tosi, D., Duraibabu, D., Leen, G., McGrath, D. and Lewis, E. (2015), 'Optical Fibre Pressure Sensors in Medical Applications', *Sensors* **15**(7), 17115–17148.

Portincasa, P., Colecchia, A., Ciaula, A. D., Larocca, A., Muraca, M., Di Ciaula, A., Larocca, A., Muraca, M., Palasciano, G., Roda, E. and Festi, D. (2000), 'Standards for diagnosis of gastrointestinal motility disorders. Section: Ultrasonography', *Digestive and liver disease : official journal of the Italian Society of Gastroenterology and the Italian Association for the Study of the Liver* **32**(2), 160–72.

Prabhune, M., Belge, G., Dotzauer, A., Bullerdiek, J. and Radmacher, M. (2012), 'Comparison of mechanical properties of normal and malignant thyroid cells', *Micron* **43**(12), 1267–1272.

Ramírez-Chavarría, R., Sánchez-Pérez, C., Matatagui, D., Qureshi, N., Pérez-García, A. and Hernández-Ruíz, J. (2018), 'Ex-vivo biological tissue differentiation by the Distribution of Relaxation Times method applied to Electrical Impedance Spectroscopy', *Electrochimica Acta* **276**, 214–222.

Rao, S. S., Bharucha, A. E., Chiarioni, G., Felt-Bersma, R., Knowles, C., Malcolm, A. and Wald, A. (2016), 'Anorectal disorders', *Gastroenterology* **150**(6), 1430–1442e4.

Rao, Y.-J. (1998), Fiber Bragg grating sensors: principles and applications, *in* 'Optical Fiber Sensor Technology', Vol. 2, Springer US, Boston, MA, pp. 355–379.

Rigaud, B., Hamzaoui, L., Frikha, M. R., Chauveau, N. and Morucci, J. P. (1995), 'In vitro tissue characterization and modelling using electrical impedance measurements in the 100 Hz-10 MHz frequency range.', *Physiological measurement* **16**(3 Suppl A), A15–A28.

Rigaud, B., Morucci, J. P. and Chauveau, N. (1996), 'Bioelectrical impedance techniques in medicine. Part I: Bioimpedance measurement. Second section: impedance spectrometry.', *Critical reviews in biomedical engineering* **24**(4-6), 257–351.

Rock, E. S. (2012), 'Impedance spectroscopy system and catheter for ischemic mucosal damage monitoring in hollow viscous organs'.

Rommel, N., Van Oudenhove, L., Tack, J. and Omari, T. I. (2014), 'Automated impedance manometry analysis as a method to assess esophageal function', *Neurogastroenterology & Motility* **26**(5), 636–645.

Sarnelli, G., Vos, R., Cuomo, R., Janssens, J. and Tack, J. (2001), 'Reproducibility of gastric barostat studies in healthy controls and in dyspeptic patients', *American Journal of Gastroenterology* **96**(4), 1047–1053.

Schröder, J., Doerner, S., Schneider, T. and Hauptmann, P. (2004), 'Analogue and digital sensor interfaces for impedance spectroscopy', *Measurement Science and Technology* **15**(7), 1271–1278.

Schwan, H. P. (1957), 'Electrical properties of tissue and cell suspensions.'.

Schwan, H. P. (1968), Electrode polarization impedance and measurements in biological materials, *in* 'Annals of the New York Academy of Sciences', Vol. 1, pp. 191–209.

Shami, V. M. and Waxman, I. (2005), 'Technology insight: Current status of endoscopic ultrasonography', *Nature Clinical Practice Gastroenterology and Hepatology* **2**(1), 38–45.

Silny, J. (1991), 'Intraluminal Multiple Electric Impedance Procedure for Measurement of Gastrointestinal Motility', *Journal of Gastrointestinal Motility* **3**(3), 151–162.

Silny, J., Knigge, K. and Fass, J. (1993), 'Verification of the intraluminal multiple electrical impedance measurement for the recording of gastrointestinal motility', *Neurogastroenterology & Motility* **5**(January), 107–122.

Smallwood, R. H., Keshtkar, A., Wilkinson, B. A., Lee, J. A. and Hamdy, F. C. (2002), 'Electrical Impedance Spectroscopy (EIS) in the Urinary Bladder: The effect of inflammation and Edema on identification of Malignancy', *IEEE Transactions on Medical Imaging* **21**(6), 708–710.

Smallwood, R., Mangnall, Y. and Leathard, A. (1994), 'Transport of gastric contents', *Physiol Meas* **15**(Suppl 2a), A175–188.

Spiller, R. (2000), 'Rome II: The functional gastrointestinal disorders, diagnosis, pathophysiology, and treatment: A multinational consensus', *Gut* **46**(5), 741.

Srinivasan, R., Vela, M. F., Katz, P. O., Tutuian, R., Castell, J. a. and Castell, D. O. (2001), 'Esophageal function testing using multichannel intraluminal impedance.', *American journal of physiology. Gastrointestinal and liver physiology* **280**(3), G457–G462.

Stanfield, C. L. (2010), *Principles of human physiology*, 4th ed. edn, Boston, Mass. : Benjamin Cummings, Boston, Mass.

Stanghellini, V., Chan, F. K., Hasler, W. L., Malagelada, J. R., Suzuki, H., Tack, J. and Talley, N. J. (2016), 'Gastroduodenal disorders', *Gastroenterology* **150**(6), 1380–1392.

Stathopoulos, E., Schlageter, V., Meyrat, B., De Ribaupierre, Y. and Kucera, P. (2005), 'Magnetic pill tracking: A novel non-invasive tool for investigation of human digestive motility', *Neurogastroenterology and Motility* **17**(1), 148–154.

Szarka, L. A. and Camilleri, M. (2009), 'Methods for measurement of gastric motility', *American Journal of Physiology-Gastrointestinal and Liver Physiology* **296**(3), G461–G475.

Szarka, L. A. and Camilleri, M. (2012), 'Methods for the assessment of small-bowel and colonic transit.', *Seminars in nuclear medicine* **42**(2), 113–23.

Tack, J., Talley, N. J., Camilleri, M., Holtmann, G., Hu, P., Malagelada, J.-R. and Stanghellini, V. (2006), 'Functional Gastroduodenal Disorders', *Gastroenterology* **130**(5), 1466–1479.

Talley, N. J., Dennis, E. H., Schettler-Duncan, V. A., Lacy, B. E., Olden, K. W. and Crowell, M. D. (2003), 'Overlapping upper and lower gastrointestinal symptoms in ir-

ritable bowel syndrome patients with constipation or diarrhea.', *The American journal of gastroenterology* **98**(11), 2454–9.

Than, M., Witherspoon, J., Shami, J., Patil, P. and Saklani, A. (2015), 'Diagnostic miss rate for colorectal cancer: An audit', *Annals of Gastroenterology* **28**(1), 94–98.

Torre, L. A., Bray, F., Siegel, R. L., Ferlay, J., Lortet-Tieulent, J. and Jemal, A. (2015), 'Global cancer statistics, 2012', *CA: A Cancer Journal for Clinicians* **65**(2), 87–108.

Tran, K., Brun, R. and Kuo, B. (2012), 'Evaluation of regional and whole gut motility using the wireless motility capsule: relevance in clinical practice', *Therapeutic Advances in Gastroenterology* **5**(4), 249–260.

Tutuian, R. and Castell, D. O. (2005), 'Multichannel intraluminal impedance: General principles and technical issues'.

Tutuian, R., Vela, M. F., Balaji, N. S., Wise, J. L., Murray, J. a., Peters, J. H., Shay, S. S. and Castell, D. O. (2003), 'Esophageal function testing with combined multichannel intraluminal impedance and manometry: Multicenter study in healthy volunteers', *Clinical Gastroenterology and Hepatology* **1**(3), 174–182.

Tutuian, R., Vela, M. F., Shay, S. S. and Castell, D. O. (2003), 'Multichannel intraluminal impedance in esophageal function testing and gastroesophageal reflux monitoring.', *Journal of clinical gastroenterology* **37**(3), 206–215.

Van Oudenhove, L., Levy, R. L., Crowell, M. D., Drossman, D. A., Halpert, A. D., Keefer, L., Lackner, J. M., Murphy, T. B. and Naliboff, B. D. (2016), 'Biopsychosocial Aspects of Functional Gastrointestinal Disorders: How Central and Environmental Processes Contribute to the Development and Expression of Functional Gastrointestinal Disorders', *Gastroenterology* **150**(6), 1355–1367.e2.

Verhagen, M. a. M. T. (2005), 'Electrogastrography', *Clinical Autonomic Research* **15**(6), 364–367.

Wakamiya, M., Furukawa, A., Kanasaki, S. and Murata, K. (2011), 'Assessment of small bowel motility function with cine-MRI using balanced steady-state free precession sequence', *Journal of Magnetic Resonance Imaging* **33**(5), 1235–1240.

Walker, D. C., Brown, B. H., Smallwood, R. H., Hose, D. R. and Jones, D. M. (2002), 'Modelled current distribution in cervical squamous tissue', *Physiological Measurement* **23**(1), 159–168.

Wang, D. H. C., Abbott, a., Maunder, S. a., Blenman, N. G. and Arkwright, J. W. (2012), 'A miniature fiber Bragg grating pressure sensor for in-vivo sensing applications', *22nd International Conference on Optical Fiber Sensors* **8421**, 10–13.

Zhou, Y., Ren, B., Li, B., Xu, J., Jin, Y. and Song, C. (2016), 'Changes in Small Intestine Tissue Compressed by a Linear Stapler Based on ColeY Model', *Annals of Biomedical Engineering* **44**(12), 3583–3592.

Zifan, A., Ledgerwood-Lee, M. and Mittal, R. K. (2015), 'Measurement of peak esophageal luminal cross-sectional area utilizing nadir intraluminal impedance', *Neurogastroenterology & Motility* **27**(7), 971–980.

Zou, Y. and Guo, Z. (2003), 'A review of electrical impedance techniques for breast cancer detection', *Medical Engineering and Physics* **25**(2), 79–90.

Zwart, I. D., Roos, A. D., Verbeek, P., Lamb, H., Kunz, P., Masclee, A., De Zwart, I., De Roos, A., Verbeek, P., Lamb, H., Kunz, P. and Masclee, A. (2003), 'Gastric motility and emptying: Evaluation of the barostat method with MRI', *Gastroenterology* **124**(4), A673.

Appendix A

Electrical impedance and fibre optic sensing technology basics

A.1 Introduction

This appendix provides the reader with the necessary knowledge of the electrical bioimpedance and/or fibre optic sensing to be able to follow the concepts that appear in the chapters in this thesis, and also some supplementary information on the techniques used. The first section is focused on impedance phenomena in biological tissues, followed by the different models and ways to represent data, finishing with the different configurations to perform bioimpedance measurements. The second section gives a brief introduction to fibre optic sensing with a strong focus on Fibre Bragg Gratings (FBGs), interrogation and multiplexing techniques.

A.2 Bioimpedance basics

A.2.1 Introduction

Electrical impedance of biological samples, referred to as electrical bioimpedance, or simply bioimpedance, has been widely used in biomedical applications (Nowakowski et al., 2005), food inspection and other areas (González-Sosa et al., 2014). Electrical impedance is

performed by injecting a small AC current and measuring the associated voltage drop by means of metal electrodes. It can be obtained at a single frequency but it can also be taken across a range of frequencies, in that instance it is referred to as Electrical Impedance Spectroscopy (EIS) or Bioimpedance Spectroscopy (BIS). In the following sections, the reader will have the opportunity to gain the basics to understand how BIS works.

A.2.2 Biological tissues

Living tissues and organs are complex and heterogeneous materials that can be considered as a mixture of conducting and dielectric materials. Electrical conduction within biological tissues is mostly due to unbound ions and molecules in the extracellular and intracellular media. The ions within biological tissues are abundant and free to migrate, and consequently, they are the main charge carriers for the electrical current (ionic current). The structure of the tissues, which are formed by cells of different sizes, cellular membranes and bound charges, may influence the current flow through them (Grimnes and Martinsen, 2008). A simple mechanism is proposed for explaining the frequency dependent behaviour of bioimpedance up to about 10 MHz. At low frequencies (e.g. < 1 kHz), the current flows mainly through the extracellular fluid, while at high frequencies, the cell walls, which act as capacitors, also allow passage of current through the the extracellular and intracellular fluid (inside cells).

Biological tissues show three dispersion regions in the frequency range of 10 Hz to 10 GHz. Figure A.1 depicts those three regions as introduced by Schwan (1957). He characterized these regions, and named them as alpha, beta, gamma (α, β, and γ respectively) dispersion (Schwan, 1957). He also explained their mechanisms of interaction. It is worth noticing that most of the experiments carried out currently and before Schwan are and were made in β dispersion (McAdams and Jossinet, 1995), between 1 kHz to several MHz, which is associated with the dielectric properties of the cell membranes and their interactions with the extra and intracellular medium. This thesis is focused specifically on this region. On the other hand α dispersion, occurring at low frequencies (10 Hz to a few kHz), deals with the ionic diffusion processes in the extracellular medium, whereas γ dispersion (> 10 GHz) is due to polarization of water molecules (Foster and Schwan, 1989).

A.2.3 Electrical properties of biological tissues

Bioimpedance measurement is the term used to express the relation between the measured voltage and the applied current. Other terms such as resistance, conductance and

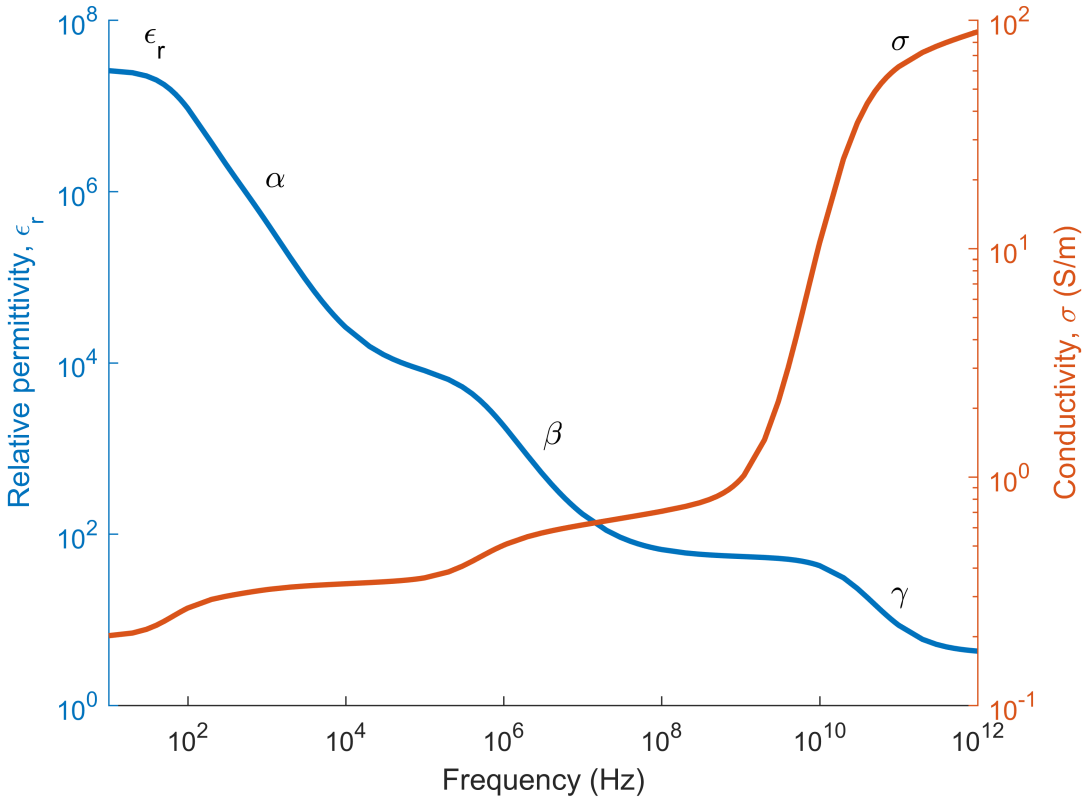

Figure A.1: Conductivity and relative permittivity of living tissue, showing the three dispersion regions identified by Schwan (1957).

admittance are also used in this field. All these parameters are dependent both on the passive electrical properties of the tissue and on the geometrical constraints (Grimnes and Martinsen, 2008). On the other hand, the parameters resistivity, conductivity, and relative permittivity are intrinsic properties of the material (electrical properties) and do not dependent on the geometry used; hence, it is preferable to report the measurements with these latter parameters instead to resistance, conductance and so on. In order to get the passive electrical properties of tissue, the bioimpedance measurements are scaled by a factor known as a cell constant (K; units m^{-1}) that depends on the geometrical constraints of the electrode configuration. Gabriel, Lau and Gabriel (1996*a*) proposed a method to characterize the K factor of any electrode configuration. This method consists in measuring the impedance values of different concentrations of NaCl (sodium chloride water), as its conductivity is well known.

All the equations related to these parameters are shown below (Ivorra, 2005):

Impedance

$$Z = R + jX \quad [\Omega] \tag{A.1}$$

Impedance magnitude

$$|Z| = \sqrt{R^2 + X^2} \quad [\Omega] \tag{A.2}$$

Phase angle

$$\angle Z = \tan^{-1} \frac{X}{R} \quad [^\circ] \tag{A.3}$$

Admittance

$$Y = \frac{1}{Z} \longrightarrow Y = G + jB \quad [S] \tag{A.4}$$

Conductivity

$$Y = G + jB = K(\sigma + j\omega\varepsilon) \longrightarrow \sigma = GK \quad \left[\frac{S}{m}\right] \tag{A.5}$$

Permittivity

$$Y = G + jB = K(\sigma + j\omega\varepsilon) \longrightarrow \varepsilon = \frac{BK}{\omega} \quad \left[\frac{F}{m}\right] \tag{A.6}$$

Relative permittivity

$$\varepsilon_r = \frac{\varepsilon}{\varepsilon_0} \tag{A.7}$$

Resistivity

$$Z = R + jX \longrightarrow \rho = \frac{R}{K} \quad [\Omega m] \tag{A.8}$$

Where:

R is the real part of the impedance and it is known as the resistance.

X is the imaginary part of the impedance and it is known as the reactance.

G is the real part of the admittance and it is known as the conductance.

B is the imaginary part of the admittance and it is known as the capacitance or susceptance.

K is the scaling factor of the measurement.

σ is the conductivity of material.

ε is the permittivity of the material.

ε_r is the relative permittivity of the material.

ρ is the resistivity of the material.

A.2.4 Models and data representation

Bioimpedance measurements can generate a large amount of data, especially when using impedance spectroscopy. For this reason, the data is fitted into a model, that mimics the living tissue behaviour, to simplify the data analysis. A common model used in the literature consists of an electrical circuit model of a resistor in parallel with a capacitor and resistor in series (Figure A.2(a)). Each component represents the dielectric properties of the cell membranes and their interactions with the extra- and intra-cellular medium: R_e corresponds to the extracellular medium resistance, R_i corresponds to the intracellular medium resistance and C_m corresponds to the capacitance formed by the cell membrane. From the electrical point of view, if we analyse the circuit as a function of frequency (from $f = 0$ to $f = \infty$), at low frequencies (< 1 kHz) the current will flow through extracellular medium making the impedance completely resistive whereas at very high frequencies ($>$ 100 kHz), the cell membrane becomes transparent, and current will flow through the intra- and extra-cellular mediums, see Figure A.2(b).

Another method to represent the data is the empirical expression proposed by Cole and Cole (1941), known as the Cole equation (Equation A.9).

$$Z = R_\infty + \frac{R_0 - R_\infty}{1 + (j\omega\tau)^\alpha} \tag{A.9}$$

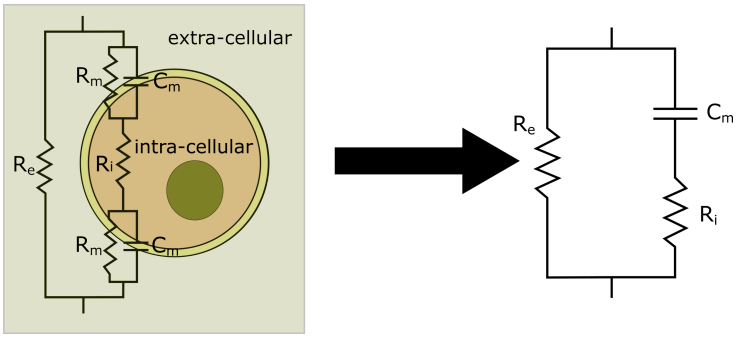

(a)

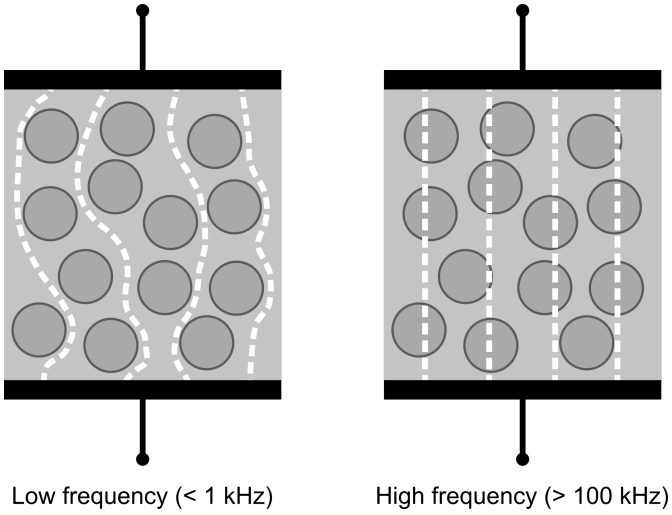

(b)

Figure A.2: (a) An electrical circuit of a single model on the right is shown with its representative components of the model on the left: extracellular resistance (R_e), resistance due to ionic and channels pumps (R_m), intracellular resistance (R_i) and capacitive membrane (C_m). (b) Current paths at low and high frequencies.

where Z is the impedance value at frequency ω, j is the complex number $\sqrt{-1}$, R_∞ is the impedance at infinite frequency, R_0 is the impedance at zero frequency, τ is the characteristic time constant of the system corresponding to a characteristic angular frequency, and α is a dimensionless constant with a value between zero and one (note that if its value is 1, the behaviour is the same as a capacitor). The parameters extracted from this model can be used to monitor living tissue and identify possible tissue states (Ivorra et al., 2005; Ivorra and Rubinsky, 2007). The representation of Cole equation is usually on a Nyquist or Wessel diagram (Figure A.3). Its representation results in a semicircle with its centre on or below the real axis and displaced away from the imaginary axis, the offset below the real axis depends on the α value (if α is 1, then there is a perfect semicircle with its centre on the real axis).

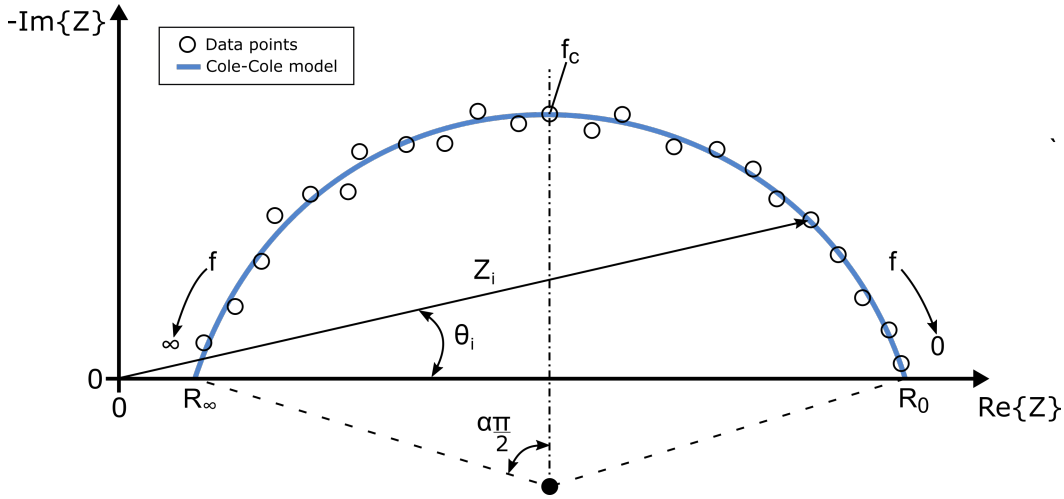

Figure A.3: Cole plot representation with its different parameters.

The equations to pass from the electrical model to Cole-Cole model are shown below:

$$R_0 = R_e \tag{A.10}$$

$$R_\infty = \frac{R_e \cdot R_i}{R_e + R_i} \tag{A.11}$$

$$\tau = C_m(R_e + R_i) \tag{A.12}$$

A.2.5 Impedance measurements

Bioimpedance measurements require a bioimpedance measurement system (BMS) and at least a pair of metallic electrodes. These two parts (BMS and electrodes) are susceptible to intrinsic and extrinsic errors that can affect the measurements (Barthel et al., 2012; McEwan et al., 2007). This subsection considers these artefacts and how to overcome these artefacts to improve bioimpedance measurements.

Impedance analyser

Currently, some commercial impedance analysers from are available, for example from Solartron Analytical® or Keysight Technologies®. These systems are used for impedance measurement in areas such as materials, bio-materials, solar cells, battery research and fuel cells, civil engineering, corrosion studies, circuit boards (Keysight Technologies, n.d.).

However, lacking an isolation stage, required so compliance with human safety requirements is met, their purpose is not tailored to biomedical applications. Additionally, the cost of these commercial impedance analysers are around $30,000 to $60,000. This has motivated some researchers to build their own impedance analysers for specific applications (Dudykevych et al., 2001; Li et al., 2013; Schröder et al., 2004). The complexity and the required measurement speed of the measurements for applications such as impedance tomography is another reason for the lack of suitable equipment, as found in (Brown, 2003). The characteristics that a commercial system can provide are achievable with custom systems (Dudykevych et al., 2001; Schröder et al., 2004). The system, developed by Dudykevych et al. (2001), has achieved an error less than 0.5% for the magnitude and 0.5° for the phase measurement before any calibration to compensate systematic errors. A commercially available model 1260A from (Solartron Analytical®) claims 0.1%, 0.1° accuracy (Keysight Technologies, n.d.).

Electrodes

The electrode is the conductive element of an electrical circuit that allows the circulation of current between two domains with different charge carriers (in bioimpedance measurements, between the metallic conductors of the measuring circuit, which lead by electrons, and the tissue that conducts by ions). So, the electrode is the critical interface for interchanging current between tissue and electronic devices. The electrodes are used in many applications such as the detection of biosignals from endogenic sources, stimulation of nerves and muscles or AC impedance measurements. Different metals are used depending on the application. For living tissue, noble metals such as gold, platinum, iridium, rhodium, palladium and silver are preferred as they are highly biocompatible while providing the conductivity required for charge transfer. The electrode-tissue interface is where the charge-transfer occurs, and electronic current (carried by electrodes) becomes ionic current (carried by ions) and vice versa. This plays a key role in the impedance measurements, as it can create undesired potentials and impedances that affect the measurements.

The contact between a metallic electrode and tissue creates an ion-electron exchange, and an electrochemical reaction happens. Two important electrochemical reactions take place in the interface: Oxidation and Reduction. Oxidation occurs when an atom from metal 'M' loses 'n' electrons and pass into the electrolyte (tissue) as metal ions 'M^{+n}', whereas reduction occurs when ions in solution M^{+n} take n electrons from the metal and deposit onto the electrode as metal atoms 'M'(McAdams, 2006).

$$M \longrightarrow M^{+n} + ne^{-} \tag{A.13}$$

$$M^{+n} + ne^{-} \longrightarrow M \tag{A.14}$$

When these two reactions are taking place under equilibrium conditions, two currents in both directions exist. These are equal, and consequently result in zero net current. Although the net current is zero, these reactions change the concentration of the ions in solution close to the electrode surface, and as a result the electrical potential near by the electrode changes with respect to the solution. This potential established between the electrode and electrolyte is known as the '*half-cell potential*' (Neuman, 2010). However, this half-cell potential (the charge distribution in the solution) can be affected when an external electric field is applied to the electrodes due to a current that passes through the electrode-electrolyte solution. Ions in the electrolyte (tissue) are attracted to the electrode-tissue interface by electrostatic forces creating a layer of opposite charge near the electrode. This is the double layer, and it is separated from the electrode surface by a small distance. The double layer can be considered as a capacitor (C_{dl}), and induces an impedance to the electrode-tissue interface, in which the current (capacitive current) will pass through it when current is applied. In addition, some leakage currents (Faradic current) due to the electrochemical reactions will take place at the interface. These reactions experience a charge transfer resistance (RCT) and can cause the dissolution of metal and a change of pH near the electrode-tissue interface (McAdams, 2006).

To avoid or minimize these errors a number of techniques have been employed. The most common technique used to avoid electrode polarization is the four-electrode configuration (Figure A.4(a)) proposed by Schwan (1968) – he also proposed that varying distance between electrodes can improve the electrodes' performance at low frequencies. This method avoids the electrode polarization since at low frequencies the electrode impedance can be very high (MΩ) (Mazzeo and Flewitt, 2007).

However, at high frequencies a four electrode configuration is susceptible to errors due to parasitic and stray capacitances, and as a consequence a two-electrode configuration (Figure A.4(b)) is preferred at high frequency measurements (Mazzeo, 2009).

Increasing the effective surface area of the electrode by mechanically roughening (sand-blasting) or electrochemical treatment (electroplating) are options used to improve electrodes' performance, as the area of the capacitance is inversely proportional to the interface impedance. These techniques are specially employed in noble metals, (since noble metals are highly polarizable and present large interface impedances) and have been shown to increase the effective capacitance of the electrode by four times. Malleo et al. (2010)

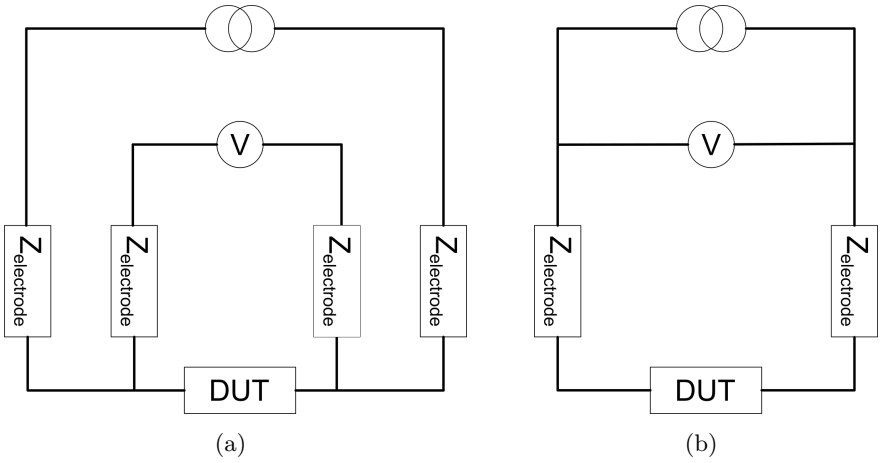

Figure A.4: (a) Four- and (b) two-electrode configuration.

enhanced the performance of a bright platinum electrode with Platinum Black, Iridium Oxide and conducting polymer electroplating. Best results are obtained if both treatments (mechanical and electrochemical) are applied (Grimnes and Martinsen, 2008). Therefore, the use of mechanical and electrochemical treatments has been demonstrated to overcome part of the problem of the impedance polarization at low frequencies. It is worth mentioning, that the deposition of an interface layer on metal may have a deleterious effect and eventually the layer will wear off so periodic recoating may be required.

Even the use of methods or techniques to improve the impedance measurements, and reduce problems due to the electrode-tissue interface and impedance analyser system (systematic errors), errors persist. To overcome these, researchers (Dean et al., 2008; Laufer et al., 2010) have been used Gabriel's method presented in Section A.2.3 (Gabriel et al., 2009). This method consists of characterizing the cell constant 'K' in a saline (NaCl) solution with similar conductivity of the soft tissue to be measured. Data on saline solutions with different concentrations and conductivities is known (Peyman et al., 2007). Saline solution has no dielectric properties in the frequency range DC - 1 MHz, therefore, no imaginary part should appear in the measurements of impedance within this range.

These problems must be taken in consideration when selecting a good electrode for a given application since they can interfere in the impedance measurements. Sometimes the application will not require extra actions (techniques) to cope with these. For example, if the frequency of interest is at high frequency no further actions will be necessary. However, at low frequencies it has been shown how the impedance measurements can be affected. That is why, before measurement in living tissue occurs it is advisable to characterize the electrodes for two main reasons: to know the magnitude of the error and to compensate with appropriate techniques that overcome the problems.

A.3 Fibre optic sensing technology basics

A.3.1 Introduction

Optical fibre sensors (OFS) have been used, mainly, for exploration and mining, civil, transportation and aerospace industry for long time. Lately, thanks to the advances in the microfabrication technology, it has started being used in biomedical applications due to its inherent attractive properties such as: small size, biocompatibility, multipoint measurement, linear temperature effect and immunity to electromagnetic interferences (Baldini et al., 2008; Mishra et al., 2011; Poeggel et al., 2015). These advantages overcomes some of the problems of solid-state sensors such as the cross-talk between electronic devices, non-linear temperature effect and so on.

Different OFS can be classified according to the structure of the sensor and the modulation technique. The sensing element can be built in the fibre (intrinsic) or can be an extended part of the fibre (extrinsic). The detection of any change in the sensing element is detected by the intensity, frequency or phase. In this thesis, Fibre Bragg gating (FBG's) sensors and their interragoation and modulation techniques have been considered.

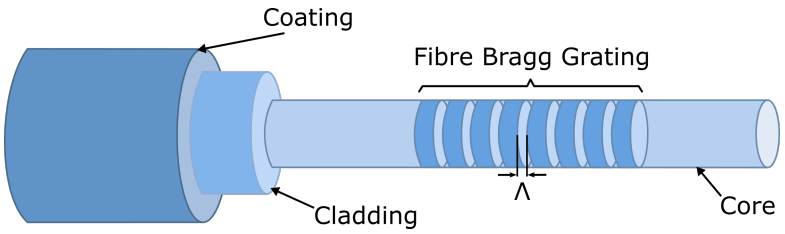

Figure A.5: Optical fibre with a fibre Bragg grating. The periodicity of the grating structure, Λ, is typically of the order of 500 nm.

The fibre is composed of a core surrounded by a cladding and a coating. The FBG is an intrinsic sensor and it is possible to contain one or multiple sensing elements in a single fibre, each with a different characteristic period. The FBGs used in this thesis are written by UV light during the fabrication process. These sensing elements consist of a pattern with a specific refractive index with a periodicity that reflects a specific wavelength know as Bragg wavelength (Equation A.15).

$$\lambda_B = 2n_{eff} \times \Lambda \tag{A.15}$$

Where Λ is the pitch of the grating, n_{eff} is the effective refractive index of the core and λ_B is the Bragg wavelength. When light is launched into the fibre core, these sensing

elements reflect the light back at specific wavelength (see Figure A.6).

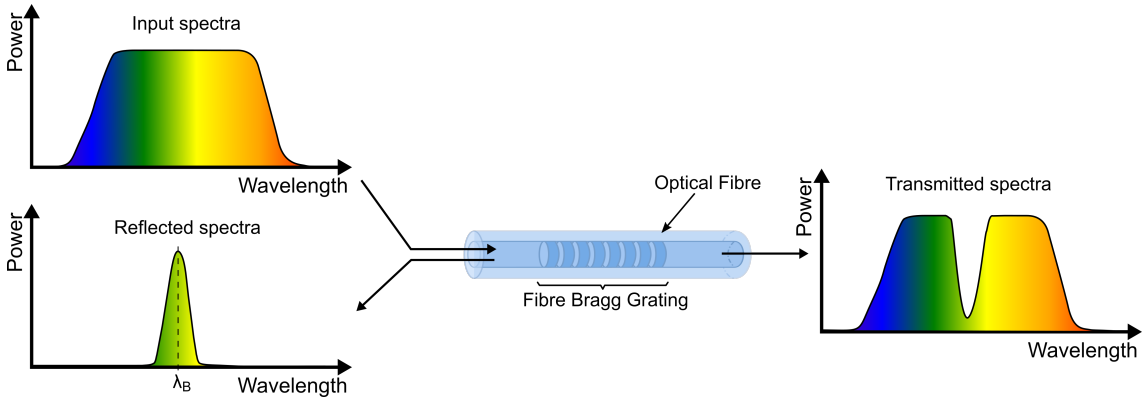

Figure A.6: Schematic representation of light interacting with a fibre Bragg grating. Broadband light is launched into the fibre, a narrow band of light is reflected and the remaining spectral components are transmitted.

The pitch of the grating and the refractive index are sensitive to strain and temperature; hence shifting the Bragg wavelength. The following equation (Equation A.16) represents the changes in wavelength by strain and temperature:

$$\frac{\Delta\lambda}{\lambda_0} = k \cdot \varepsilon + \alpha_\delta \cdot \Delta T \tag{A.16}$$

Where k is gauge factor, ε is the strain, α_δ is the change of the refraction index, and ΔT is the temperature change. The first term describes the wavelength shift induced to the fibre due to mechanical and thermal strain and the second one describes the change of refraction index caused by temperature. Equation A.17 is more detailed and takes into account the thermal expansion coefficient of an external package, α_{pk}, when the grating is fixed at both ends or thermal expansion coefficient of glass, α_{glass}, when the grating is only fixed at one end:

$$\frac{\Delta\lambda}{\lambda_0} = (1 - p_e) \cdot \varepsilon_m + \Big((1 - p_e) \cdot \alpha_{(pk,glass)} + \eta\Big) \cdot \Delta T \tag{A.17}$$

Where:

$\Delta\lambda$ Wavelength shift.

λ_0 Initial wavelength.

p_e Photo-elastic coefficient of silica, $p_e = 0.22$.

ε_m Mechanical strain.

α_{pk} Thermal expansion coefficient of package.

α_{glass} Thermal expansion coefficient of glass, $\alpha_{glass} = 0.55 \times 10^{-6}/℃$.

η Thermo-optic coefficient of the refractive index, $\eta = 8.6 \times 10^{-6}/℃$.

ΔT Temperature change in ℃.

Thus, a change in Bragg wavelength can be due to the strain applied or to the change in ambient temperature. Therefore, when measuring strain with FBGs, a compensation method is needed to avoid any change in Bragg wavelength due to variations in temperature. A few approaches have been described in the literature (Rao, 1998). In this thesis, only two methods have been used and these are explained.

Reference FBG method: As one single fibre is not able to separate both effects strain and temperature. A second strain-free fibre as close as possible to the first fibre is used. This second fibre only measures the Bragg wavelength shift due to the temperature, then, the temperature artefact can be removed by subtracting the Bragg wavelength shift due to temperature effect.

Dual-wavelength superimposed FBGs method: This method also uses a similar approach to the reference FBG method, with the difference that the second fibre is also sensitive to strain. The two FBGs need to be close and under different sort of force, if both fibres are under the same magnitude of force this method will not work as they will exhibit the same wavelength shift. Assuming that the fibres are under different force and the total wavelength shift for each fibre due to strain and temperature are linear, the Bragg wavelength is given by:

$$\begin{pmatrix} \Delta\lambda_{B_1} \\ \Delta\lambda_{B_2} \end{pmatrix} = \begin{pmatrix} K_{\varepsilon_1} & K_{T_1} \\ K_{\varepsilon_2} & K_{T_2} \end{pmatrix} \begin{pmatrix} \Delta\varepsilon \\ \Delta T \end{pmatrix} \tag{A.18}$$

Where K_ε and K_T are the strain and temperature sensitivity. These calibration constants must be determined against a known strain and temperature.

A.3.2 Interrogation techniques

To detect a change in strain or temperature, the FBG sensors needs to be interrogated by guiding the light through the fibre by means of light source, and simultaneously reading the intensity of the reflected light at specific wavelength with a photodetector. By

interrogating the FBG's continuously, any change in strain or temperature will shift the reflected wavelength. Two configurations can be used to interrogate the FBG's sensors (Figure A.7); with a **broadband light** source and a spectrometer; or with a **tunable laser** source and a photodetector (photodiode).

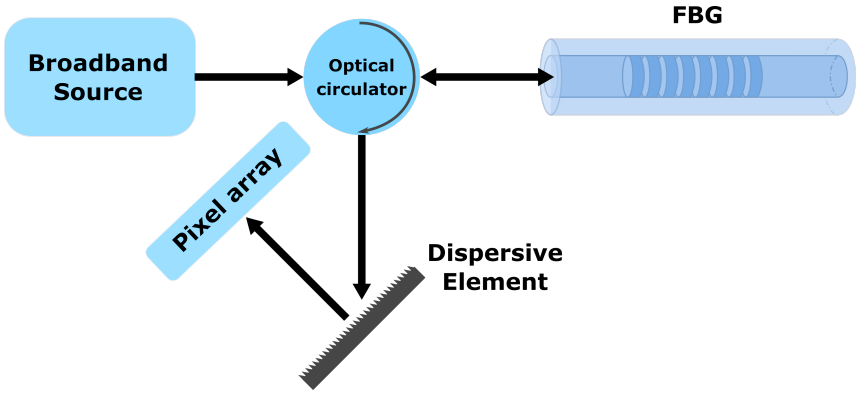

(a)

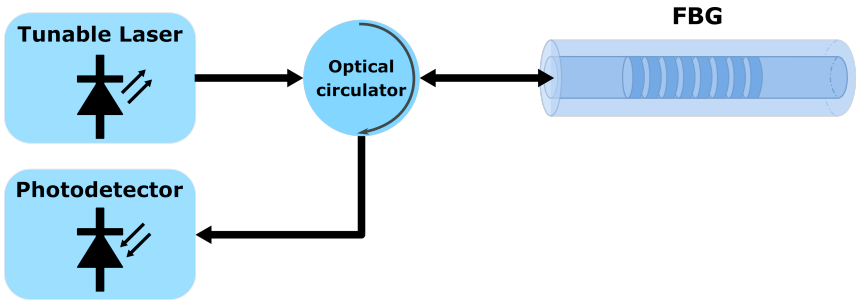

(b)

Figure A.7: Schematics of interrogation techniques: (a) broadband laser in conjunction with a CCD pixel array and (b) tunable laser in conjunction with a photodetector.

The broadband light source emits light over a wide spectral range along the fibre, whereas the tunable laser source has a high-powered narrow band light that sweeps along the full spectrum of the source. In the former case, FBG sensors reflect back the Bragg wavelength light to a dispersive element (diffraction grating), and the remaining components of the spectrum will not be reflected; ending up at the other end of the fibre. Then, the dispersive element separates the reflected wavelength into an array of sensors that converts the light intensity into voltage. While, in the second configuration there is only one sensor that converts the reflected light into a voltage and the spectra is defined by the wavelength of the laser as it tunes through its spectral range; hence there is no need for a dispersive element.

A.3.3 Multiplexing techniques

It would not be viable to use an interrogation system for each sensing element due to the high cost components of the interrogation system. To overcome this problem some multiplexing techniques have been used. There are available three multiplexing techniques; spatial division multiplexing (SDM), wavelength division multiplexing (WDM) and time division multiplexing (TDM). Only WDM is explained as it is the multiplexing technique used in this thesis, but more information about the others can be found in (López-Amo and López-Higuera, 2011).

The WDM technique consist of interrogating a single fibre with multiple sensing points along it. Sensing points can be separated at any given distance as long as the FBG sensor does not physically overlap with the next and as long as the attenuation in the intervening fibre is not too high for the dynamic range of the detector. However, the wavelength range of the interrogator unit and the wavelength range of sensor's operation limit the number of sensing elements that a fibre can usefully contain. For example, if two consecutive FBG sensors have a range of ± 2 nm and are separated by 4 nm or both sensors are apart by 2 nm but both work on the same direction, these FBG sensors' signal will not overlap. On the other hand, if both FBG sensors move towards each other, then sensors' wavelengths will overlap causing sensor-to-sensor crosstalk (see Figure A.8), or the loss of one or both sensors.

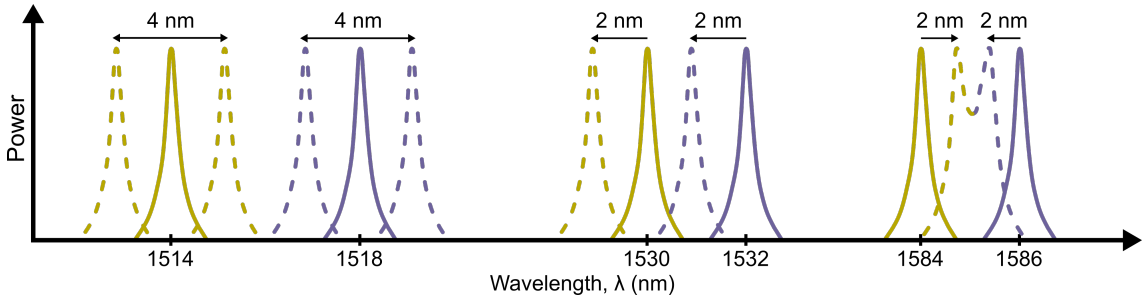

Figure A.8: Schematic representation of reflected wavelength peaks from two spectrally adjacent FBGs. The required separation between peaks depends on the bandwidth of each peak, and the mode of operation of both sensing elements. Cross talk will occur if the spectral peaks start to merge.

Appendix B

Design and development of a custom bioimpedance measurement system

The work presented in this appendix is the subject of the following refereed conference paper:

Ruiz-Vargas, A, Arkwright, JW, Ivorra, A. A portable bioimpedance measurement system based on Red Pitaya for monitoring and detecting abnormalities in the gastrointestinal tract. In: *2016 IEEE EMBS Conference on Biomedical Engineering and Sciences (IECBES)*. IEEE; 2016:150-154. doi:10.1109/IECBES.2016.7843433.

B.1 Introduction

Commercial impedance analyser systems are available with high performance over a wide-range of frequencies and impedance ranges. However, these systems have some disadvantages: 1) Most commercial measurement systems exhibit low sampling rates because they are not intended to monitor impedance evolution but to perform accurate static measurements. 2) Most systems are 2-terminal systems not suitable for bioimpedance because of the contact impedances that appear at the interface between the electrode and the sample. It should also be noted that even 4-terminal systems do not have ideal features to take impedance measurements due to their low input impedance. 3) A majority of these systems do not comply with electrical safety standards for *in-vivo* human measurement.

As part of my PhD, I have developed a bioimpedance measurement system (BMS) to perform bioimpedance measurements with the developed devices under this thesis. In this appendix, I present the design, construction and validation of a portable, low-cost 4-terminal bioimpedance measurement system with its interface software that have been used during the experiments performed during this thesis. The BMS can be powered by either a normal charger or a power bank, which makes it inherently safe, and suitable for real-time ambulatory measurement.

B.2 System description

The system consists of a Red Pitaya board (www.redpitaya.com) and custom designed front-end circuitry, see Figure B.1, with a software interface developed in NI LabView (National Instruments Corporation, Austin, USA) and Matlab R2015 (Mathworks, Massachusetts, U.S.A) allowing dynamic reconfiguration of current and voltage, and real-time data acquisition. Data acquisition is based on an auto-balancing bridge method in which a sinusoidal current is injected through the sample, waits for 5 cycles to reach steady state and then simultaneously acquires 2 cycles of the current flowing through and the voltage across the sample. The impedance calculations are then executed in the Red Pitaya processor. The data is sent in real-time to the PC, via an Ethernet cable and/or to an iPad by via a wireless USB dongle.

The software application allows the user to take and record either single frequency measurements or multi-frequency measurements in real time. In single-frequency measurement mode, acquisition and calculations take about 72 ms at an excitation frequency of 1 kHz, and for multi-frequency measurement mode, the acquisition of 5 different frequencies from

1 kHz to 1 MHz, takes about 200 ms. The data is streamed to disk and stored dynamically in a text file. The user can make comments during acquisition in order to synchronize the measurements with other devices. It also allows the user to fit and plot the multi-frequency data in a Cole-Cole plot and display its four parameters: alpha (α), characteristic frequency (fc), R_∞ and R_0 (Cole and Cole, 1941).

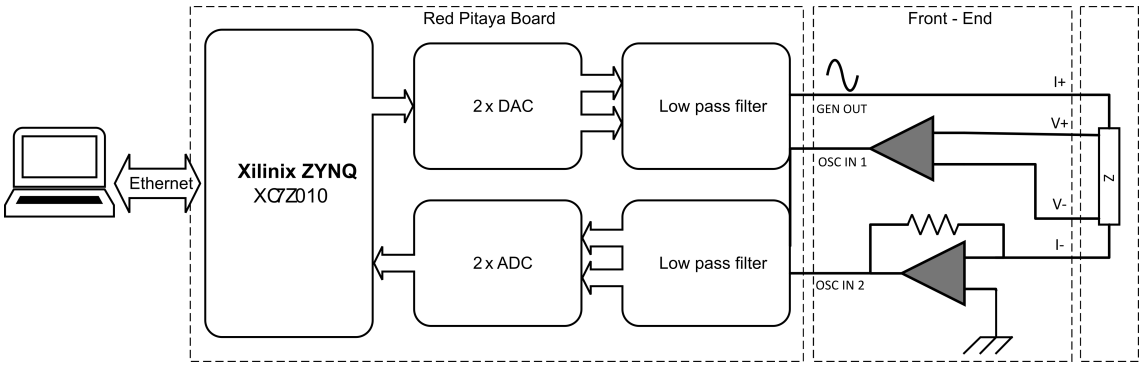

(a)

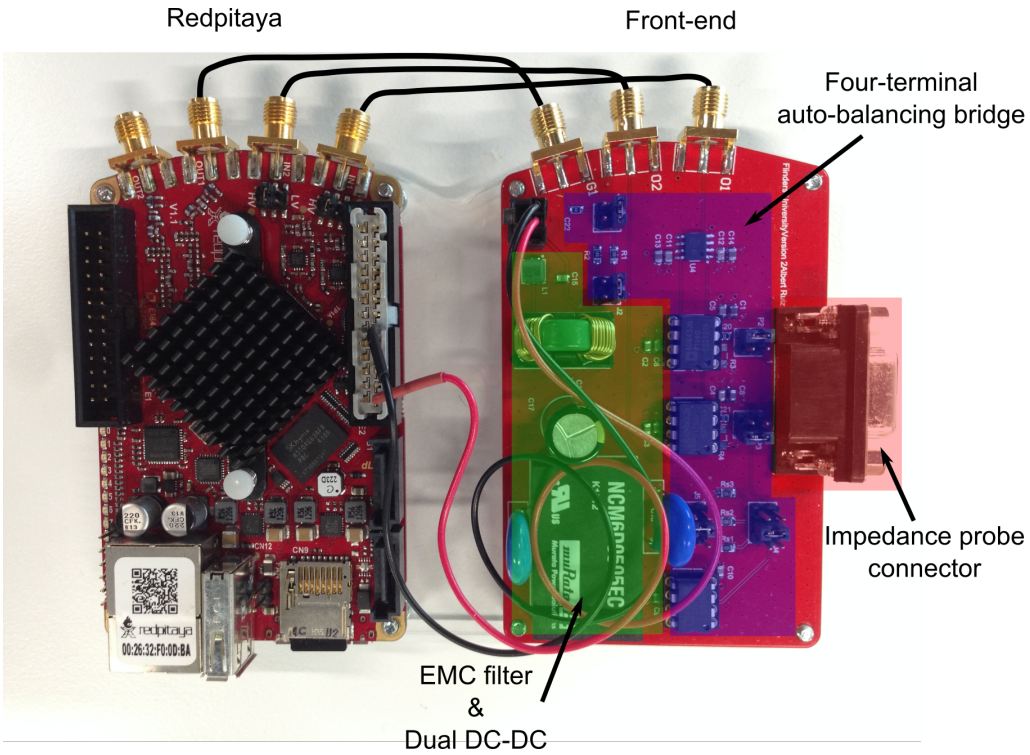

(b)

Figure B.1: (a) Representation of the general hardware architecture of the bioimpedance measurement system. (b) Picture of bioimpedance system with front-end. The green shaded area shows the electromagnetic filter and dual power supply, the blue shaded area shows the signal conditioning circuit (auto-balancing bridge), and the red shaded area shows the connector where the impedance probe is connected.

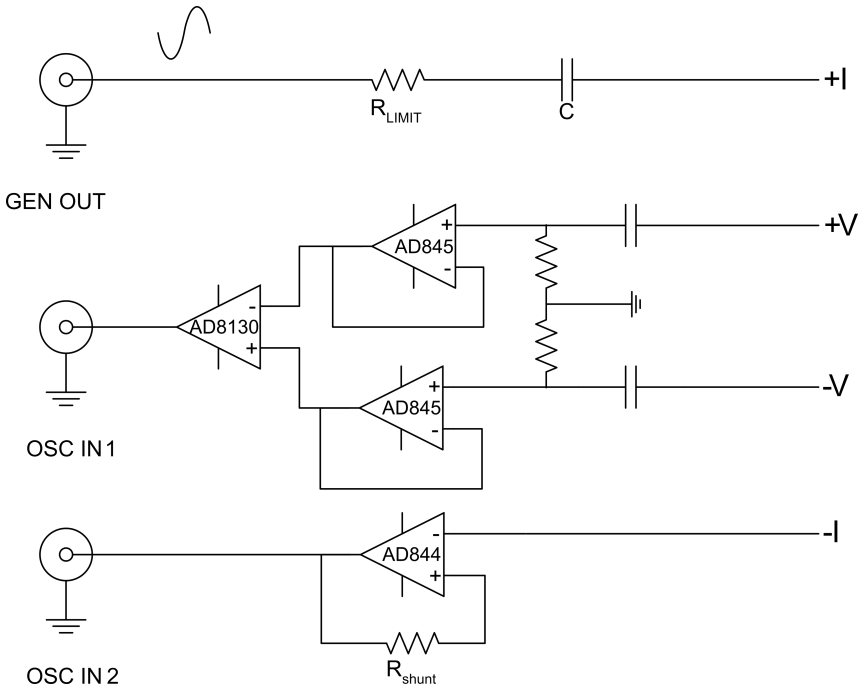

Figure B.2: Four-terminal auto-balancing bridge schematic used on the front-end.

B.3 General hardware design

Figure B.1 and B.2 show the hardware architecture of the BMS and the 4-terminal auto-balancing bridge schematic. To minimize the development time, it was decided to employ a Red Pitaya board to generate the signal and acquire both the current and voltage across the sample under test. Red Pitaya boards have powerful digital signal generation and processing capabilities (Dual Core ARM Cortex A9+FPGA) and FPGA (Xilinx Zynq 7010 SoC) able to generate sinusoidal signals and to process signals in real time. Output analogue signals are generated by a high speed (125 MSamples/s) 14-bit Digital to Analogue Converter (DAC) and afterwards passed through a low pass filter with 50 MHz cut off frequency. The voltage and current are acquired through a low pass filter (50 MHz cut off frequency) which is then digitized by the dual high speed (125 MSamples/s) 14-bits Analogue to Digital Converter (ADC) which passes the data to the FPGA.

The Redpitaya board provides half of the system. The Redpitaya board output and inputs are connected to the front-end input and outputs by means of coaxial cables (see Figure B.1). Figure B.1(b) shows the different parts in the front-end. The green shaded area corresponds to an electromagnetic filter and dual power supply to provide $\pm$ 5 V to the electronic components in the blue shaded area. The red shaded area is a D-9 connector where the impedance probe is connected. The blue shaded area corresponds to the 4-terminal auto-balancing bridge circuit.

The auto-balancing bridge circuit applies the current to the sample and conditions the voltage across and current through the sample. A resistor and capacitor are used in series to limit the maximum applied current for patient's safety. A 10 kΩ resistor was chosen to limit the maximum current flowing through the living tissue. The Red Pitaya delivers ± 1 V therefore the maximum current flowing through the system is limited to 100 µA.

The trans-impedance amplifier (AD844) is used as a current to voltage converter to read the current flowing through the sample. The positive input is connected to ground which takes the negative input to zero, channeling the current through the shunt resistance. The voltage across this resistance will be $Vout = -R_{shunt} \cdot I$. The shunt resistance provides gain, so once the signal is digitized it needs to be divided by the same value in order to output the correct current value.

In order to measure the voltage across the sample the AD8130 differential amplifier was used which provides a good common mode rejection ratio (CMRR) across the spectrum. However, its input impedance is not as high as the instrumentation amplifiers. Thus, the two operational amplifiers (AD845) prior to the differential amplifier inputs assures a high input impedance in the system. The function of the capacitance and the resistance prior to the input buffer is to avoid any DC current passing through the sample.

B.3.1 Signal processing

A digital coherent demodulation technique is applied to the digitized signal from the ADC buffers taking advantage of the Red Pitaya on-board processor. Figure B.3 shows the block diagram of this process. The digital coherent demodulation process extracts real and imaginary part of a signal, by multiplying the signal, Equation B.1, by two reference signals, one in phase and one in quadrature with same frequency as the injected signal, obtaining then (Equation B.2 and B.3):

$$v(t) = A\cos(2\pi f_0) \tag{B.1}$$

$$v_r(t) = v(t)\cos(2\pi f_0) \tag{B.2}$$

$$v_x(t) = v(t)\sin(2\pi f_0) \tag{B.3}$$

Afterwards, a non-linear digital filter (mean filter) is applied to $v_r(t)$ and $v_x(t)$, to get the values of the real and imaginary parts, as the important information is in the DC component of $v_r(t)$ and $v_x(t)$. This process is applied to both signals to obtain the complex numbers of voltage and current. Finally, Equation B.4 is applied to get the complex value

of the impedance.

$$Z = \frac{\Re(v) + \Im(v)}{\Re(i) + \Im(i)} \tag{B.4}$$

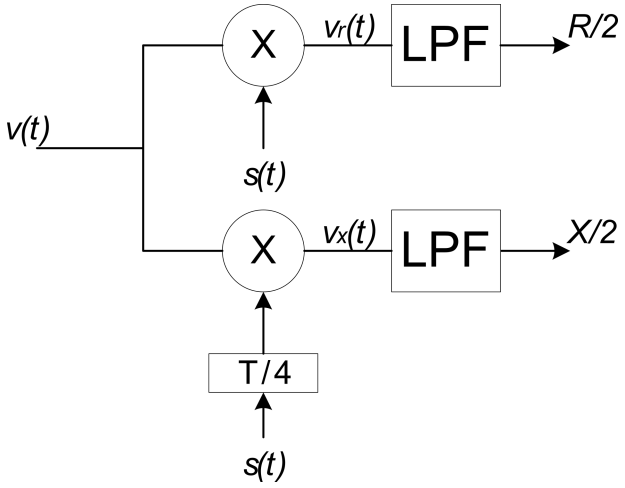

Figure B.3: Block schematic of digital coherent demodulation signal.

B.3.2 Software

Data was acquired using a custom written LabVIEW program and additional graphical user interface was developed in Matlab for post-processing. The user can visualize the data on a table, and select sets of data to fit it in a Cole-Cole model (Cole and Cole, 1941) and plot in four different graphs: 1) Cole-Cole plot, 2) Bode diagram, 3) Real and Imaginary vs frequency, and 4) electrical properties (conductivity σ and relative permittivity ε_r). The four known Cole-Cole parameters (α,fc , R_∞ and R_0) are also shown on the user interface.

B.4 System evaluation

In order to validate the performance of the system, we employed an equivalent circuit model of a cell suspension (0.9997 kΩ resistor in series with a 97.26 nF in parallel with 1.0007 kΩ resistor measured with an Agilent U1253B Multimeter with an accuracy of 0.05% ± 5 LSD (least significance digit) for resistors and 1% ± 5 LSD for capacitors).

Table B.1: Impedance measurement system´s accuracy of an equivalent circuit model of a cell suspension from 10 Hz to 1 MHz.

Frequency	**True value**		**Measured value**		**Relative error (%)**	
	|Z|(Ω)	Phase(°)	|Z|(Ω)	Phase(°)	Mag	Phase
10 Hz	999.64	-0.350	999.23	-0.35	< 0.1	0.0050
100 Hz	994.16	-3.470	993.69	-3.46	< 0.1	0.0009
1 kHz	741.94	-19.260	743.13	-19.15	< 0.1	0.0001
10 kHz	505.10	-4.610	505.51	-4.69	< 0.1	0.0009
100 kHz	500.19	-0.470	500.12	-0.58	< 0.1	0.0417
1 MHz	500.15	-0.047	499.66	-1.05	< 0.1	0.4704

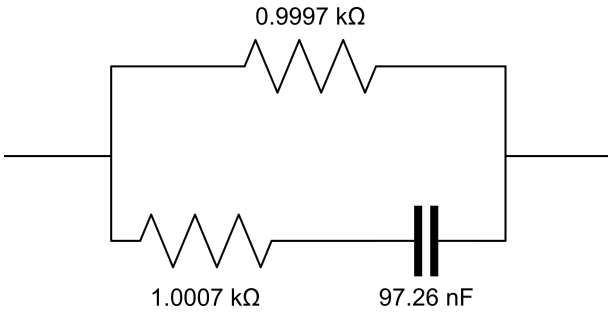

Figure B.4: Equivalent circuit model of a cell suspension.

Eleven measurements were performed in the frequency range from 10 Hz to 1 MHz. Table B.1 shows the range of true values measured with a PM6304LCR meter from Fluke (Fluke, Washington, USA) with an accuracy of 0.1%, the mean value of results obtained with our impedance measurement system and percentage deviation for magnitude and phase within range frequency of 10 Hz – 1 MHz. The impedance measurement system has low standard deviation in magnitude and phase ($< 0.02\%$ and $< 0.47\%$ respectively) from 10 Hz to 1 MHz.

A range of pure resistors from 1 Ω to 1 MΩ (1% tolerance) were employed to measure the accuracy. These resistors were measured with the PM6304LCR meter. Table B.2 shows the values obtained with the LCR meter and the percent error obtained with our system from 10 Hz to 1 MHz for the impedance range 1 Ω to 1 MΩ. The system is capable of measuring low impedances (< 10 Ω) with accuracies of better than 0.55% up to 100 kHz, however at higher frequencies the accuracy degrades to 34% at 1 MHz. The accuracy of the system for impedances up to 10 kΩ is $< 2.02\%$ up to 1MHz. The accuracy for impedances larger than 100 kΩ increases to 2.43% at 100 kHz. The system's accuracy at lower (< 10 Ω) and larger (> 100 kΩ) impedances at high frequencies (> 100 kHz) decreases noticeably.

Table B.2: Impedance measurement system's accuracy for an impedance range of 1 Ω to 1 MΩ from 10 Hz to 1 MHz. Significant error values are shaded.

	Percent error (%)					
	10Hz	**100 Hz**	**1 kHz**	**10 kHz**	**100 kHz**	**1 MHz**
1.05 Ω	0.86	1.25	1.05	1.04	2.04	3.004
10.07 Ω	0.51	0.45	0.55	0.22	0.03	0.90
100.3 Ω	0.07	0.07	0.07	0.06	0.05	0.04
0.9997 kΩ	0.69	0.69	0.69	0.70	0.70	0.81
9.963 kΩ	0.08	0.08	0.07	0.10	0.18	2.02
100 kΩ	0.21	0.21	0.20	0.09	2.43	46.68
1 MΩ	0.08	0.13	0.11	2.94	53.48	93.71

This could be explained by the parasitic capacitances and inductances in the system that cause signal distortion and limit the bandwidth of the analogue path.

Finally, the effective CMRR (common mode rejection ratio) of the system was simulated for the frequency range 1 Hz to 10 MHz with LTspice IV (Linear Technology, Milpitas, CA, USA). Figure B.5 shows the results of the simulated CMRR of the front end depicted in Figure B.1. The CMRR of a differential amplifier should be infinite; however, due to the imperfections of the operational amplifiers, this is not achievable. A -60 dB CMRR value is considered average, and -100 dB is considered high CMRR while below -60 dB is considered quite poor CMMR value. The system presents a high CMRR of -100 dB at low frequencies up to 10 kHz. From 10 kHz, there is a drop in the CMRR reaching -74 dB at 1 MHz.

B.5 Conclusions

Overall, the size and the power requirement makes our system portable and viable for measuring bioimpedance in any environment. In addition, the bioimpedance spectroscopy measurement system exhibits good accuracy in the impedance range of 10 Ω to 10 kΩ between the range frequency 10 Hz to 1 MHz (10 Hz to 100 kHz for impedance values of 1 Ω).

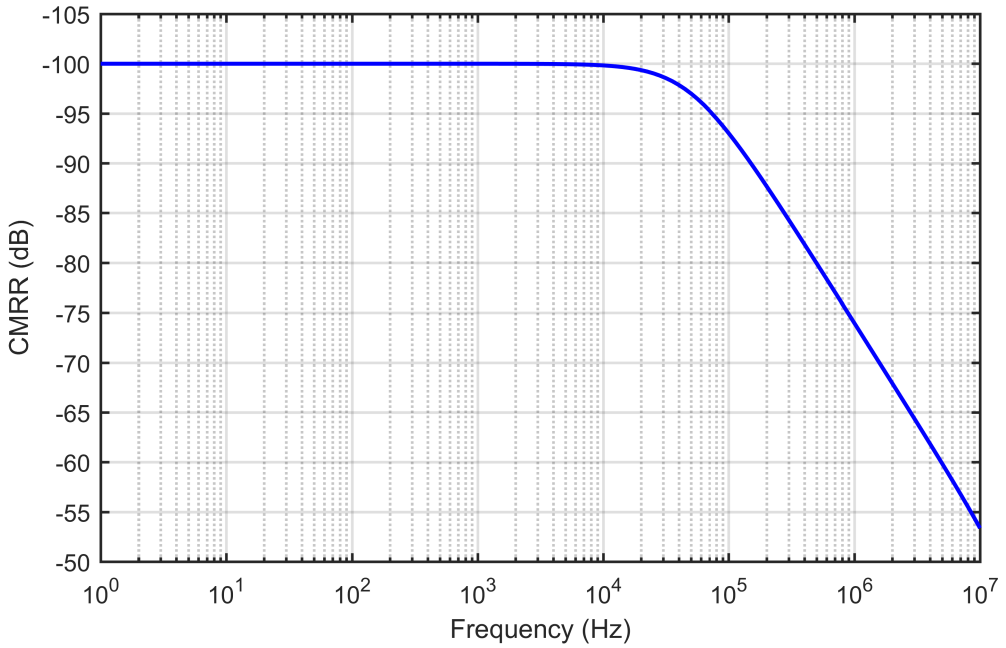

Figure B.5: Effective common mode rejection ratio vs frequency of the impedance signal conditioning circuit.

Appendix C

Additional material to chapter 3

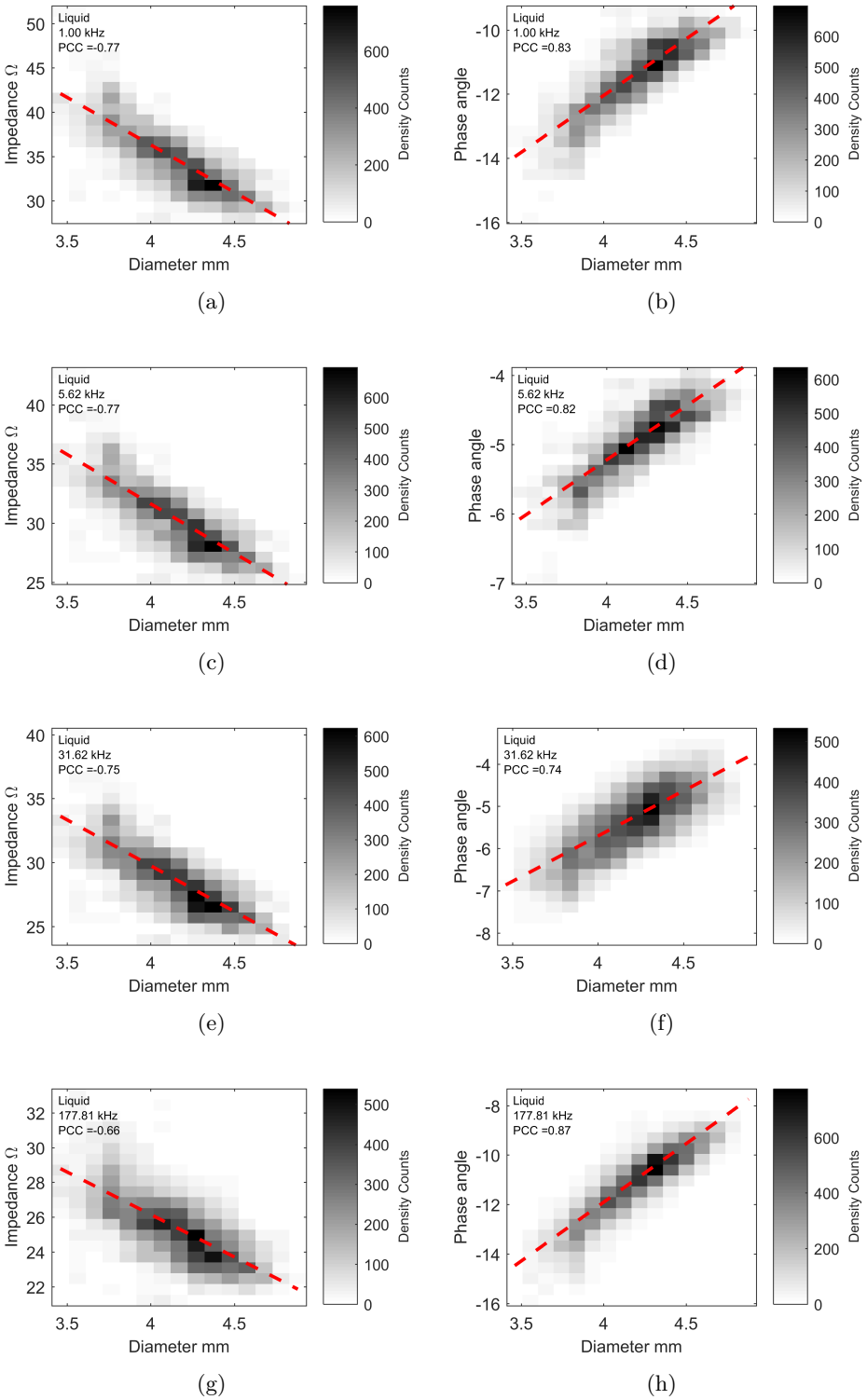

Figure C.1: Correlation graphs of impedance magnitude and phase angle against diameter at frequency range 1 – 177.81 kHz for liquid content.

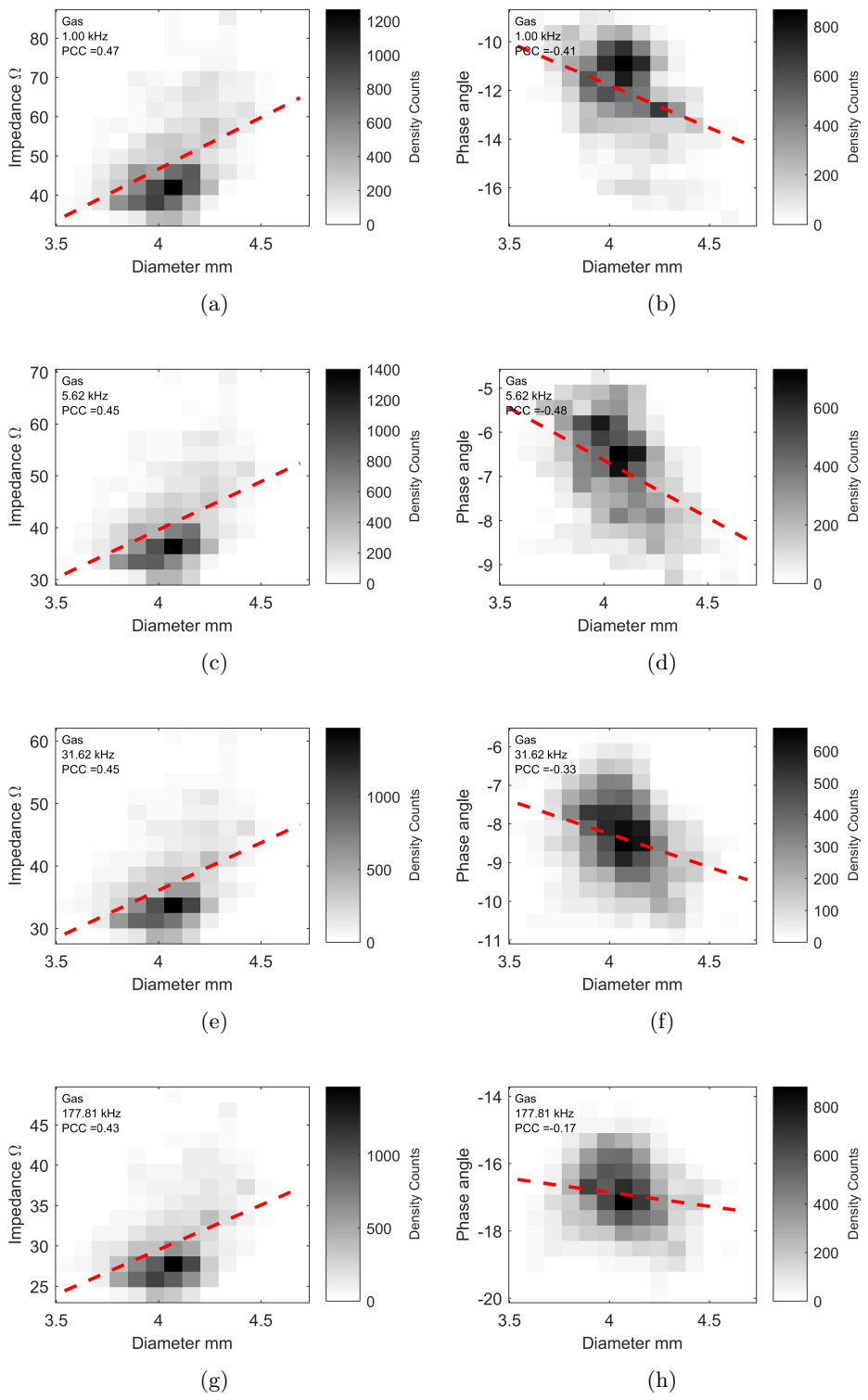

Figure C.2: Correlation graphs of impedance magnitude and phase angle against diameter at frequency range 1 – 177.81 kHz for gas content.

Table C.1: Nornality test results for impedance magnitude data.

Tests of Normality

	Shapiro-Wilk		
	Statistic	df	Sig.
F1_Liquid	0.963	1501	0
F1_Gas	0.882	1501	0
F2_Liquid	0.966	1501	0
F2_Gas	0.88	1501	0
F3_Liquid	0.971	1501	0
F3_Gas	0.876	1501	0
F4_Liquid	0.971	1501	0
F4_Gas	0.868	1501	0
F5_Liquid	0.724	1501	0
F5_Gas	0.802	1501	0

Table C.2: Wilcoxon Signed Ranks Test for impedance magnitude.

Ranks

		N	Mean Rank	Sum of Ranks
F1_Gas - F1_Liquid	Negative Ranks	79[a]	161.59	12766
	Positive Ranks	1422[b]	783.74	1114485
	Ties	0[c]		
	Total	1501		
F2_Gas - F2_Liquid	Negative Ranks	65[d]	158	10270
	Positive Ranks	1436[e]	777.84	1116981
	Ties	0[f]		
	Total	1501		
F3_Gas - F3_Liquid	Negative Ranks	78[g]	177.42	13839
	Positive Ranks	1423[h]	782.44	1113412
	Ties	0[i]		
	Total	1501		
F4_Gas - F4_Liquid	Negative Ranks	166[j]	344.61	57205
	Positive Ranks	1335[k]	801.53	1070046
	Ties	0[l]		
	Total	1501		
F5_Gas - F5_Liquid	Negative Ranks	859[m]	669.81	575367
	Positive Ranks	642[n]	859.63	551884
	Ties	0[o]		
	Total	1501		

a. F1_Gas < F1_Liquid; b. F1_Gas > F1_Liquid; c. F1_Gas = F1_Liquid; d. F2_Gas < F2_Liquid; e. F2_Gas > F2_Liquid; f. F2_Gas = F2_Liquid; g. F3_Gas < F3_Liquid; h. F3_Gas > F3_Liquid; i. F3_Gas = F3_Liquid; j. F4_Gas < F4_Liquid; k. F4_Gas > F4_Liquid; l. F4_Gas = F4_Liquid; m. F5_Gas < F5_Liquid; n. F5_Gas > F5_Liquid; o. F5_Gas = F5_Liquid

Table C.3: Wilcoxon test statistics for impedance magnitude.

Test Statistics[a]

	F1_Gas - F1_Liquid	F2_Gas - F2_Liquid	F3_Gas - F3_Liquid	F4_Gas - F4_Liquid	F5_Gas - F5_Liquid
Z	-32.798[b]	-32.946[b]	-32.734[b]	-30.152[b]	-.699[c]
Asymp. Sig. (2-tailed)	0	0	0	0	0.485

a. Wilcoxon Signed Ranks Test

b. Based on negative ranks.

c. Based on positive ranks.

Table C.4: Nornality test results for phase angle data.

Tests of Normality

	Shapiro-Wilk		
	Statistic	df	Sig.
F1_PA_Liquid	0.964	1501	0
F1_PA_Gas	0.958	1501	0
F2_PA_Liquid	0.978	1501	0
F2_PA_Gas	0.973	1501	0
F3_PA_Liquid	0.994	1501	0
F3_PA_Gas	0.997	1501	0.004
F4_PA_Liquid	0.979	1501	0
F4_PA_Gas	0.998	1501	0.086
F5_PA_Liquid	0.887	1501	0
F5_PA_Gas	0.879	1501	0

Table C.5: Wilcoxon Signed Ranks Test for phase angle.

Ranks

		N	Mean Rank	Sum of Ranks
F1_PA_Gas - F1_PA_Liquid	Negative Ranks	872[a]	818.56	713781
	Positive Ranks	629[b]	657.34	413470
	Ties	0[c]		
	Total	1501		
F2_PA_Gas - F2_PA_Liquid	Negative Ranks	1436[d]	779.67	1119603
	Positive Ranks	65[e]	117.66	7648
	Ties	0[f]		
	Total	1501		
F3_PA_Gas - F3_PA_Liquid	Negative Ranks	1487[g]	757.84	1126914
	Positive Ranks	14[h]	24.07	337
	Ties	0[i]		
	Total	1501		
F4_PA_Gas - F4_PA_Liquid	Negative Ranks	1500[j]	751.5	1127250
	Positive Ranks	1[k]	1	1
	Ties	0[l]		
	Total	1501		
F5_PA_Gas - F5_PA_Liquid	Negative Ranks	1366[m]	781.28	1067234
	Positive Ranks	135[n]	444.57	60017
	Ties	0[o]		
	Total	1501		

a. F1_PA_Gas < F1_PA_Liquid; b. F1_PA_Gas > F1_PA_Liquid; c. F1_PA_Gas = F1_PA_Liquid; d. F2_PA_Gas < F2_PA_Liquid; e. F2_PA_Gas > F2_PA_Liquid; f. F2_PA_Gas = F2_PA_Liquid; g. F3_PA_Gas < F3_PA_Liquid; h. F3_PA_Gas > F3_PA_Liquid; i. F3_PA_Gas = F3_PA_Liquid; j. F4_PA_Gas < F4_PA_Liquid; k. F4_PA_Gas > F4_PA_Liquid; l. F4_PA_Gas = F4_PA_Liquid; m. F5_PA_Gas < F5_PA_Liquid; n. F5_PA_Gas > F5_PA_Liquid; o. F5_PA_Gas = F5_PA_Liquid

Table C.6: Wilcoxon test statistics for phase angle.

Test Statistics[a]

	F1_PA_Gas - F1_PA_Liquid	F2_PA_Gas - F2_PA_Liquid	F3_PA_Gas - F3_PA_Liquid	F4_PA_Gas - F4_PA_Liquid	F5_PA_Gas - F5_PA_Liquid
Z	-8.940[b]	-33.102[b]	-33.538[b]	-33.558[b]	-29.984[b]
Asymp. Sig. (2-tailed)	0	0	0	0	0

a. Wilcoxon Signed Ranks Test

b. Based on positive ranks.